Figure 1.1 The Trans-Alaska Pipeline starts at Pump Station 1 in Prudhoe Bay. [Figure from www.clui.org/ludb/site/alaska-pipeline-origin.]

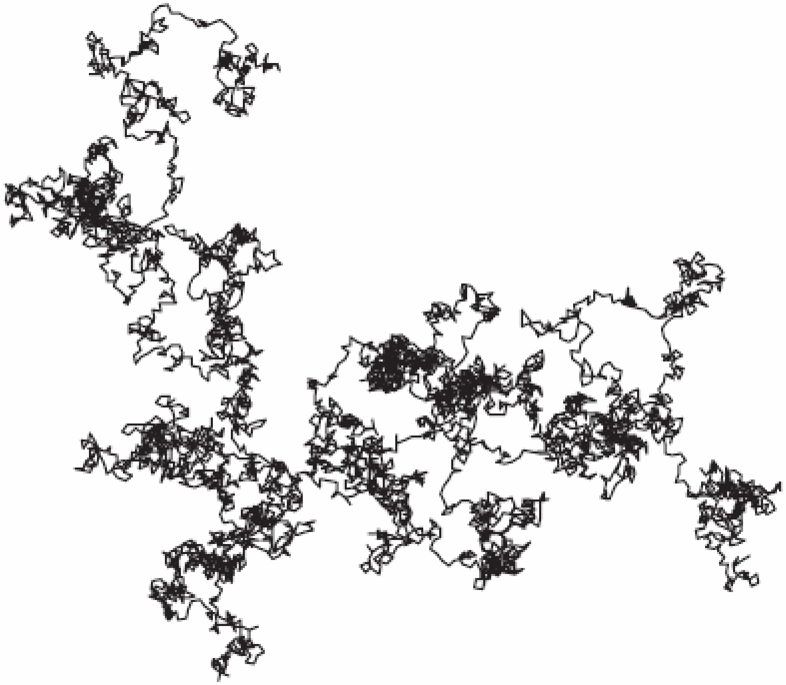

Figure 2.1 Trajectory of a Brownian Particle.

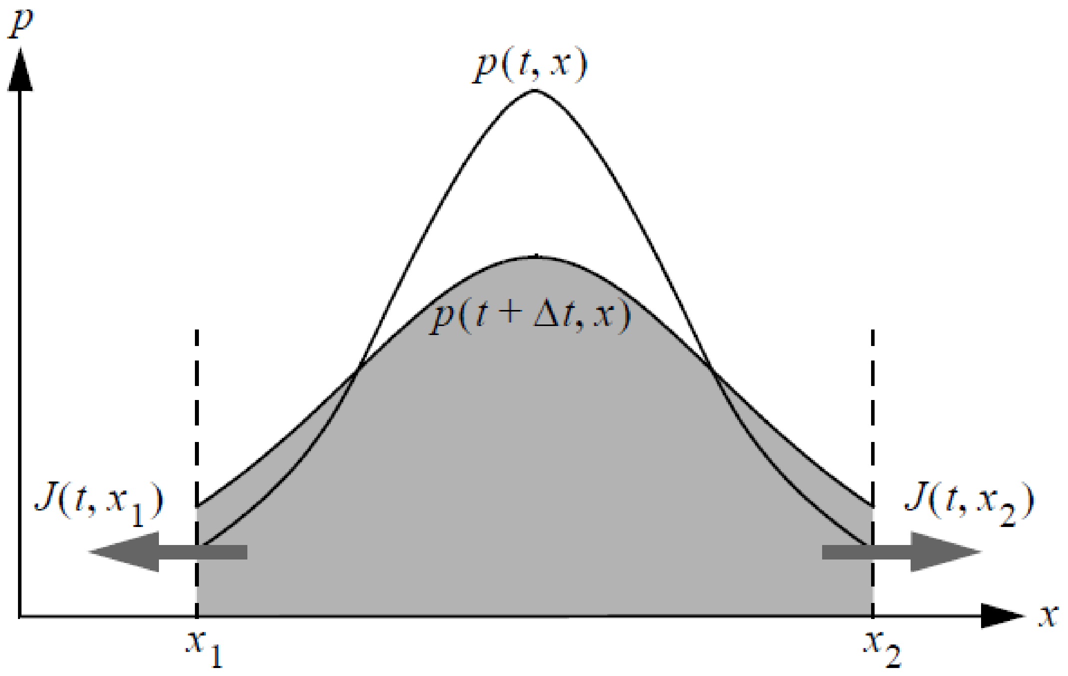

Figure 2.2 In the time interval from t to $t + \Delta t$, probability flows out of the interval [x1, x2] (note that the flux J(t, x1) is negative).

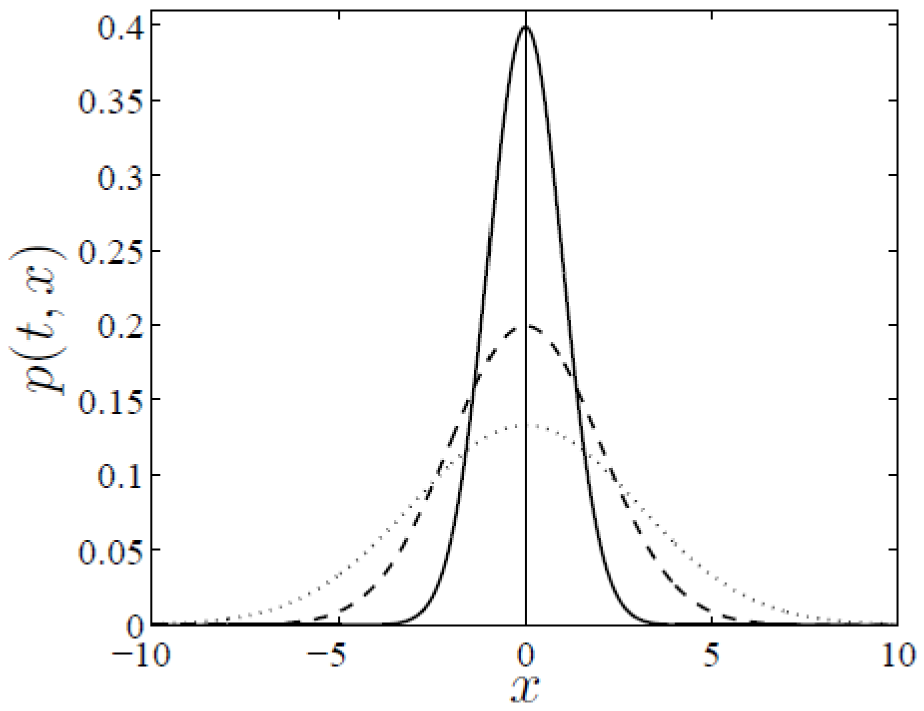

Figure 2.3 Gaussian solution of the diffusion equation (2.1) with drift A = 0 and diffusion coefficient D = 1 for t = 1 (continuous line), t = 4 (dashed line), and t = 9 (dotted line); the initial condition at t = 0 is assumed to be a ∂ function or a Gaussian of zero width located at the origin.

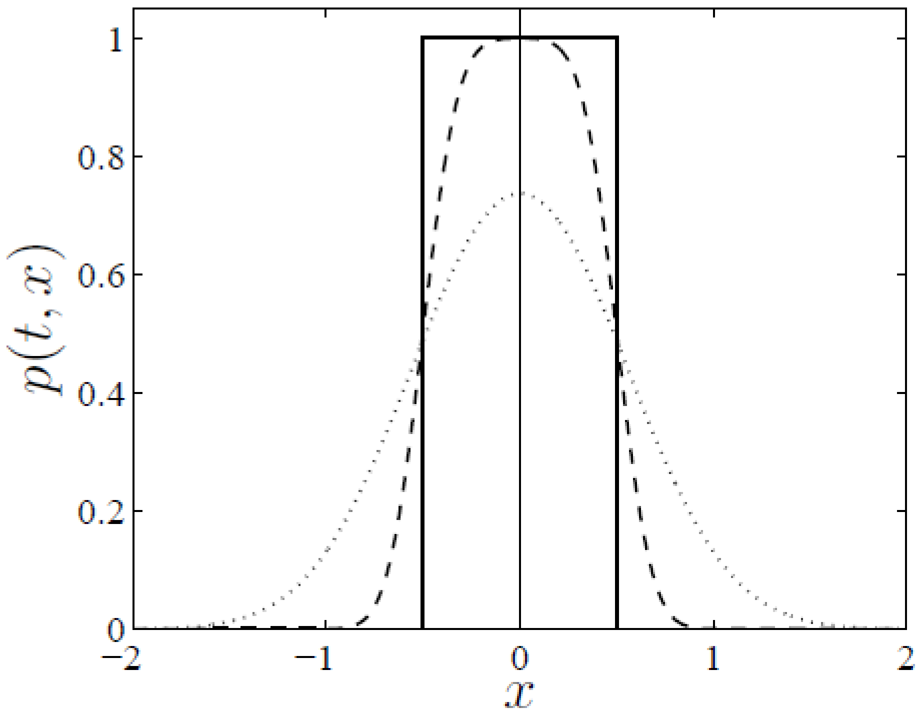

Figure 2.4 Solution of the diffusion equation (2.1) with drift A = 0 and diffusion coefficient D = 1 for t = 0 (continuous line), t = 0:02 (dashed line), and t = 0:2 (dotted line); the initial condition at t = 0 is chosen as a rectangular probability density.

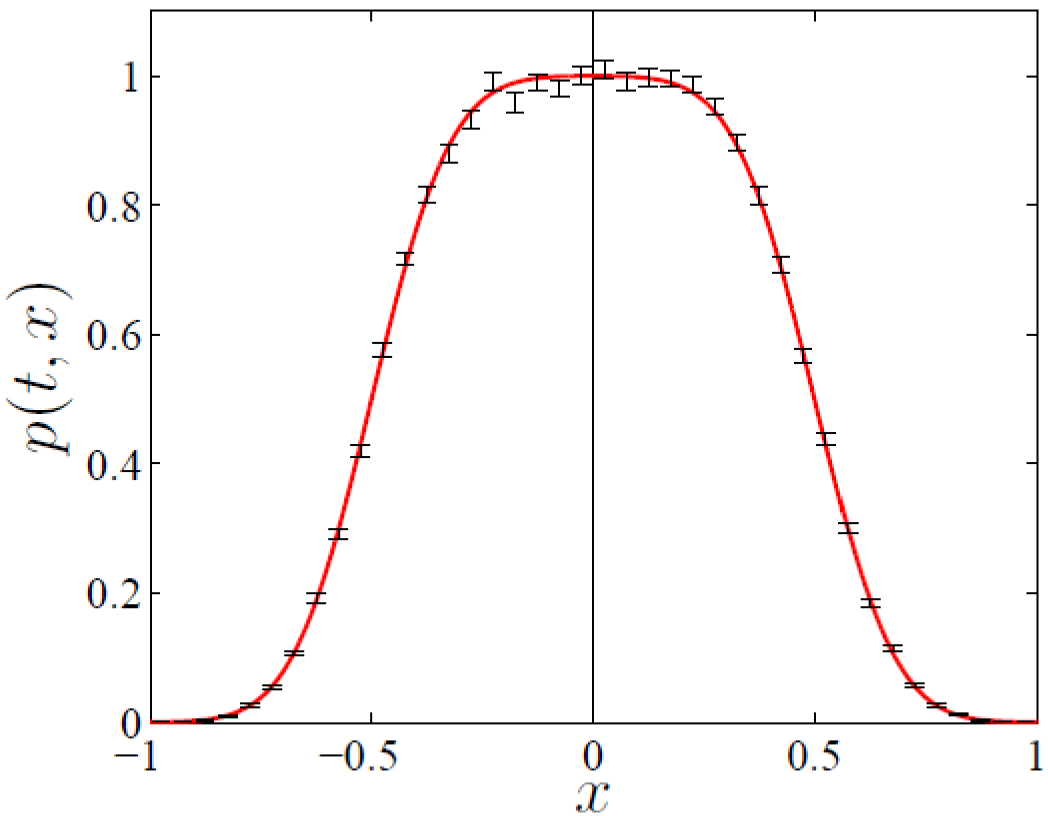

Figure 3.1 Solution of the diffusion equation (2.1) with drift A = 0 and diffusion coefficient D = 1 for t = 0:02 obtained from Brownian dynamics simulations (error bar symbols). For comparison, the exact solution is included (continuous line), and the result is a smeared version of the rectangular initial probability density.

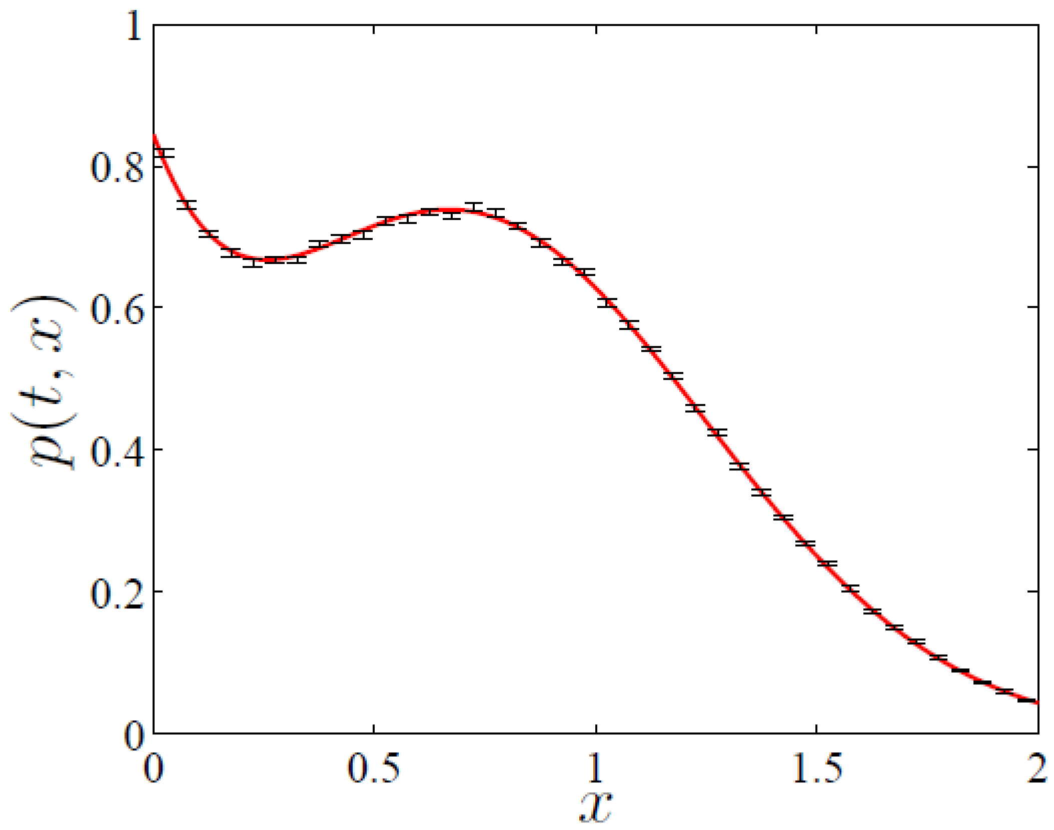

Figure 3.2 Solution of the diffusion equation (2.1) with drift *A* = -1 nd diffusion coefficient *D* = 1 for *t* = 0:3 obtained from Brownian dynamics simulations (error bar symbols). For comparison, the solution (3.19) is included (continuous line) where the particles start at *x* = 1 for *t* = 0.

Figure 4.1 Emmy Noether, 1882-1935.

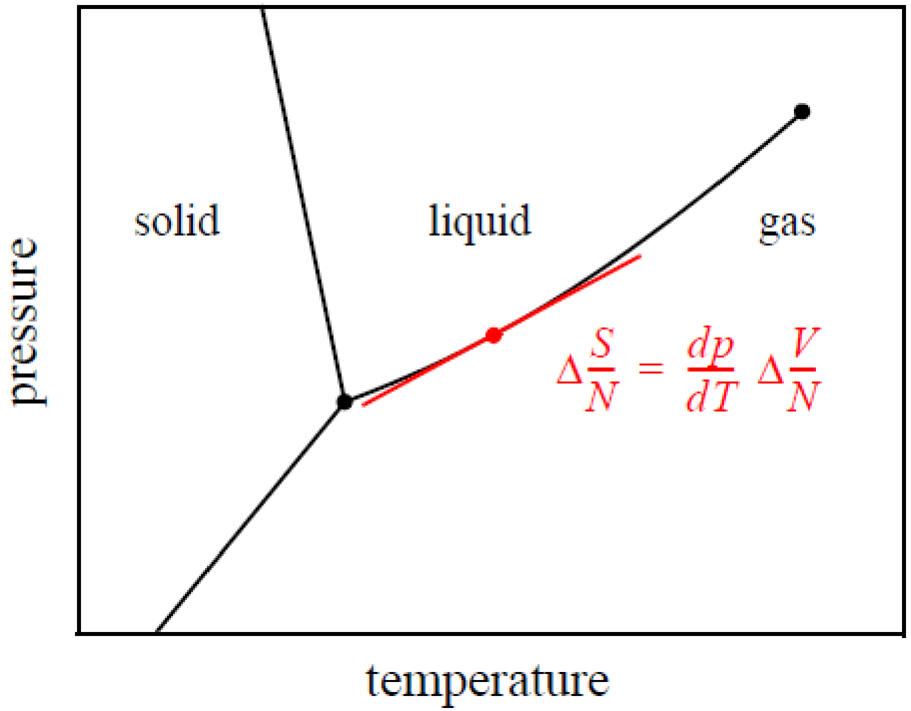

Figure 4.2 Illustration of the relevance of the Clapeyron equation.

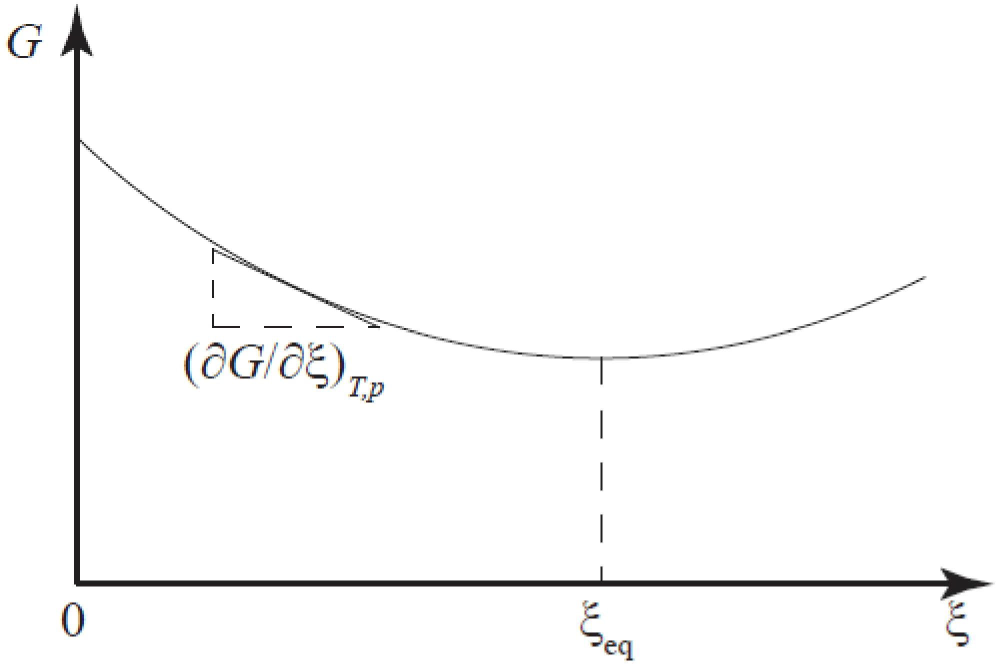

Figure 4.3 Gibbs free energy *G* for a system with chemical reaction as a function of extent of reaction ξ. At equilibrium, *G* is minimized at ξ eq.

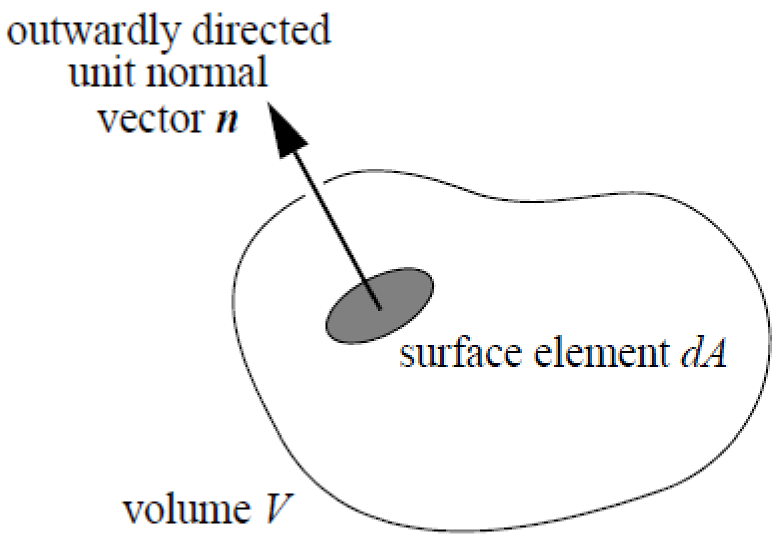

Figure 5.1 Arbitrary volume, fixed in space, over which mass, momentum, and energy balances are made.

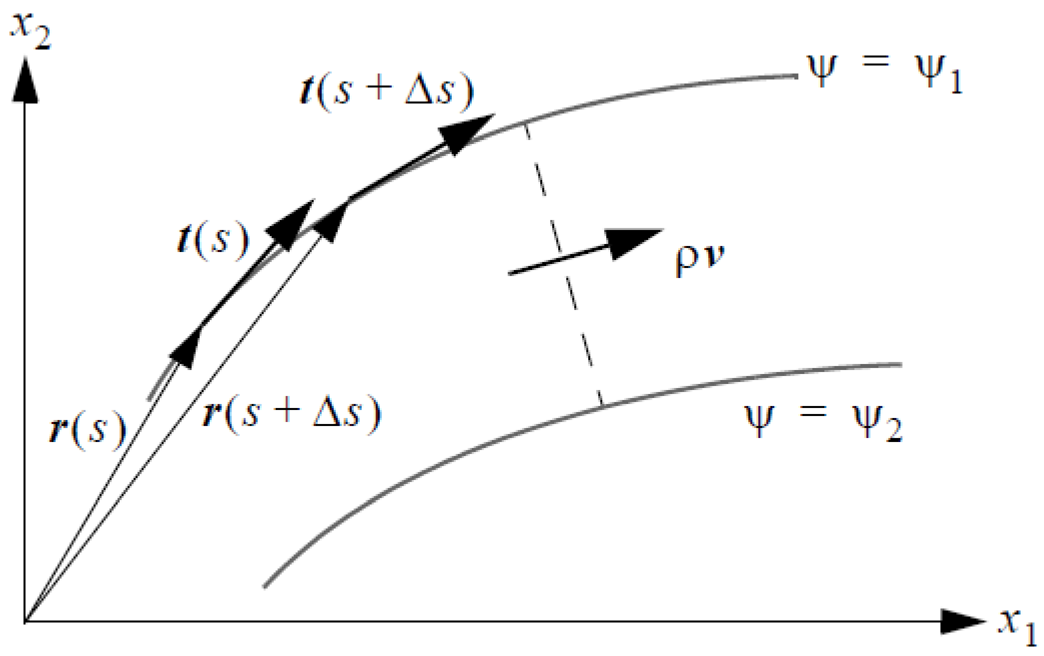

Figure 5.2 Streamline for a two-dimensional flow in the 1-2 plane showing unit tangent vector *t* at position *r.* Also shown is a second streamline connected to the first one by a dashed line at arbitrary positions.

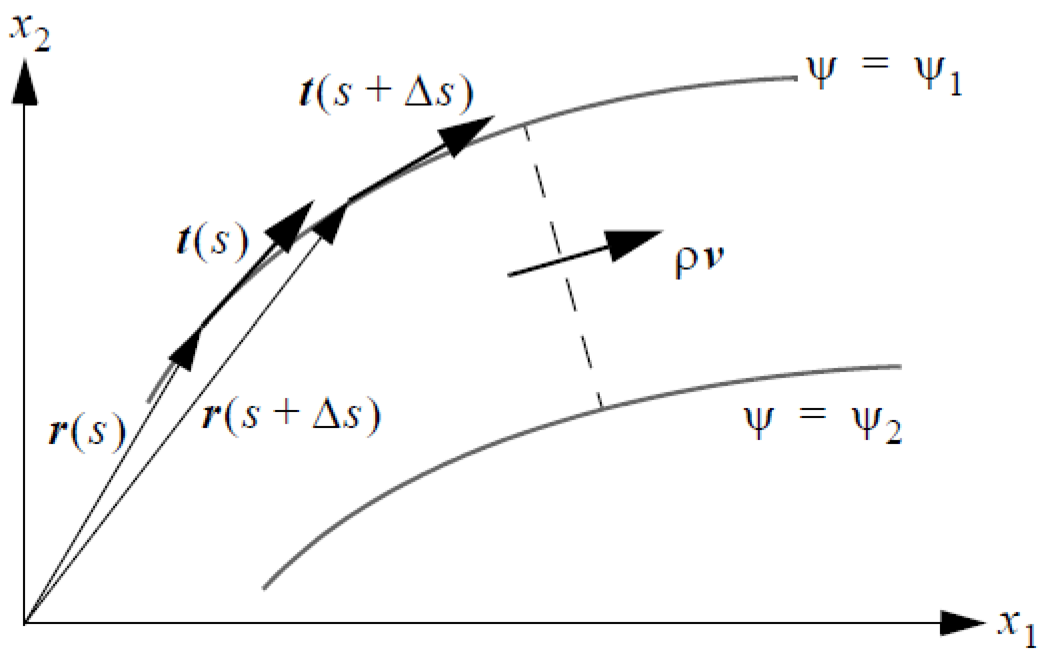

Figure 5.3 Element of surface *dA* across which a force π_n *dA* is transmitted.

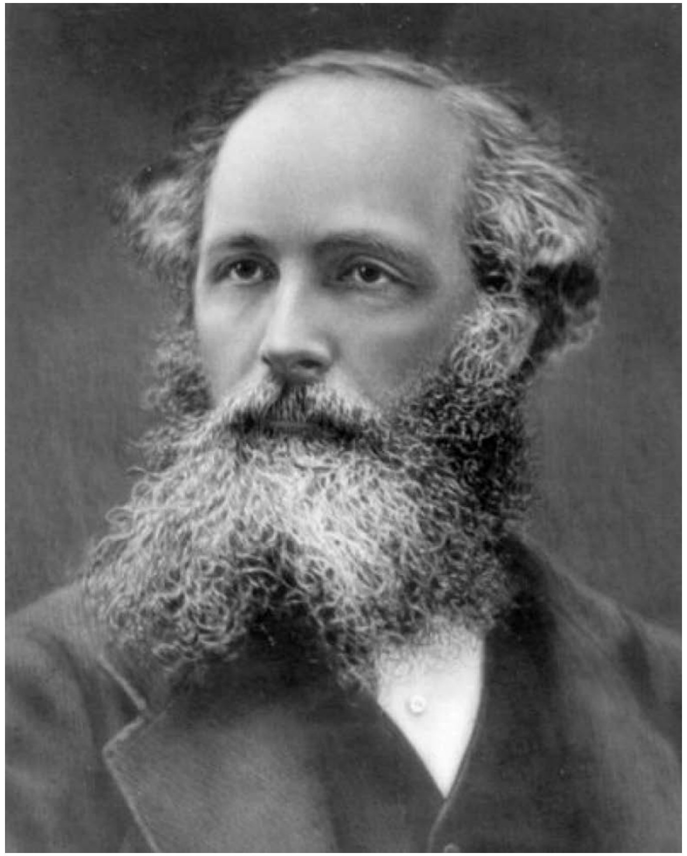

Figure 5.4 James Clerk Maxwell, 1831-1879.

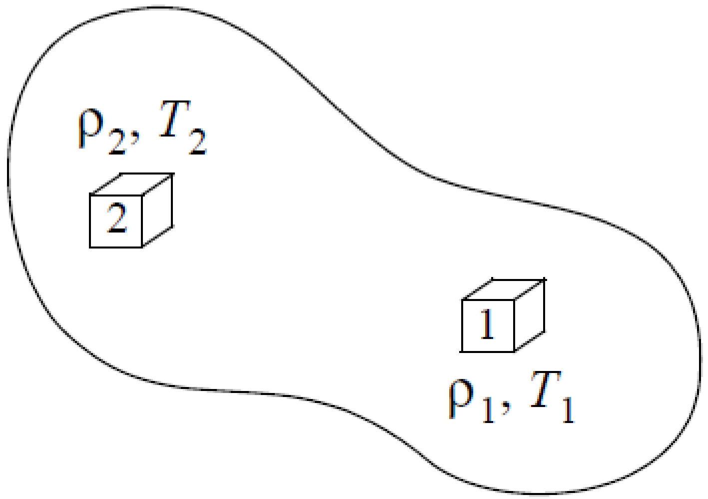

Figure 6.1 A global nonequilibrium system with local equilibrium subsystems 1 and 2.

Figure 6.2 Lars Onsager, 1903-1976.

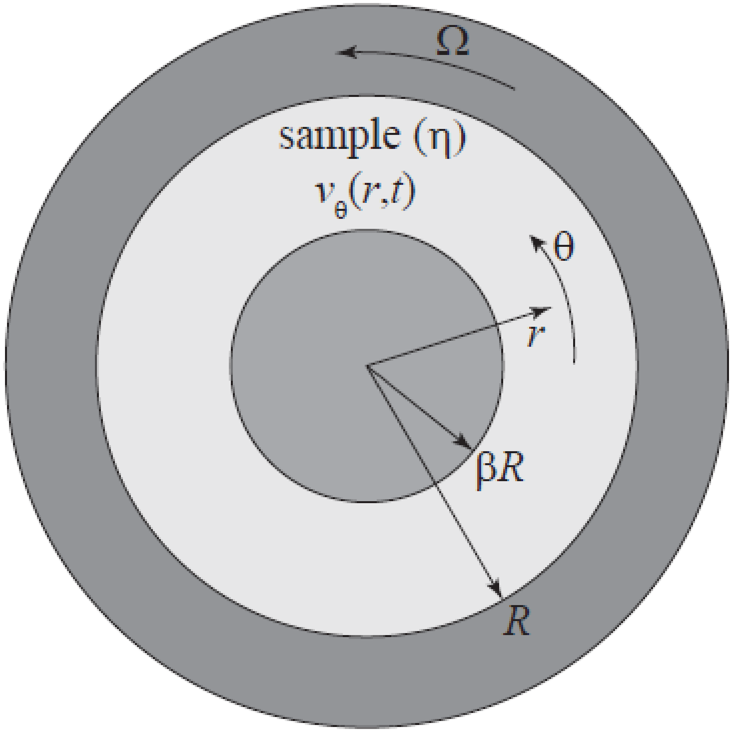

Figure 7.1 Schematic of Couette flow geometry with sample having viscosity η between stationary inner cylinder and outer cylinder rotating with angular velocity Ω..

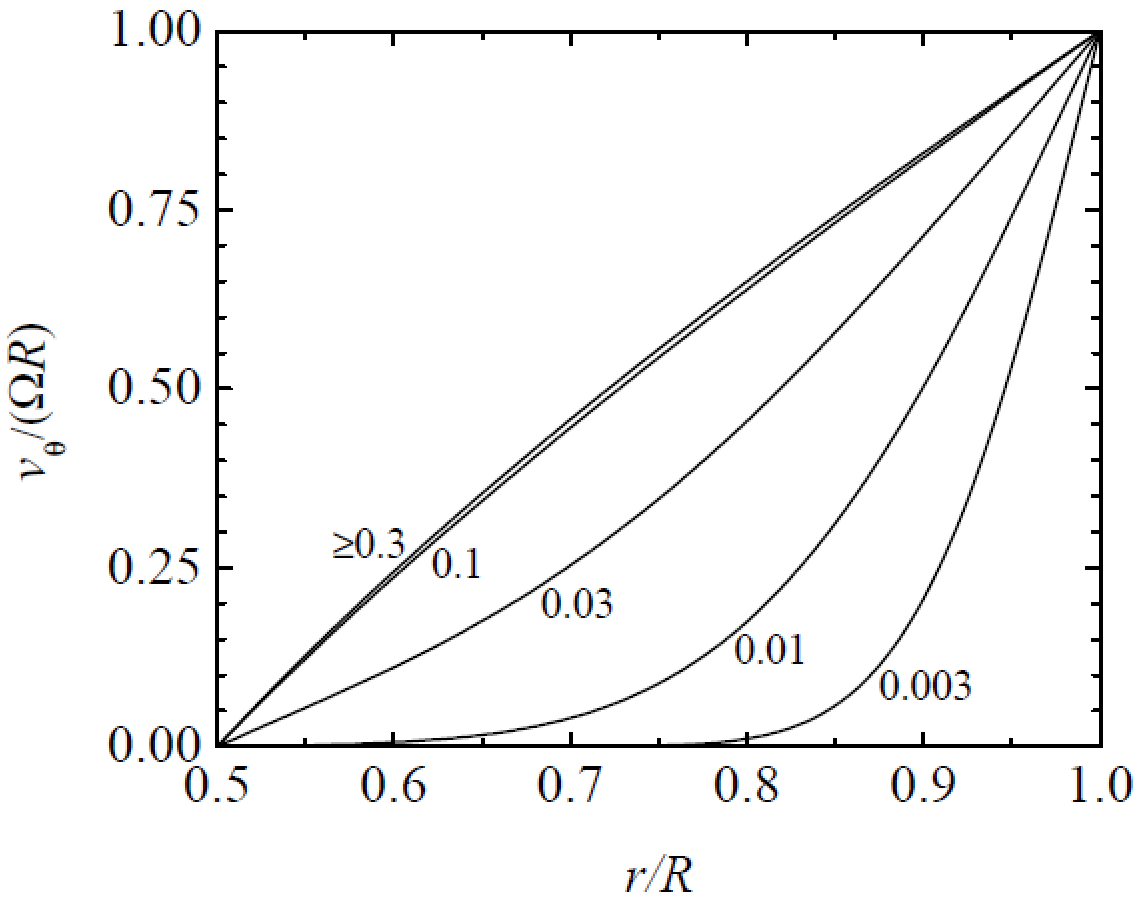

Figure 7.2 Evolution of velocity field for Couette flow of a Newtonian fluid in an annulus with β = 0:5 given by (7.12) for $\nu t/R^2$ = 0:003, 0:01, 0:03; 0:1, $\geq$ 0:3 (bottom to top).

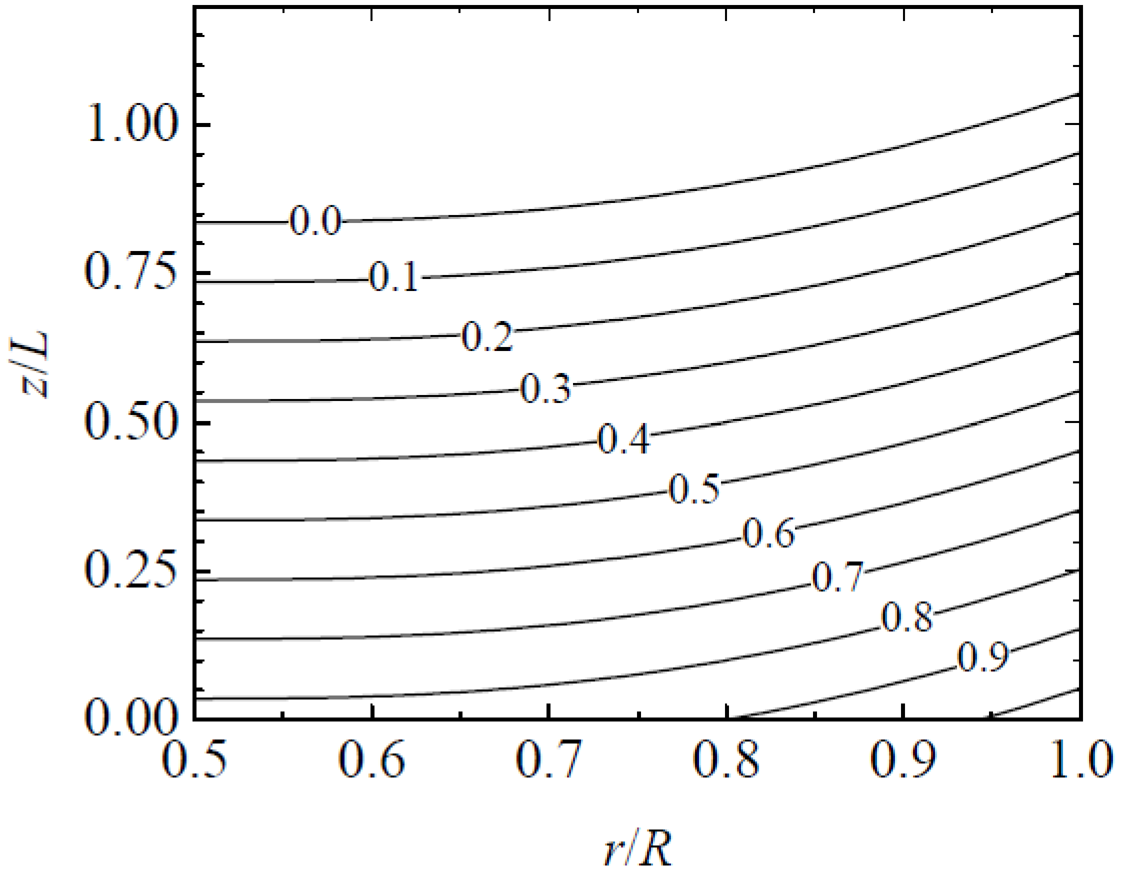

Figure 7.3 Steady-state pseudo-pressure $p^{\mathrm{L}}/(\rho\Omega^2 R^2)$ contours for Couette flow of a Newtonian fluid in an annulus given by (7.14) with β = 0:5 and N_{Fr} = 1.

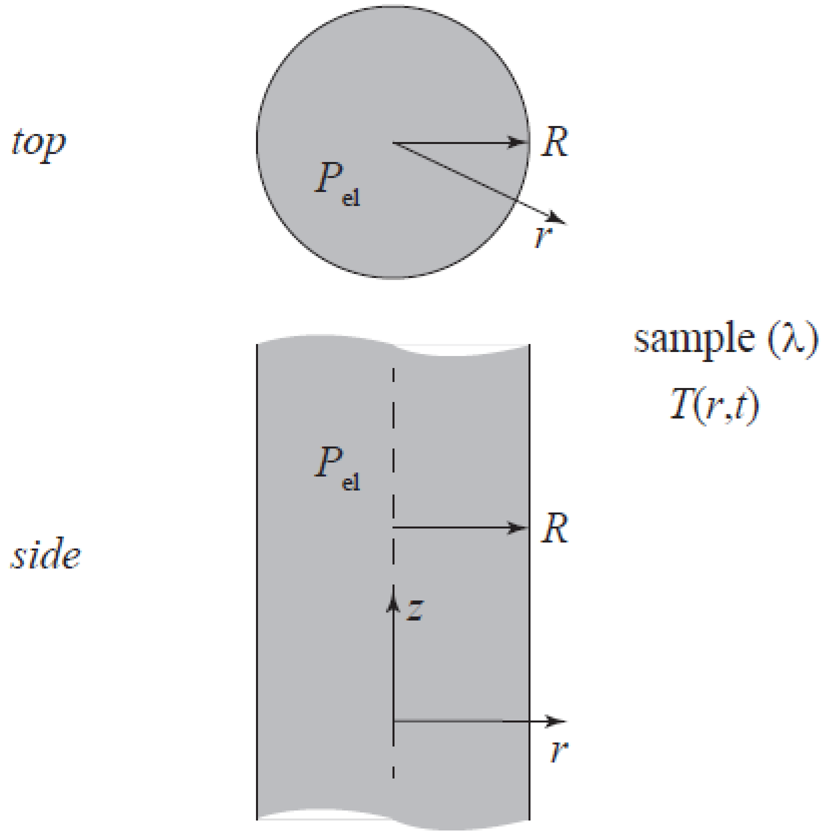

Figure 7.4 Schematic of transient hot-wire (THW) experiment with wire of radius *R* that uniformly generates energy at a rate per unit length of P_{el} surrounded by a sample with thermal conductivity λ .

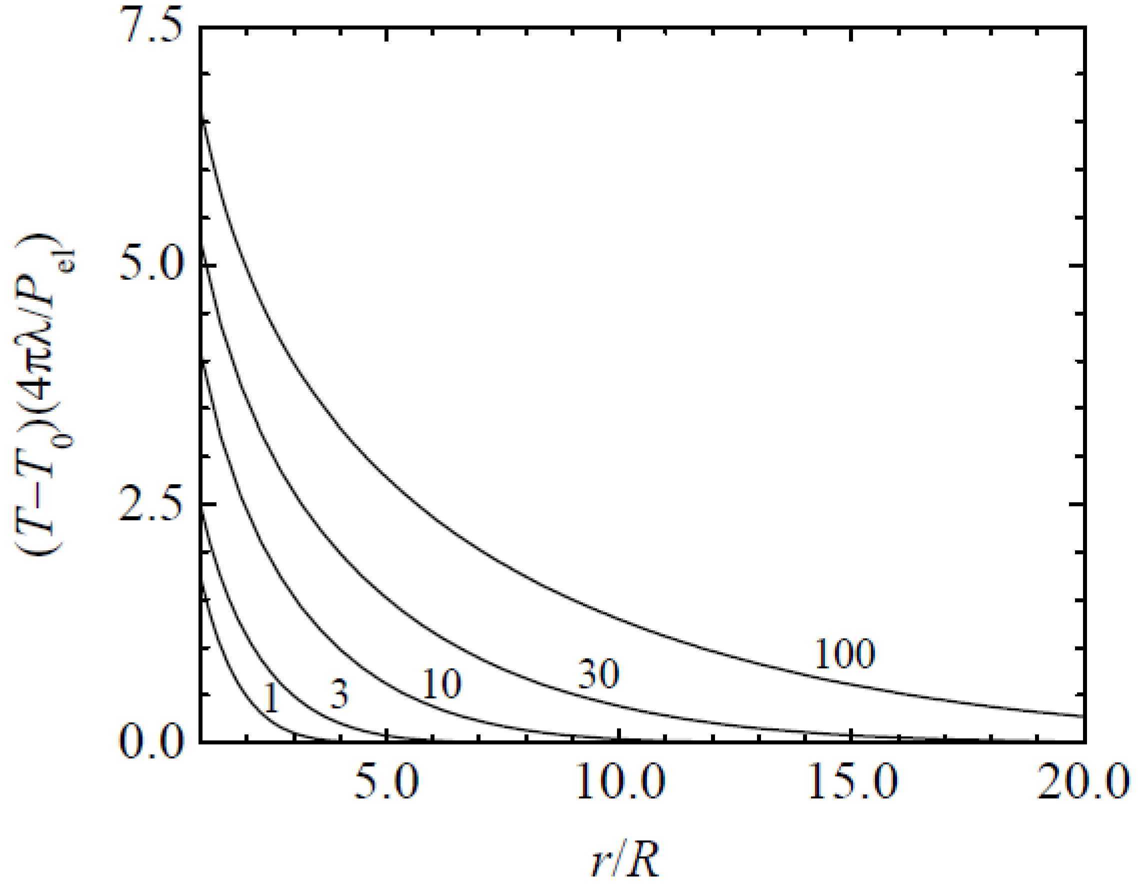

Figure 7.5 Evolution of the temperature field for THW experiment given by (7.24) for $\chi t/R^2$ = 1, 3, 10, 30, 100 (bottom to top).

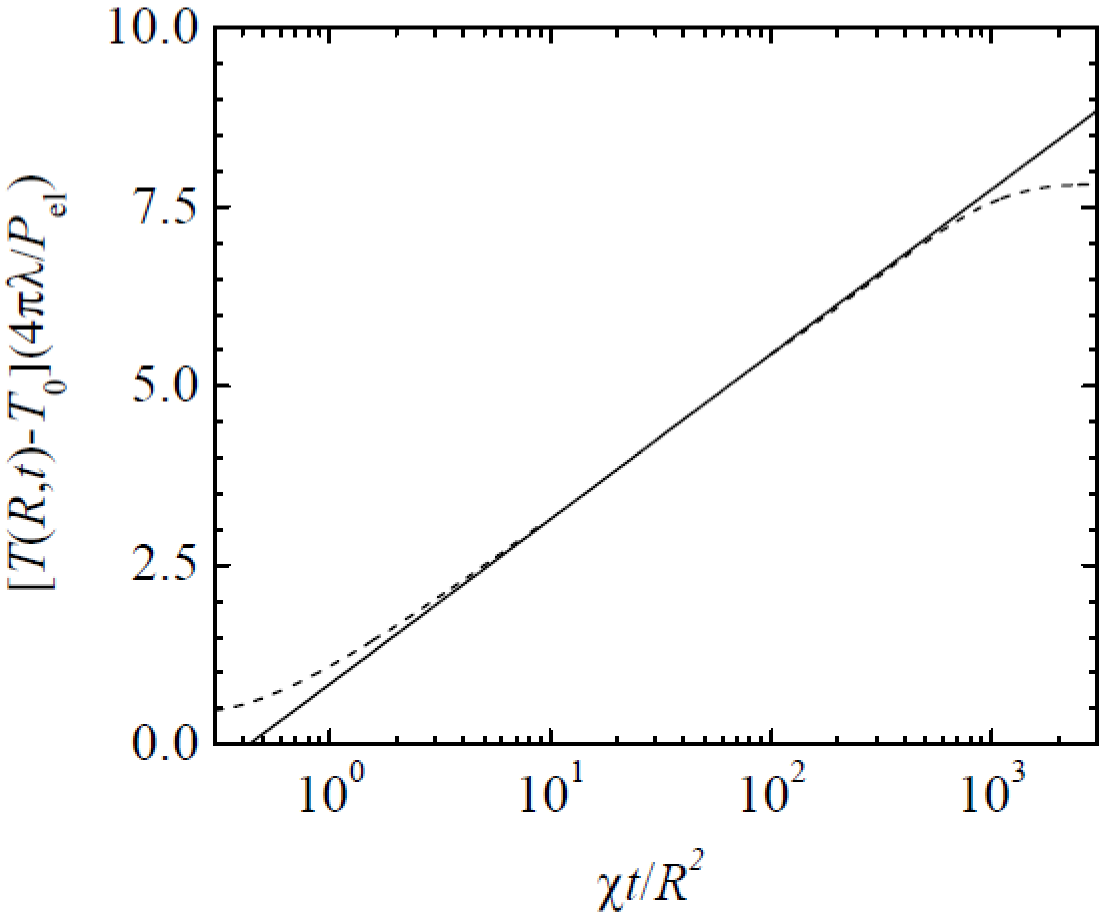

Figure 7.6 Temperature rise of wire in THW technique given by (7.25). Dashed curves at small and large times indicate non-idealities associated with finite heat capacity of the wire and the finite sample radius.

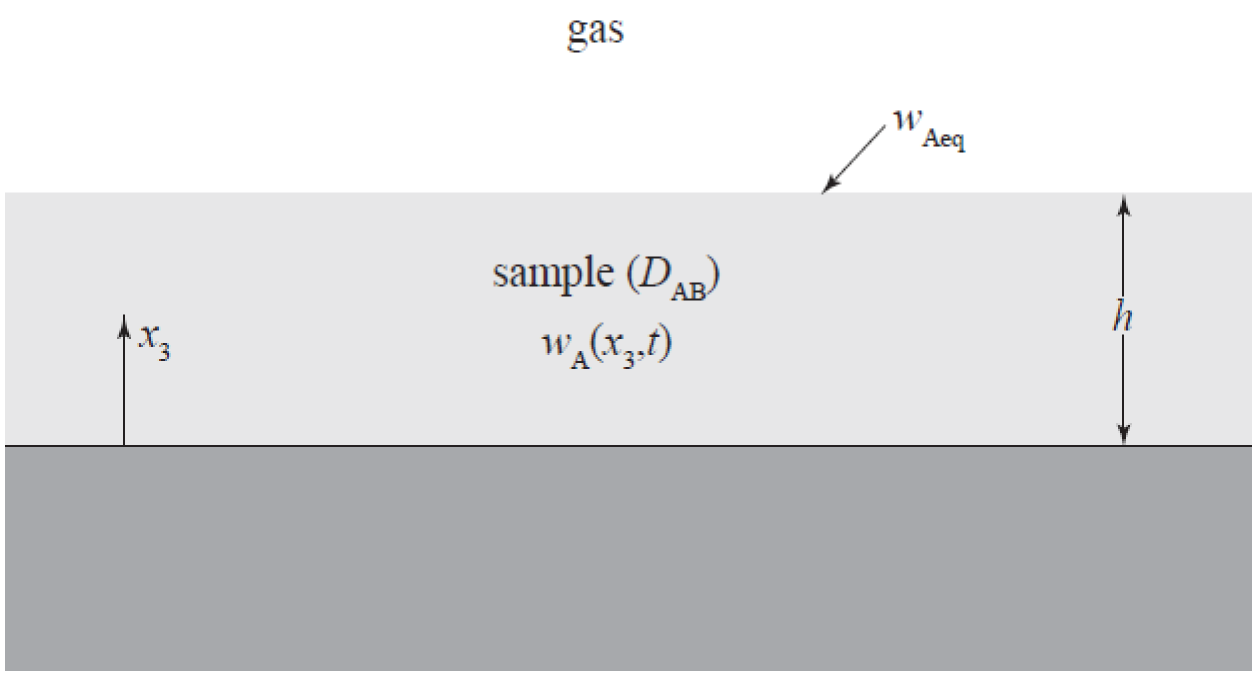

Figure 7.7 Schematic of sorption experiment with sample having mass diffusivity D_{AB} in contact with a gas that maintains the concentration w_{Aeq} at the surface $x_3 = h$.

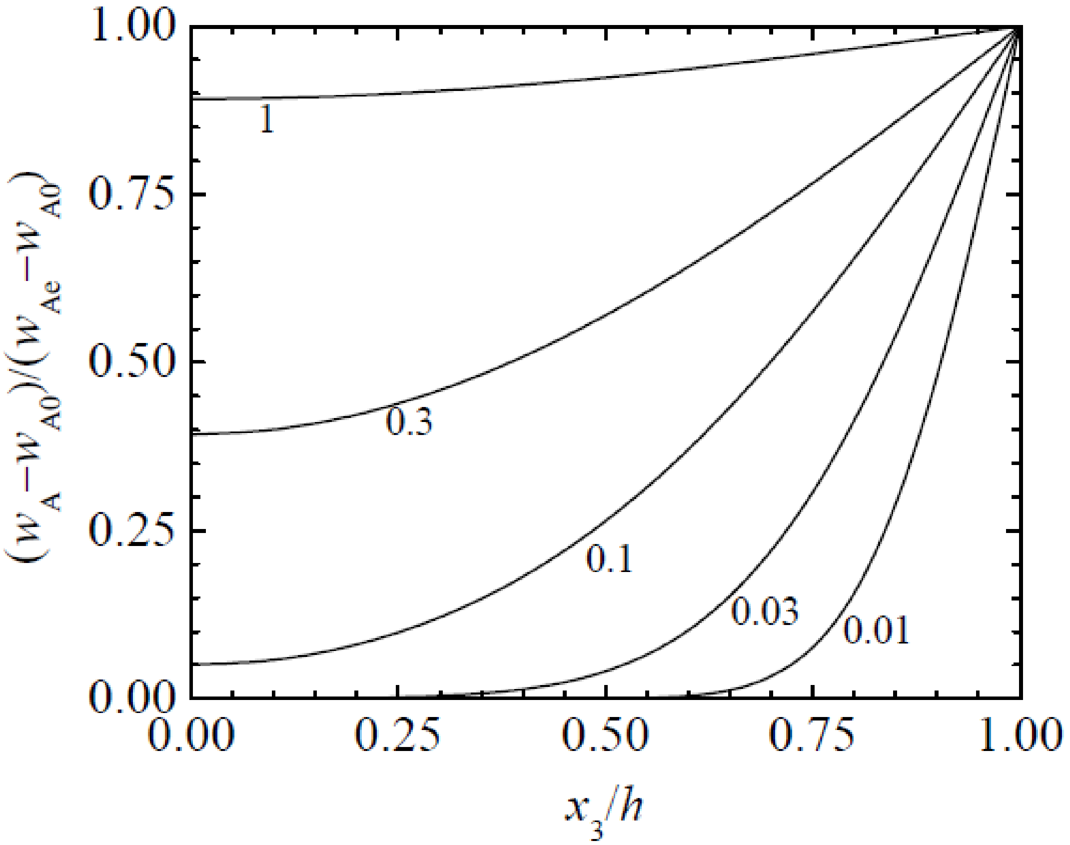

Figure 7.8 Evolution of concentration prole in sorption experiment given by (7.43) for tD_{AB}/h^2 = 0:01; 0:03; 0:1; 0:3; 1:0 (bottom to top).

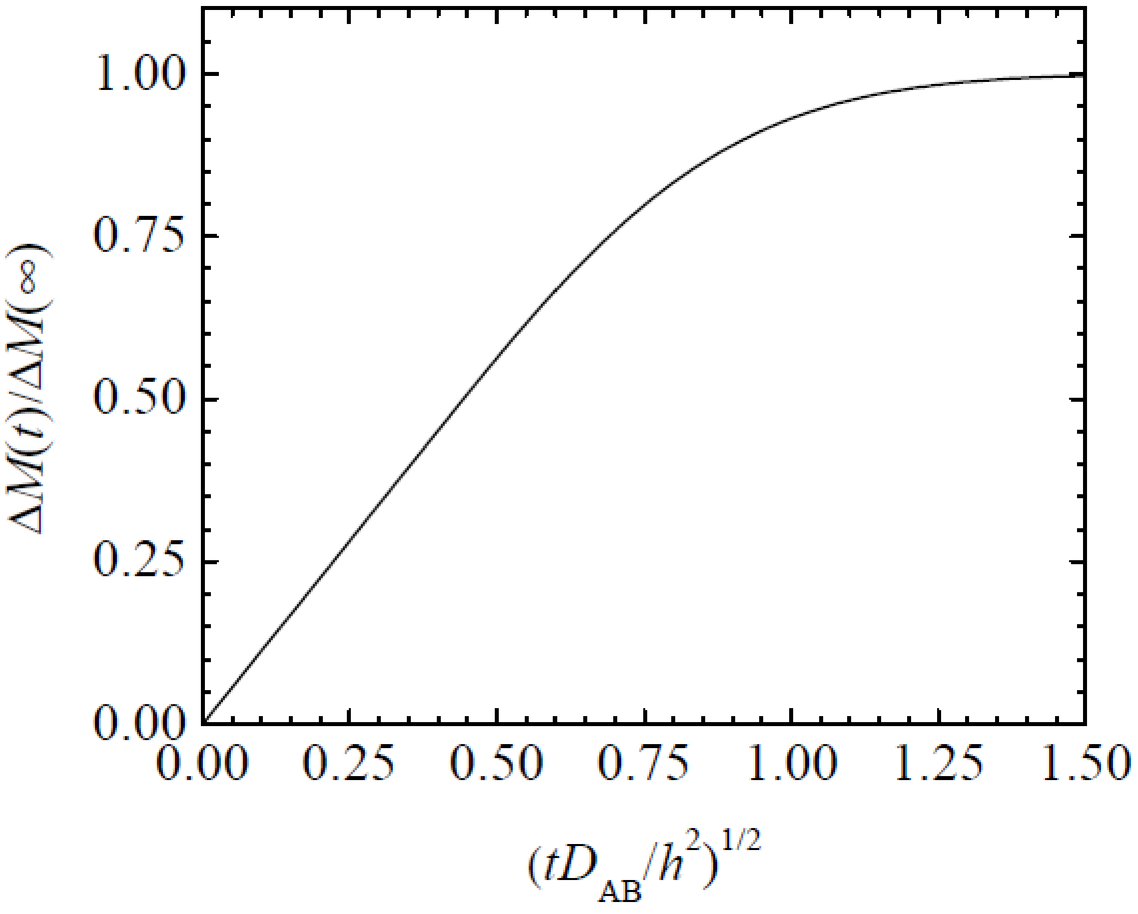

Figure 7.9 Normalized mass uptake in sorption experiment given by (7.44). The slope of the line for $tD_{AB}/h^2 \lesssim 0.5$ is $2/\sqrt{\pi}$.

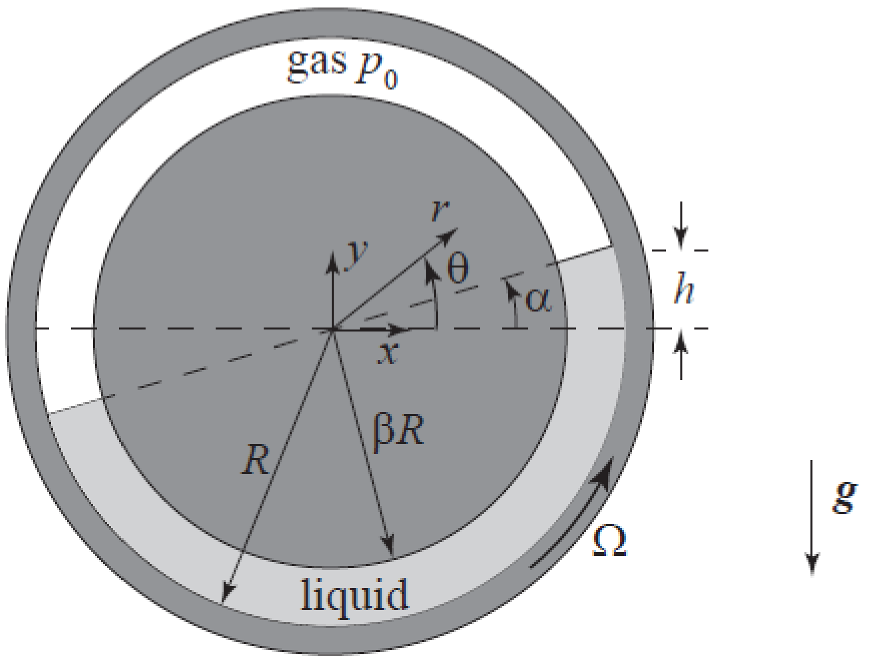

Figure 7.10 Schematic showing flow of a liquid (light shaded region) that partially fills the annular region between horizontal concentric cylinders.

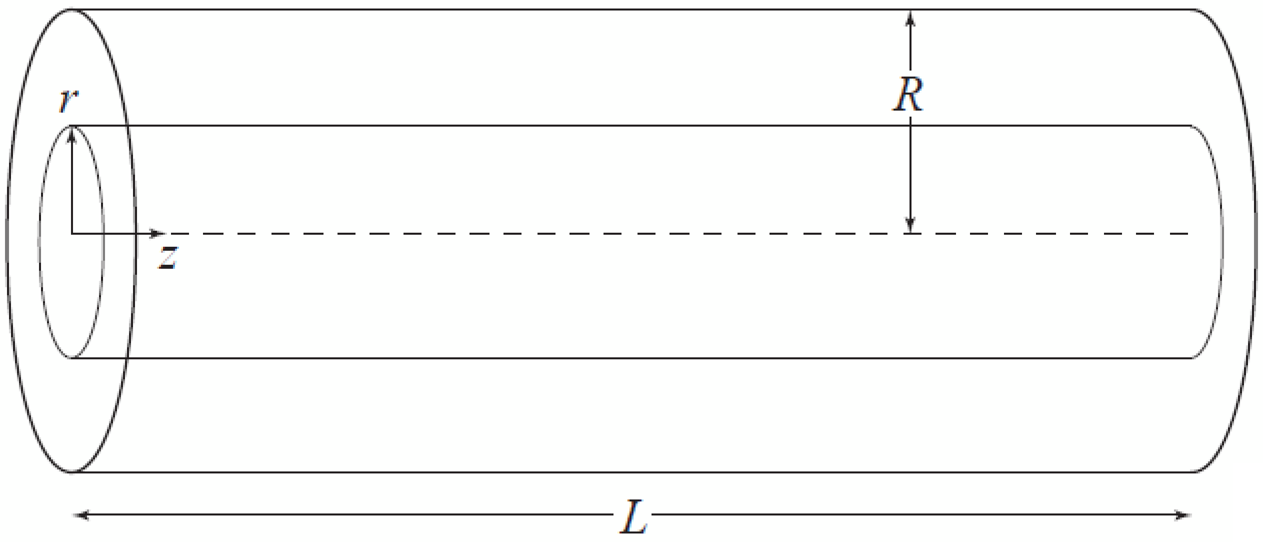

(Above) Figure 8.1 Flow in a tube showing cylindrical fluid element.

(Left) Figure 8.2 Experimental pressure drop data for gas flows in microchannels with height 2*H* and width *B* normalized by pressure drop for incompressible flow versus normalized isothermal compressibility. Different symbols correspond to different gases: N2 □, He ◯, Ar △, Air ◊ (see Venerus & Bugajsky, Phys. Fluids 22 (2010) 046101). The dashed line is the incompressible case (see Exercise 8.2) and the solid curve is given by (8.36), which is based on the lubrication approximation.

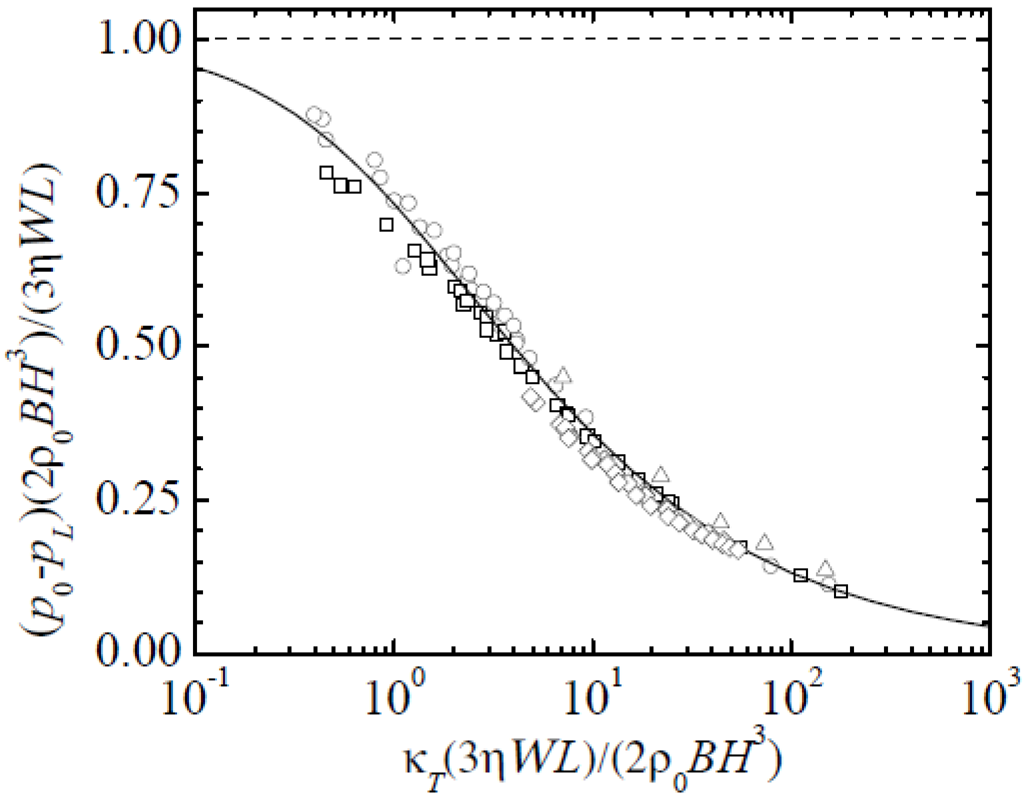

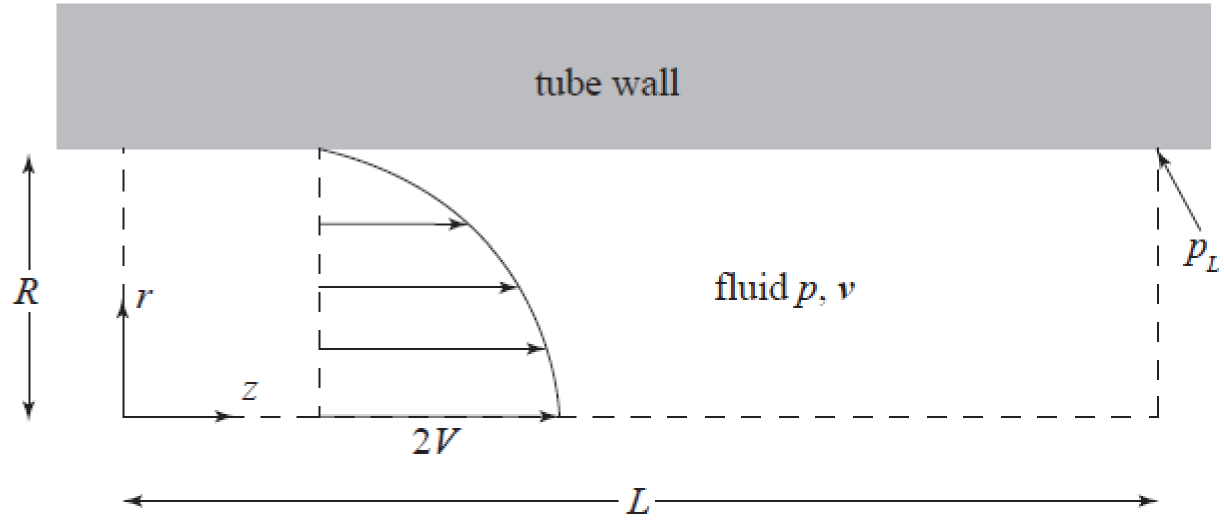

(Above) Figure 8.3 Schematic of flow in a tube of radius *R* and length *L*. Note tha
2*V* is the maximum velocity only for incompressible flow.

(Left) Figure 8.4 Axial velocity v_z/V profile for compressible flow in a tube from (8.28) for $\epsilon = \beta/80$ and ϵN_{Re} = 1/8 or N_{Ma} = 1/4 (solid lines) for z/L = 0, 0:5, 1 (bottom to top). The dashed line is for the incompressible case, ϵ = 0.

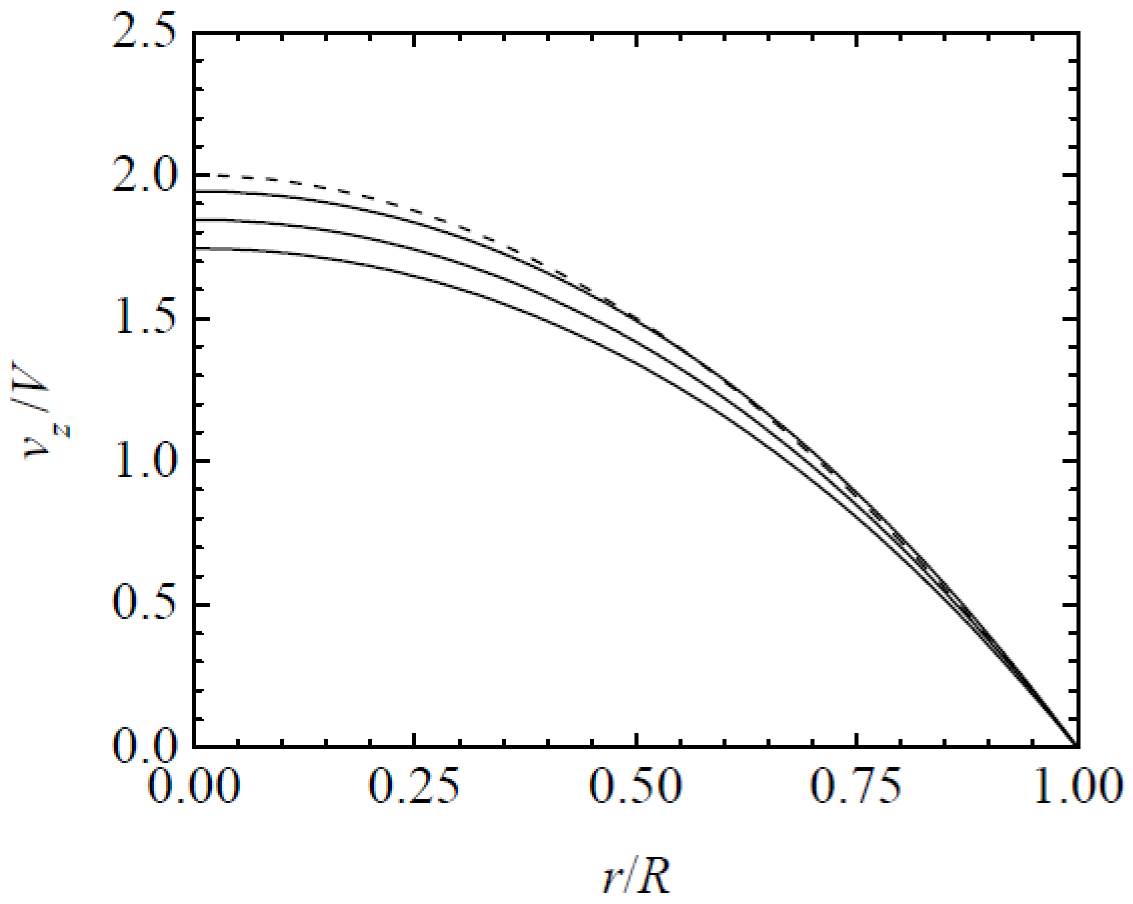

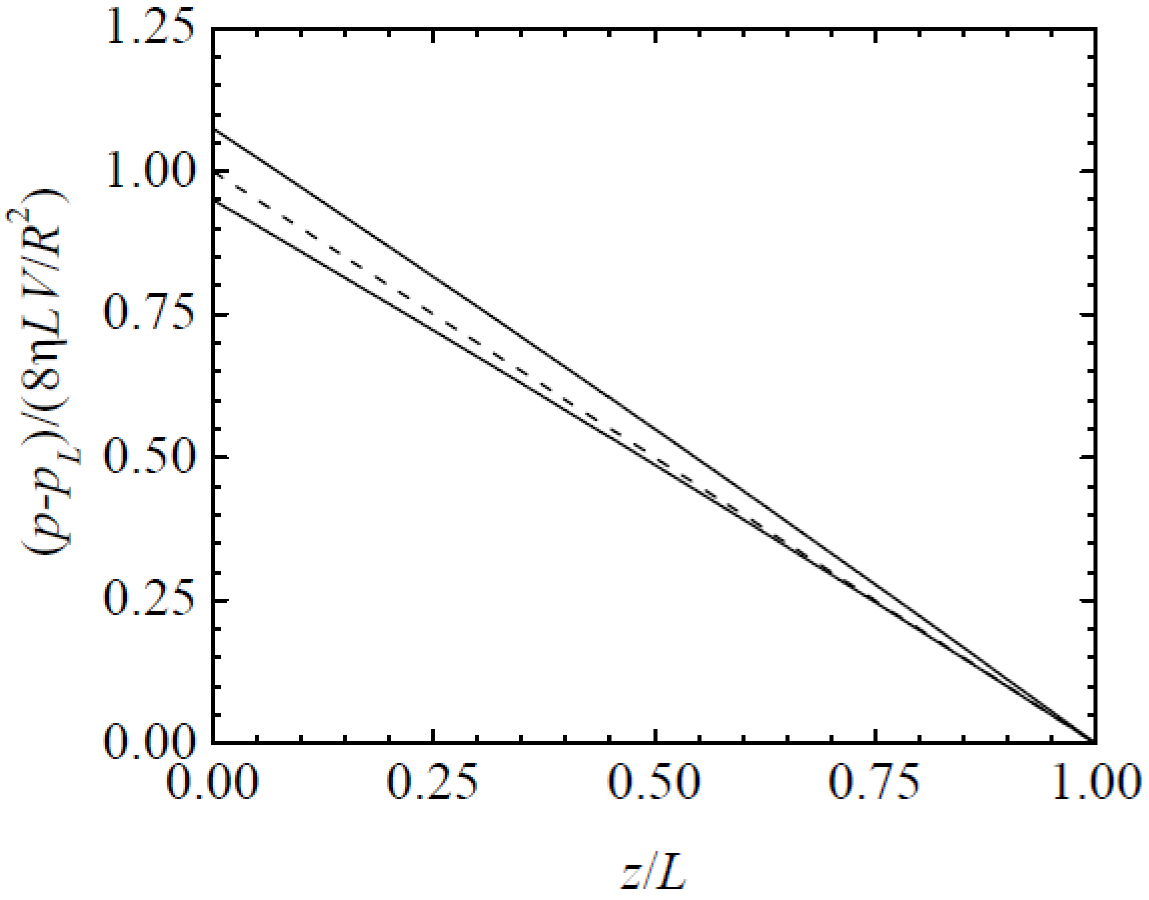

Figure 8.5 Pressure $(p-p_L)/(8\eta V L/R^2)$profile for compressible flow in a tube from (8.29) for $\epsilon = \beta/80$ and ϵN_{Re} = 0 (bottom curve) and ϵN_{Re} = 1/8 (top curve). The dashed line is for the incompressible case, ϵ = 0.

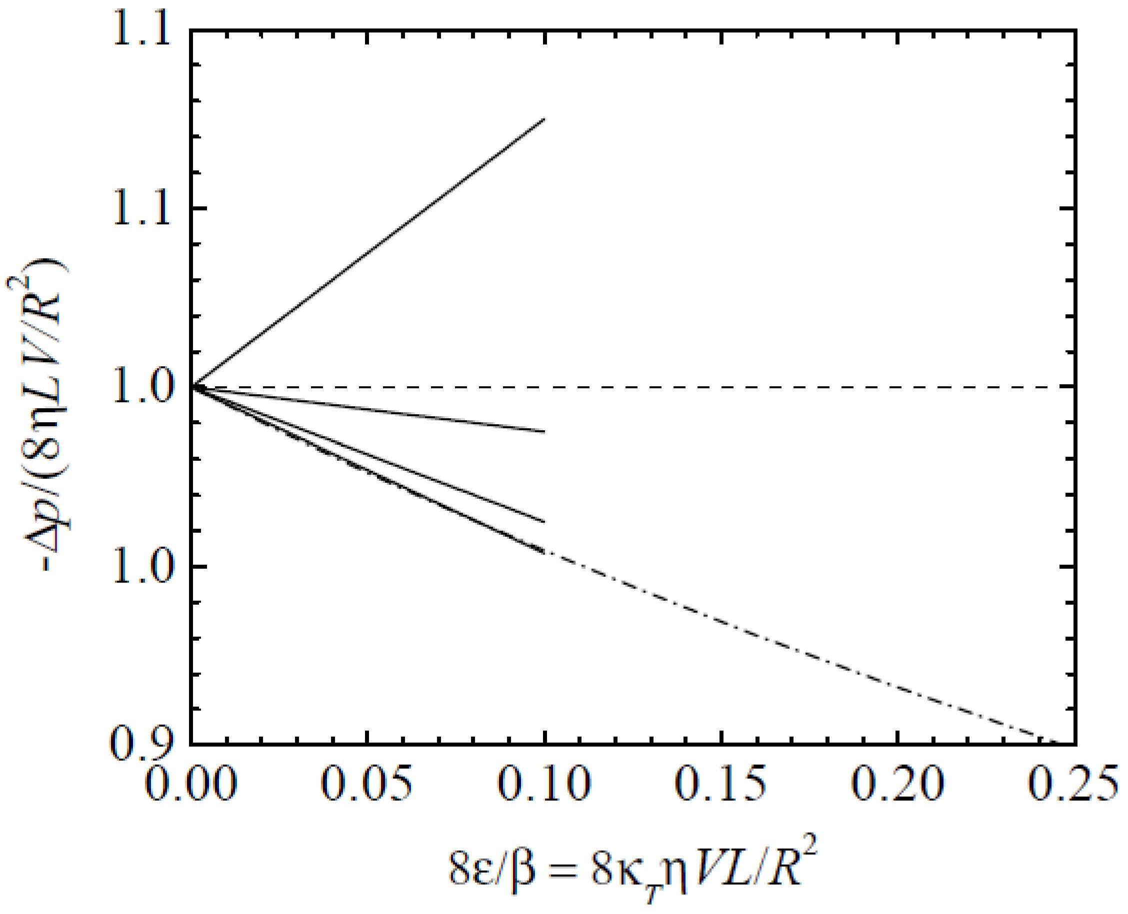

Figure 8.6 Normalized pressure drop for compressible flow in a tube from (8.30) for four values of $\beta N_{\mathrm{Re}}/8$ = 0:3, 1, 3, 10 (solid lines from bottom to top). The dash-dotted line is from the lubrication approximation (8.36). The dashed line is for the incompressible case, ϵ = 0.

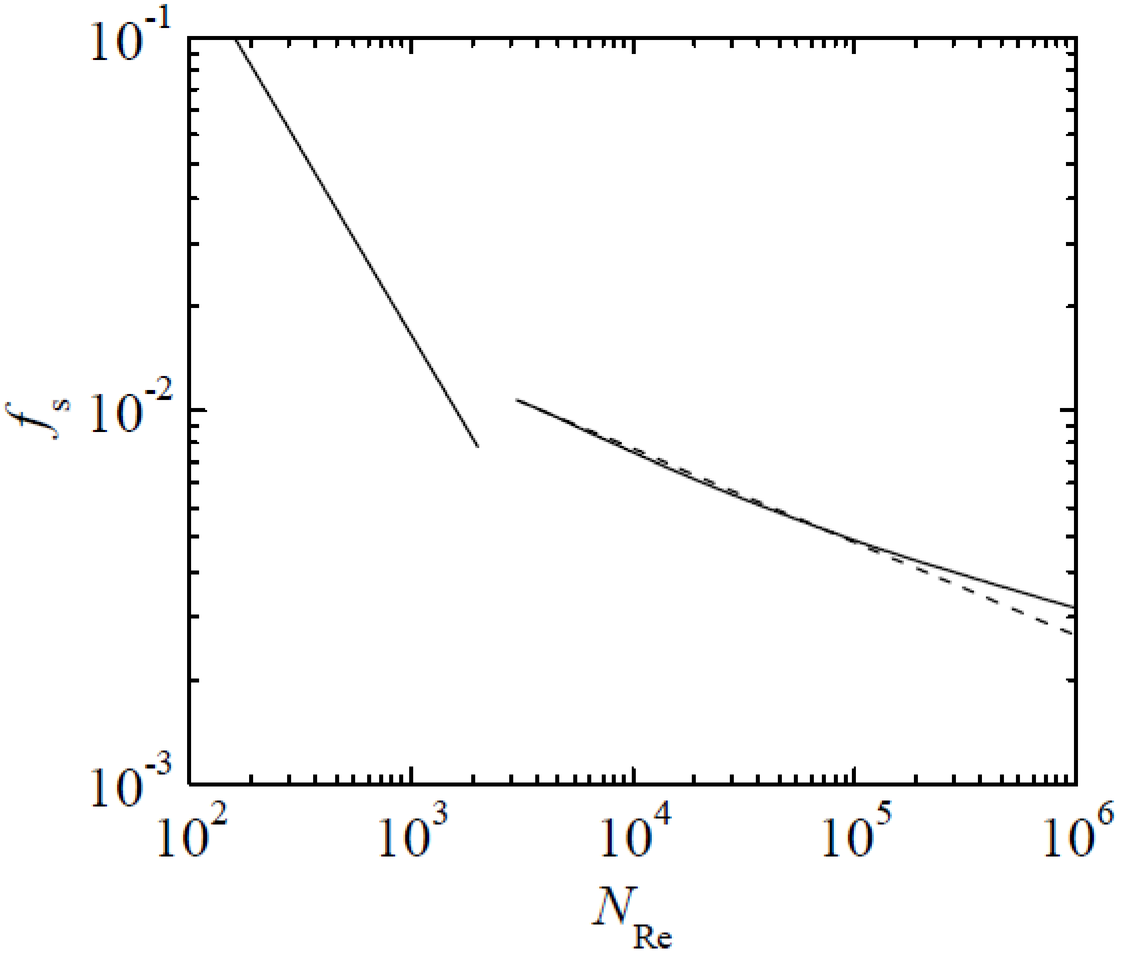

Figure 8.7 Friction factor f_s versus Reynolds number N_{Re} for incompressible flow in a smooth tube. The solid line for laminar flow $(N_{\mathrm{Re}} \lesssim 2000)$ is from (8.38). For turbulent flow $(N_{\mathrm{Re}} \gtrsim 3000)$, the solid line is from (8.42) and the dashed line is from (8.43).

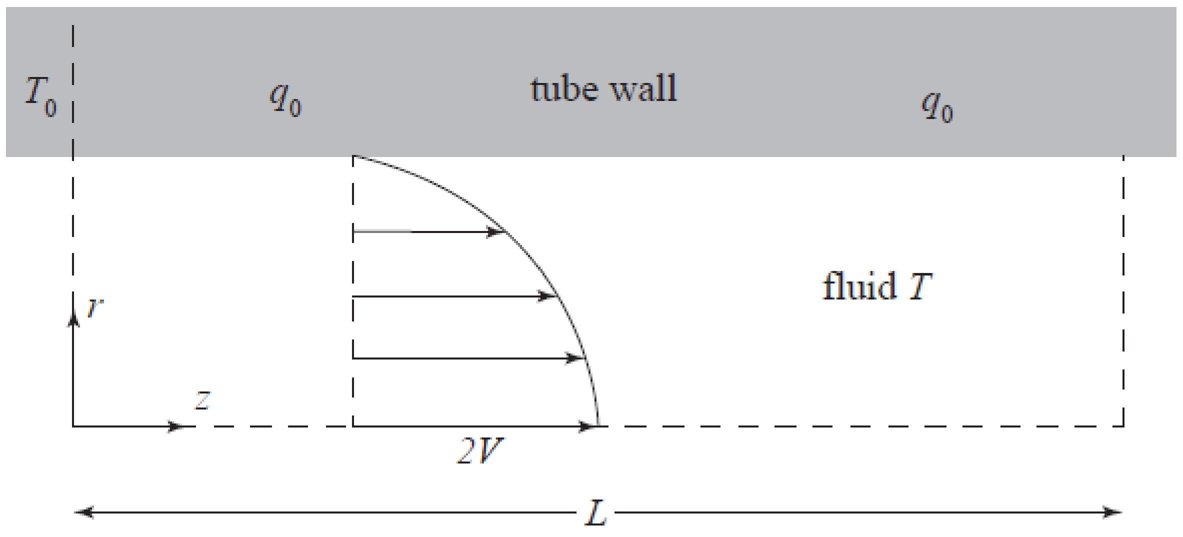

Figure 9.1 Schematic of forced convection in a heated tube.

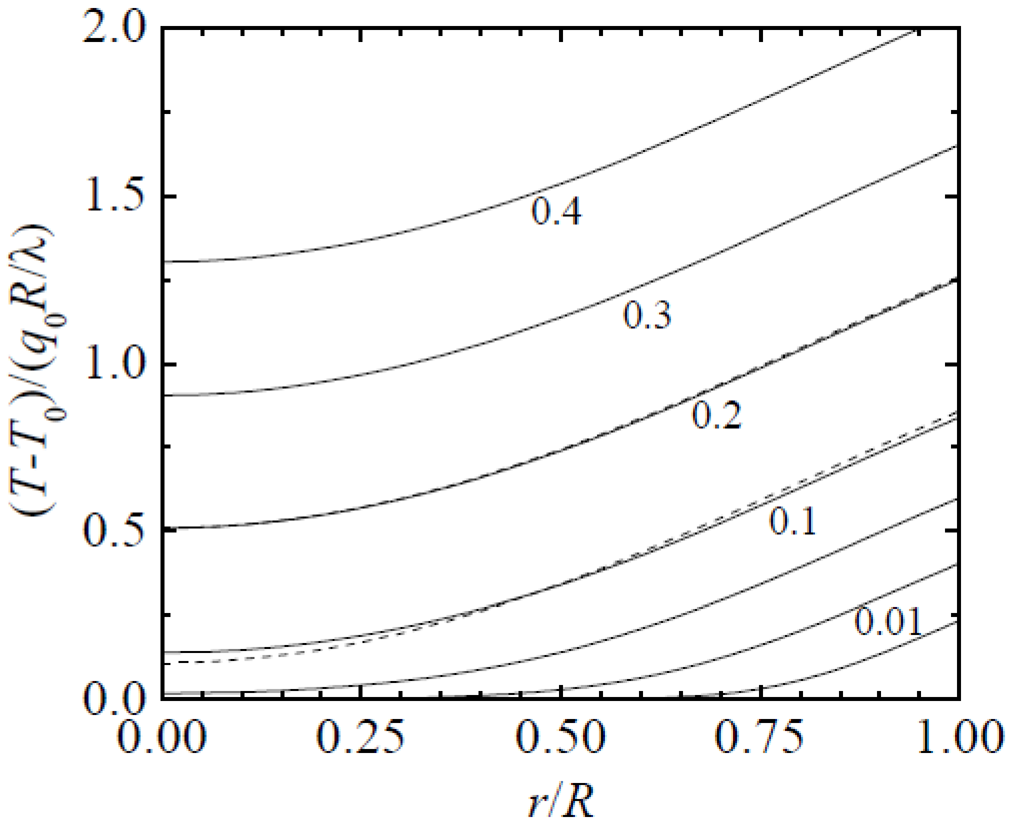

Figure 9.2 Temperature field $T(r,\bar{z})$ for laminar flow in a heated tube for $\bar{z} = z/(RN'_{\mathrm{Pe}})$ = 0:005, 0:01, 0:05, 0:1, 0:2, 0:3, 0:4 (bottom to top). Also shown for $\bar{z} \geq$ 0:1 (dashed lines) is the temperature from (9.10).

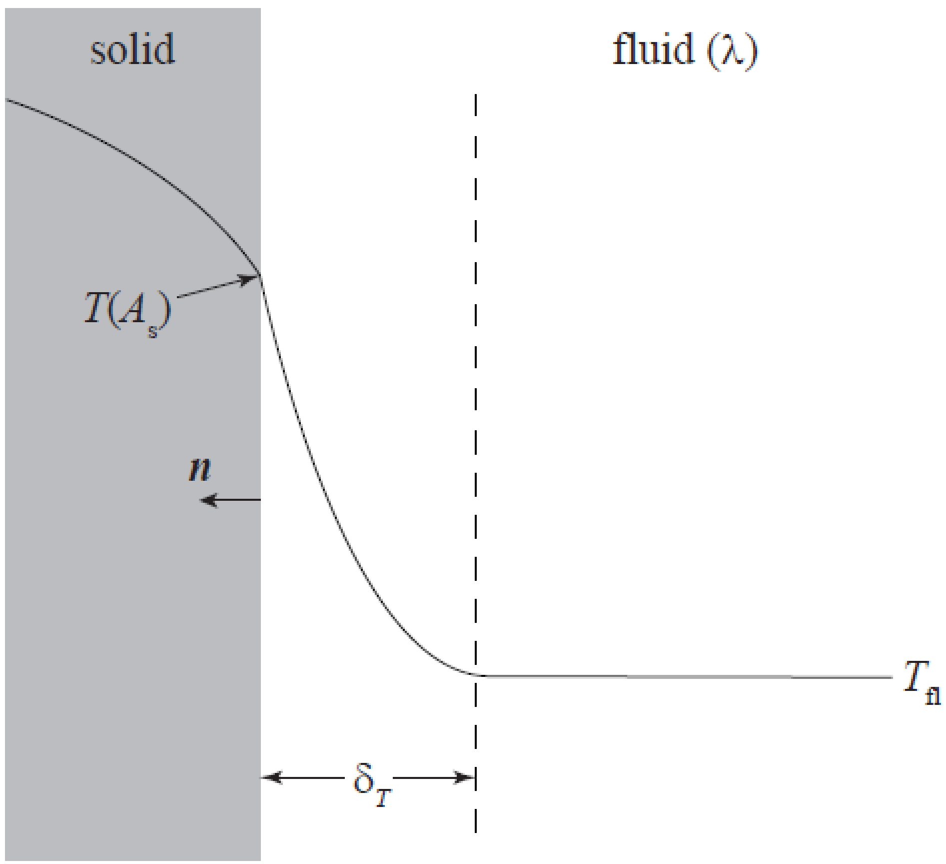

Figure 9.3 Schematic temperature profile across interface between solid and fluid phases showing thermal boundary layer with thickness δ_T.

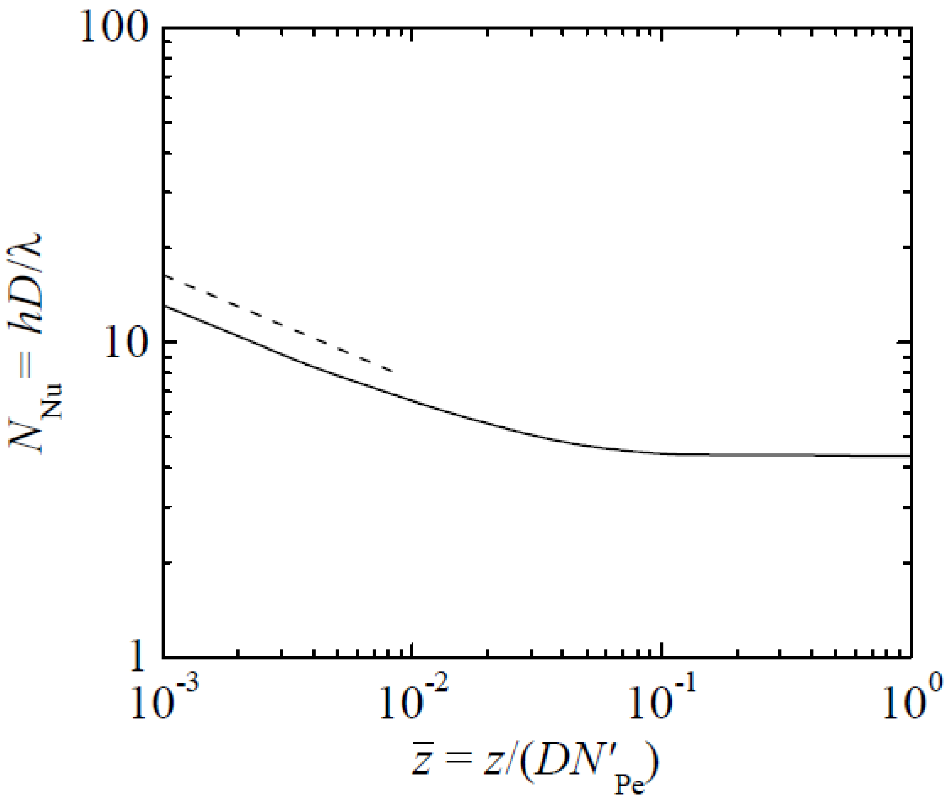

Figure 9.4 Nusselt number N_{Nu} as a function of axial position $\bar{z}$ for laminar flow in a heated tube from (9.30) The dashed line is from the asymptotic solution given in (9.31).

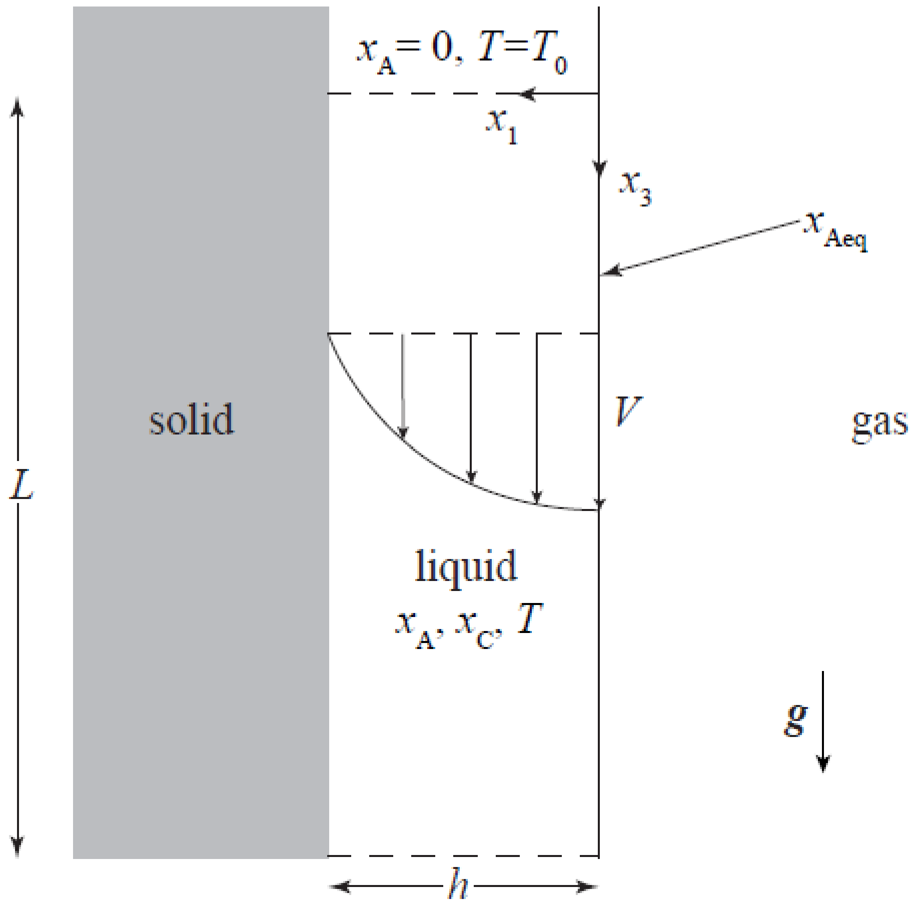

Figure 10.1 Schematic of gas absorption with homogeneous chemical reaction in a liquid film flowing along a vertical solid surface.

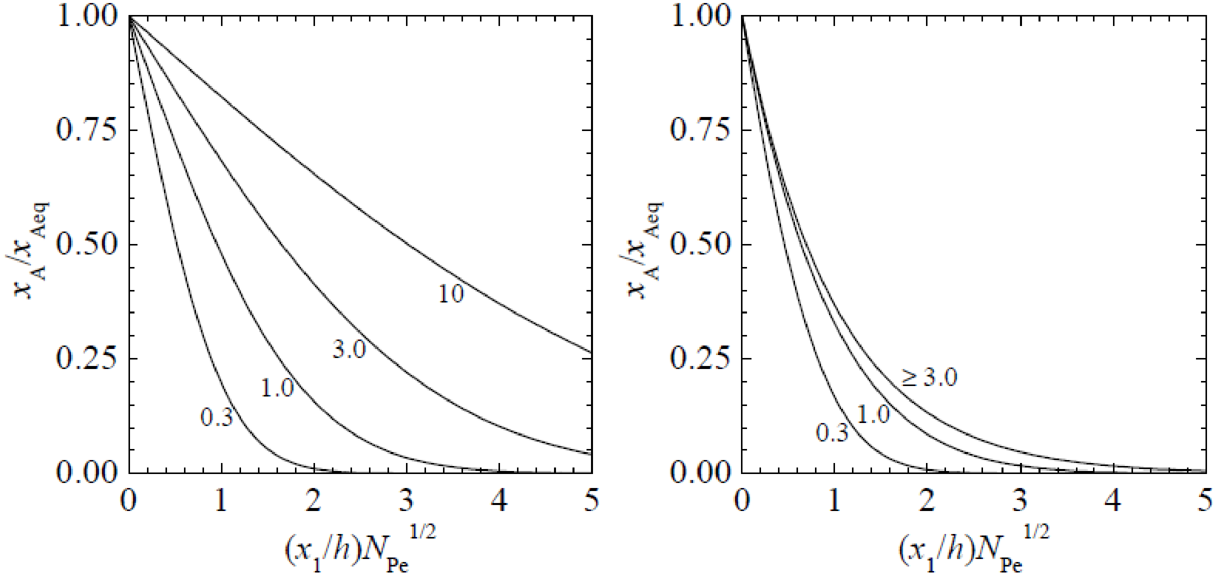

(Above) Figure 10.2 Species A concentration profile from (10.27) for gas absorption without N_{Da} = 0 (left), and with N_{Da} = 1 (right), homogeneous chemical reaction at several locations along film: x_3/h = 0:3; 1; 3; 10.

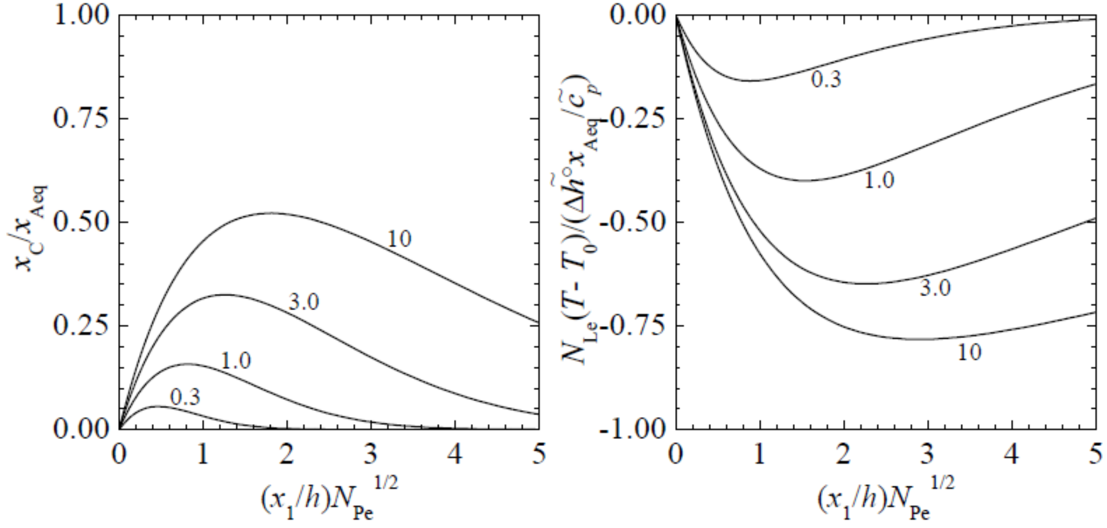

(Left) Figure 10.3 Species C concentration profile (left) from (10.30) and temperature prole (right) from (10.33) with N_{Le} = 10 for gas absorption with homogeneous chemical reaction with N_{Da} = 1 at several locations along film: $\breve{x}_3/L$ = 0:3, 1, 3, 10.

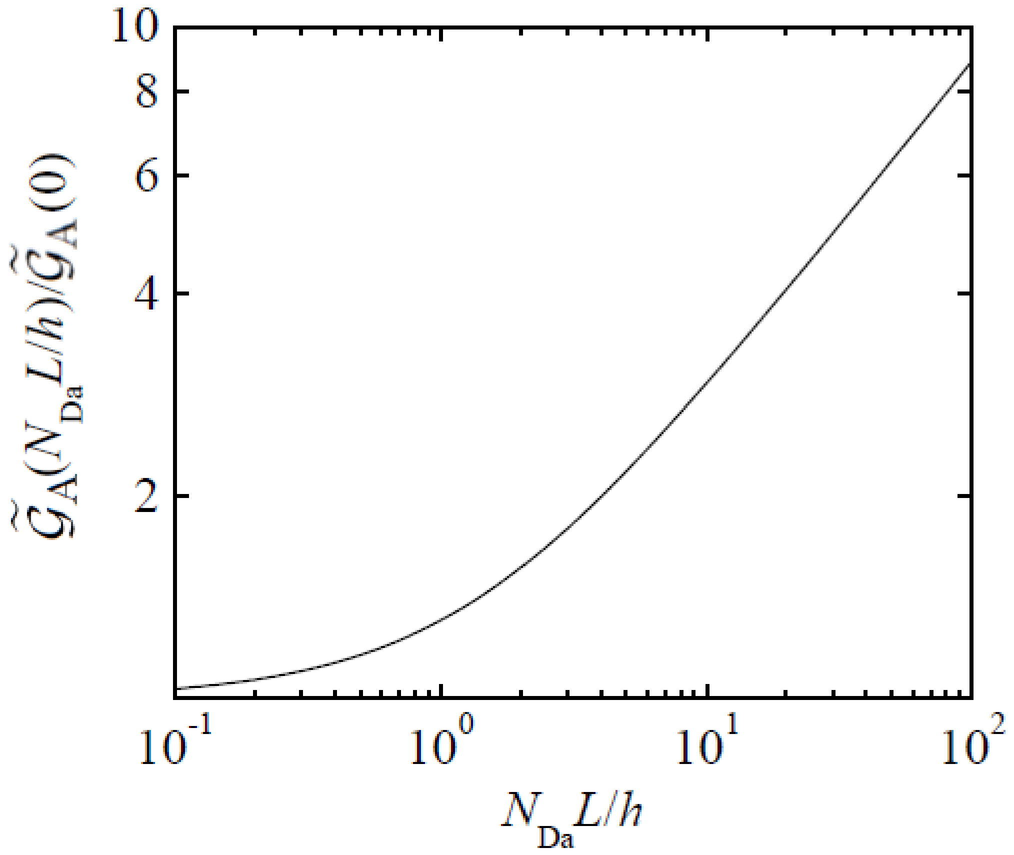

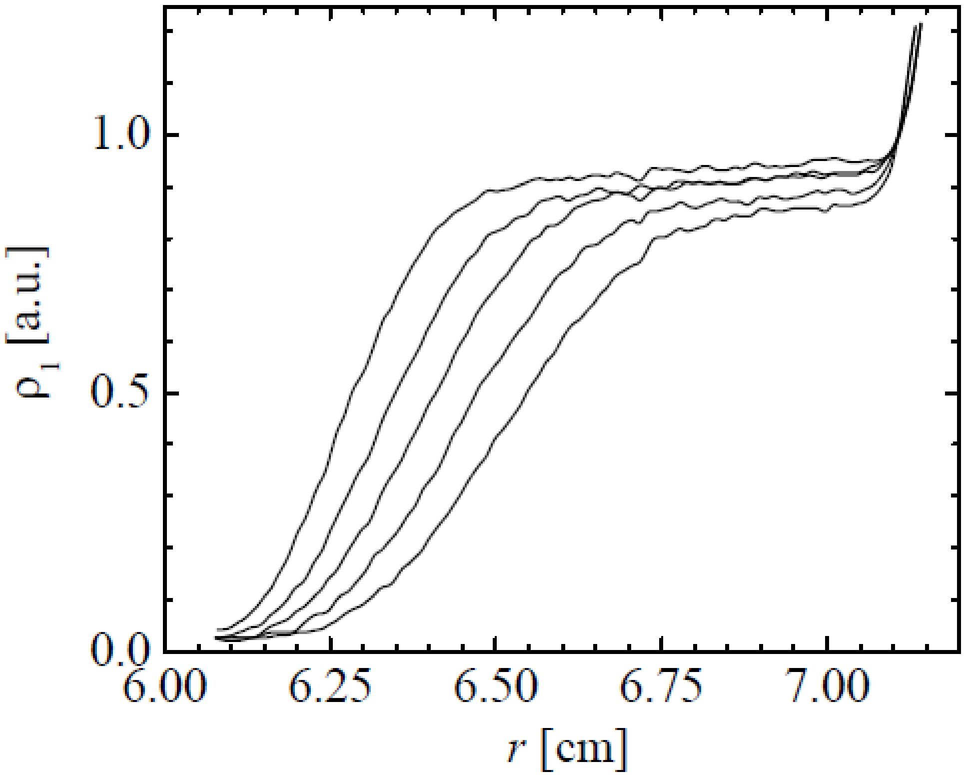

Figure 10.4 The dependence of molar rate of absorption $\widetilde{\mathcal{G}}_A$ on reaction rate and film length $N_{Da}L/h$ as given by (10.35).

Figure 11.1 Concentration of the enzyme RNase A as function of position within sample cell for different times (increasing from left to right at 20 min intervals) for an analytic ultracentrifuge experiment run at 20˚C, pH 6.5, and rotation rate of 60,000 revolutions per min. [Adapted from Laue & Staord, *Annu. Rev. Biophys. Biomol. Struct*. 28 (1999) 75.]

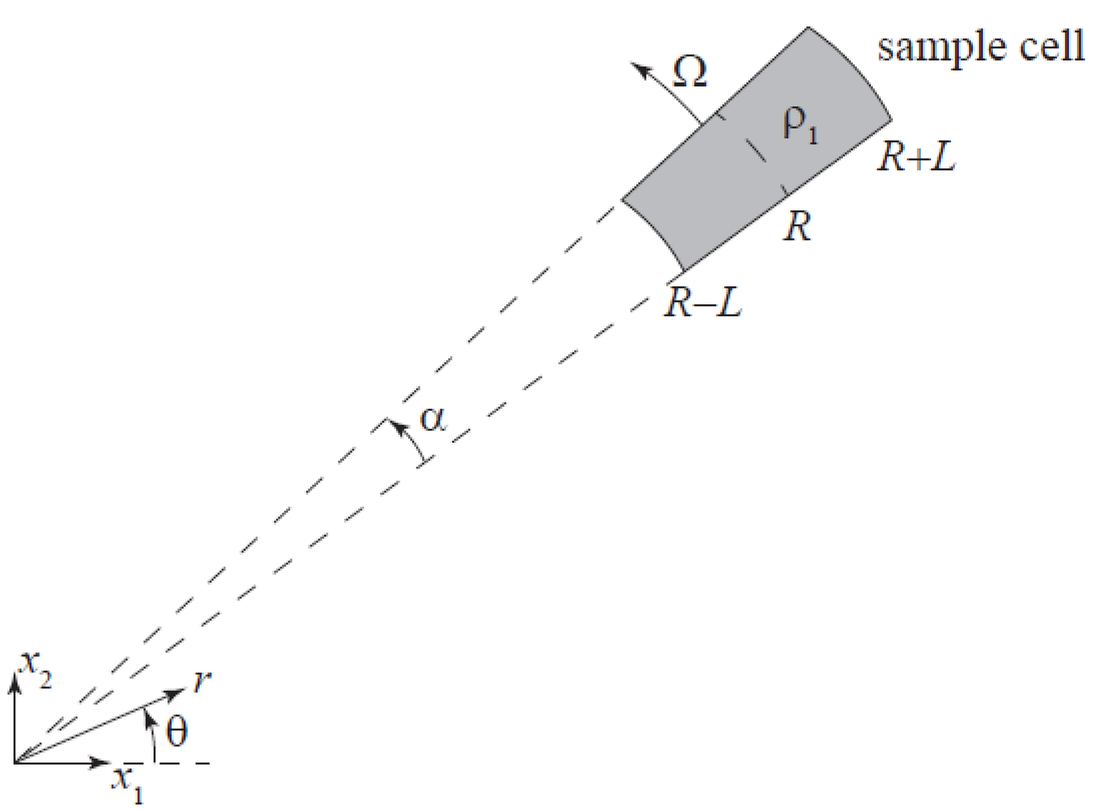

Figure 11.2 Schematic of centrifuge with sample cell rotating with angular velocity Ω. The sample occupies the region between $R - L \leq r \leq R + L$ and has solute concentration $\rho_1 = \rho w_1$.

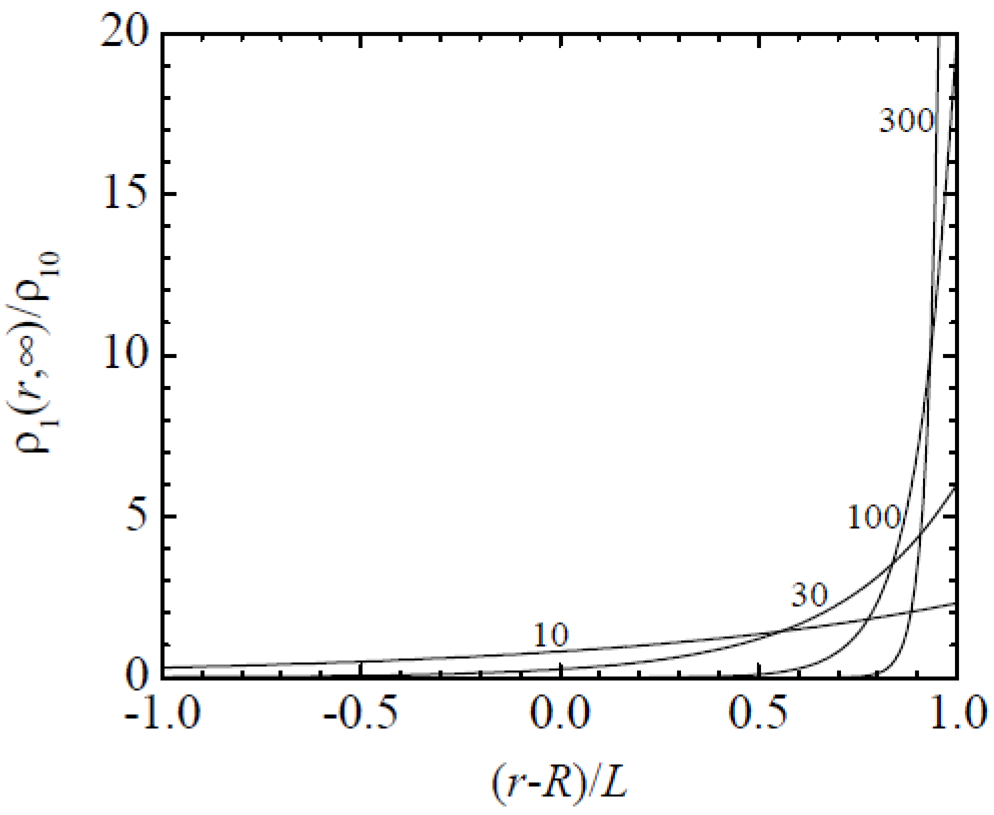

Figure 11.3 Steady state concentration field for an ultracentrifuge from (11.30) with β = 0:1 for Λ_p = 10, 30, 100, 300.

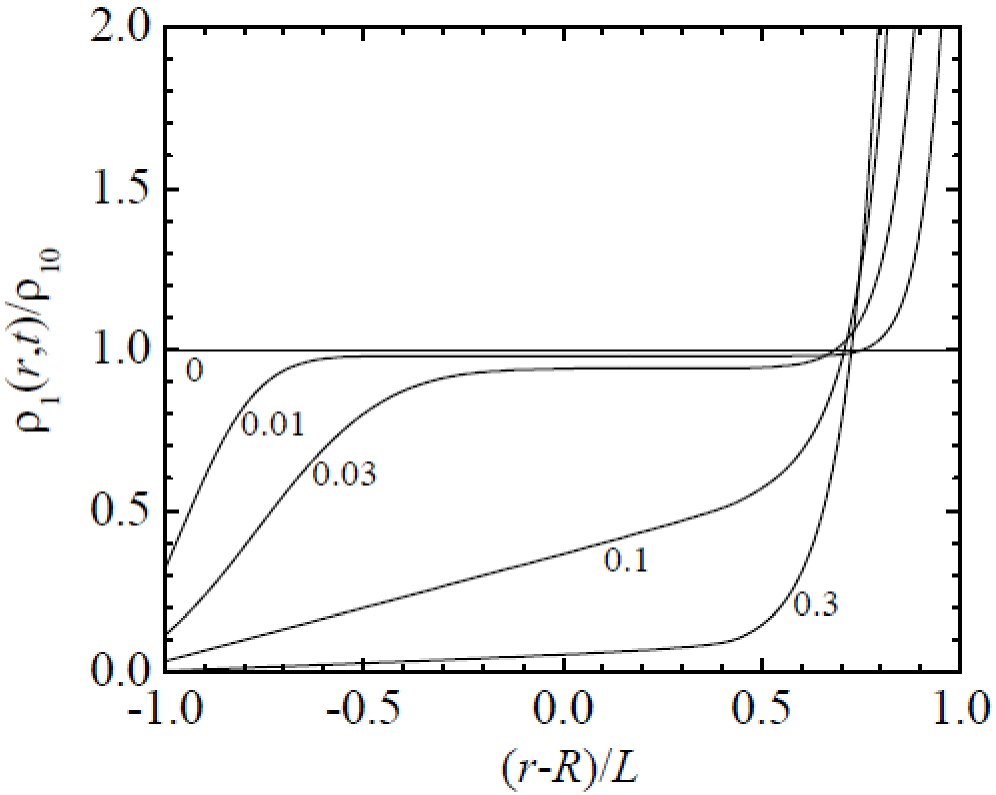

Figure 11.4 Time evolution of the solute concentration field for an ultracentrifuge obtained from numerical solution of (11.15)-(11.17) with β = 0.1 and Λ_p = 100 for different times tD_{12}/L^2 = 0, 0.01, 0.03, 0.1, 0.3.

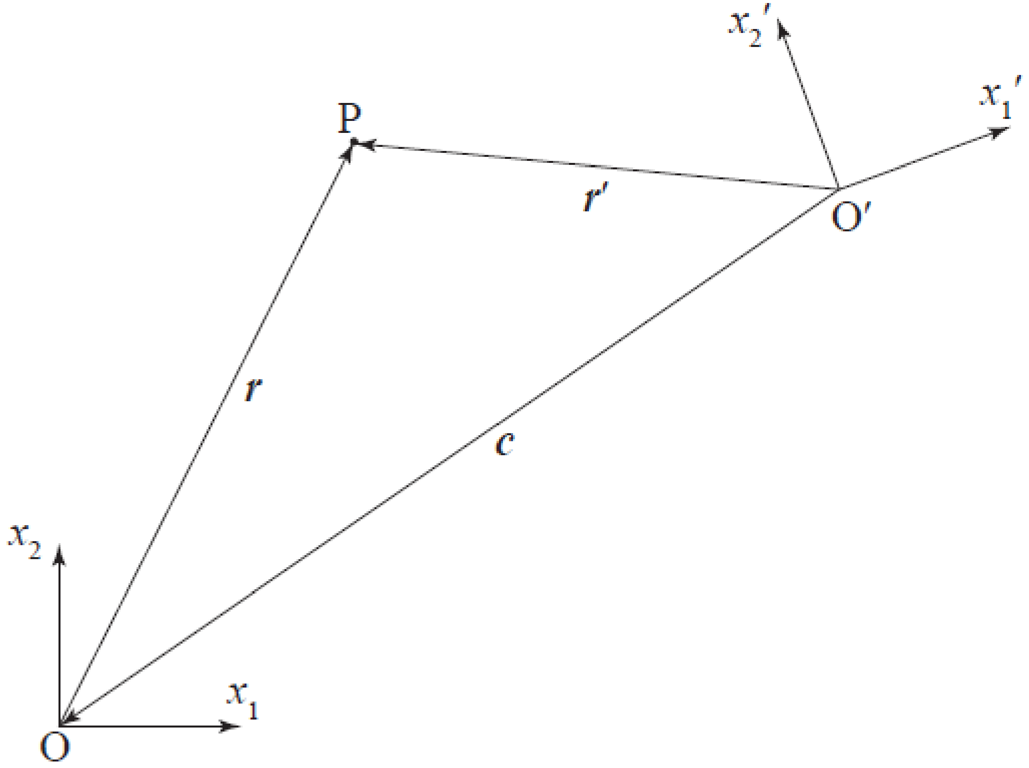

Figure 11.5 Two-dimensional representation of a non-inertial coordinate system with origin O’ relative to an inertial coordinate system with origin O. Point P is an arbitrary point in space.

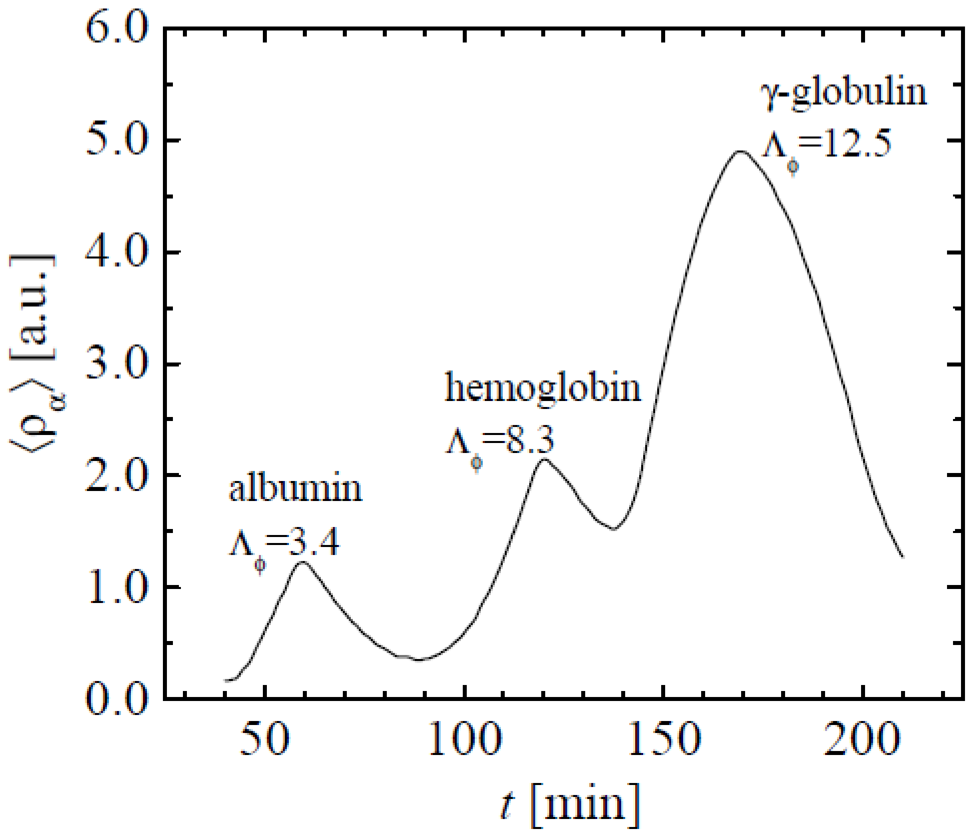

Figure 11.6 Exiting average concentrations versus time for the separation of different blood proteins (species α) in an electric F3 experiment carried out at 25˚C, pH 4:5, and electric potential gradient of 2:95 V/cm. The parameter Λ_ϕ (see Exercise 11.9) is proportional to the molecular weight of the protein. [Adapted from Krishnamurthy & Subramanian, *Sep. Sci.* 12 (1977) 347.]

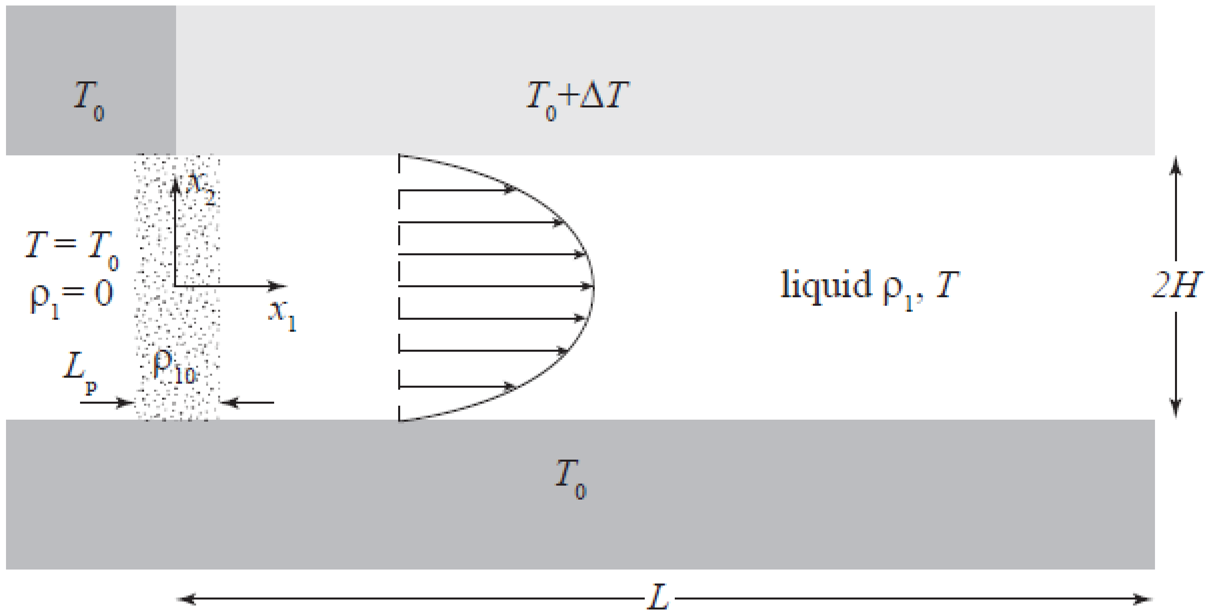

Figure 11.7 Schematic of thermal field-flow fractionation (F_3) channel. For $t < 0$, the liquid is pure solvent ($\rho_1 = 0$) and has uniform temperature T_0. At $t = 0$, a liquid plug having concentration 10 and length L_p is injected at the channel entrance ($x1 = 0$), and for $t \geq 0$ a temperature difference ΔT is maintained between the channel walls.

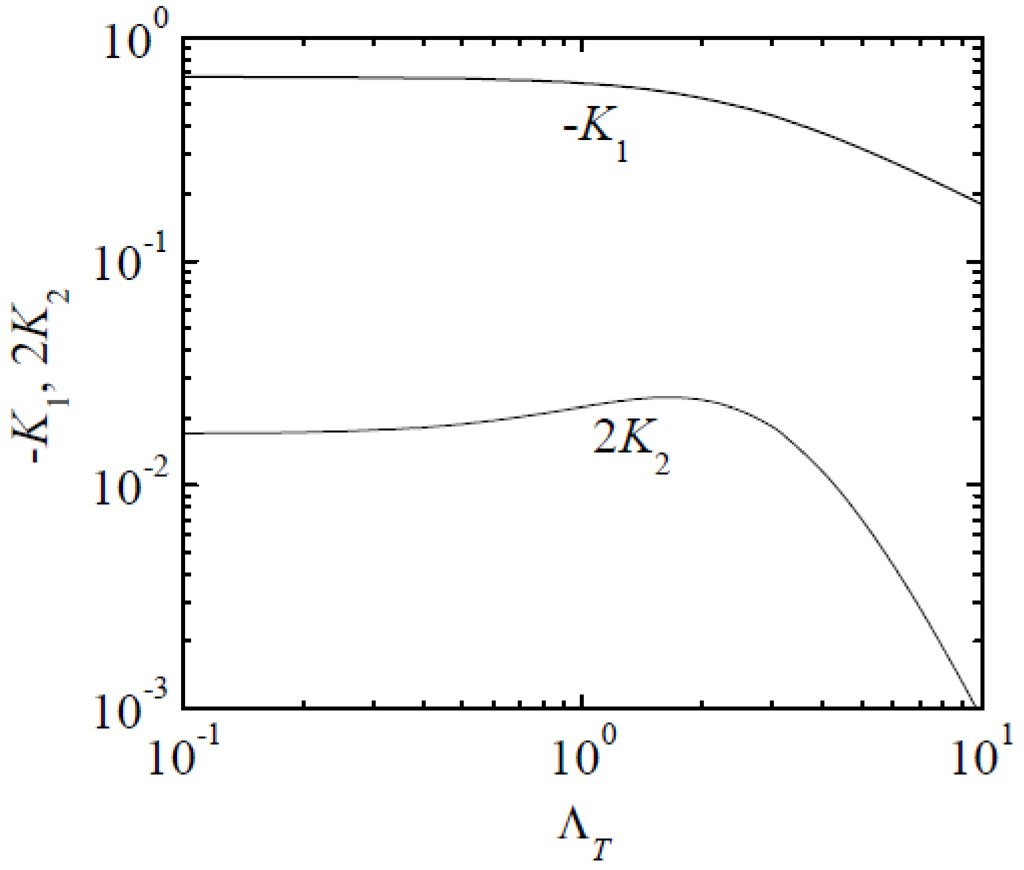

Figure 11.8 Dependence of the coefficients $-K_1$ and K_2 with $N_{\mathrm{Pe}} \gg 1$ on $\Lambda_T = D_T \Delta T/(2D_{12})$ given by (11.47) and (11.48) from dispersion theory solution.

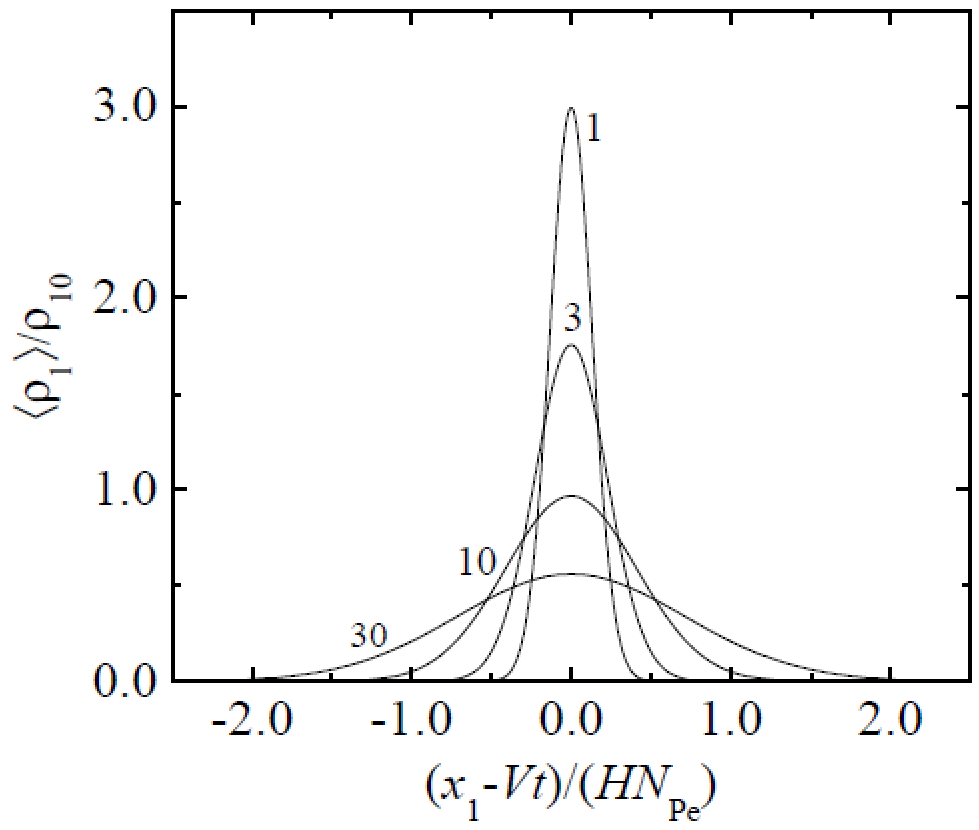

Figure 11.9 Time evolution of the radial-average solute concentration eld for laminar ow in a channel without temperature gradient Λ_T = 0 from (11.46){(11.48) with $N_{\mathrm{Pe}} \gg$ 1 in a coordinate system that moves with the average velocity of the fluid for different times tD_{12}/H^2 = 1, 3, 10, 30.

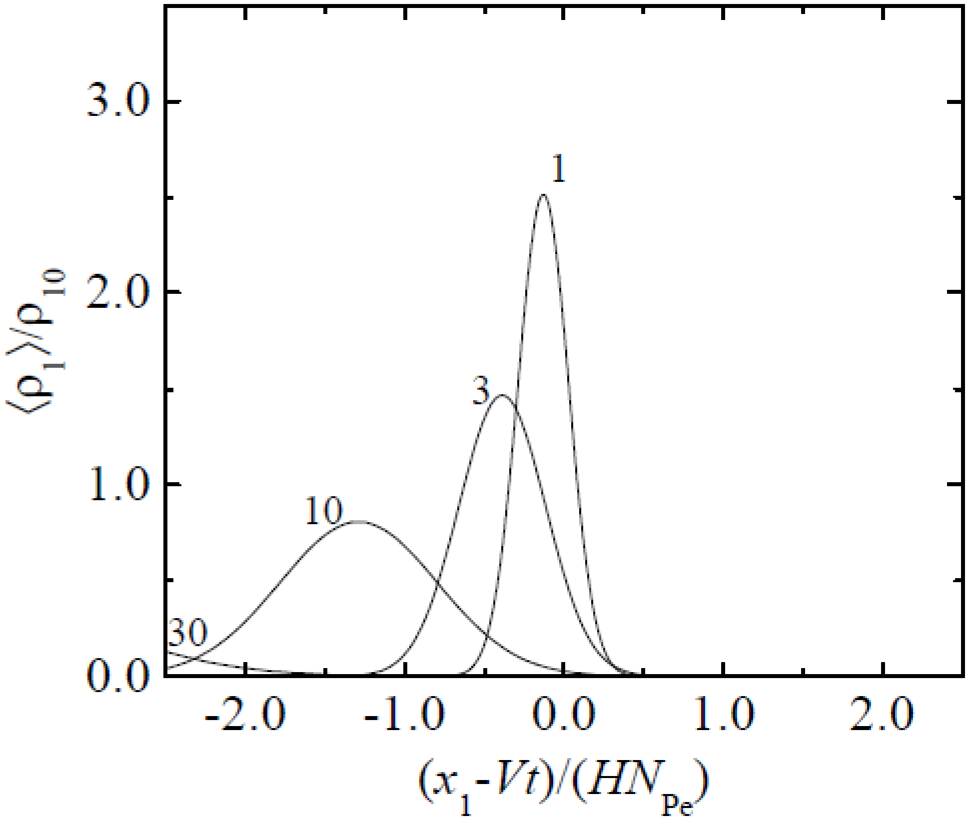

Figure 11.10 Time evolution of the radial-average solute concentration field for laminar flow in a channel with temperature gradient Λ_T = 2 from (11.46)-(11.48) with $N_{\mathrm{Pe}} \gg 1$ in a coordinate system that moves with the average velocity of the fluid for different times tD_{12}/H^2 = 1, 3, 10, 30.

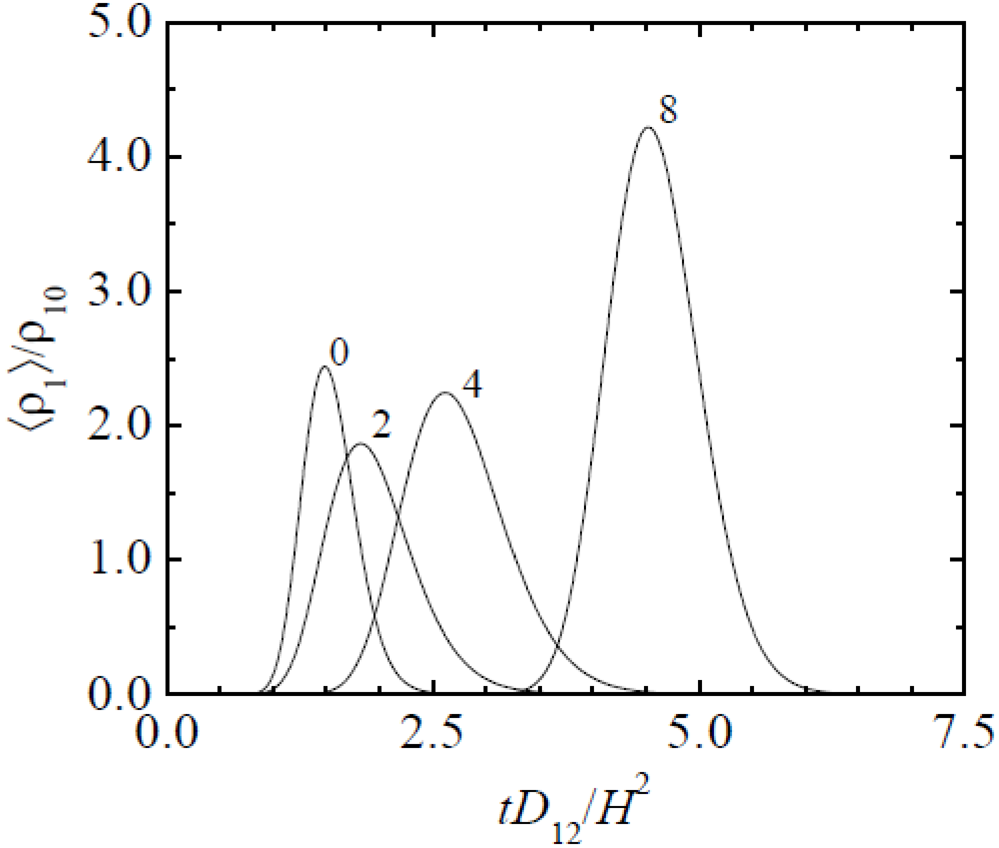

Figure 11.11 Elution curves at channel location $x_1/(HN_{\mathrm{Pe}})$ = 1 in thermal F3 method from (11.46)-(11.48) with $N_{\mathrm{Pe}} \gg 1$ for Λ_T = 0, 2, 4, 8.

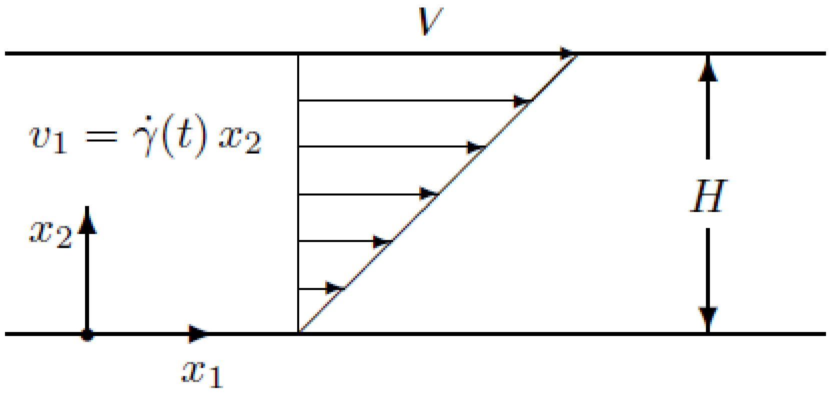

Figure 12.1 Time dependent shear flow between parallel plates with shear rate $\dot{\gamma}(t)$.

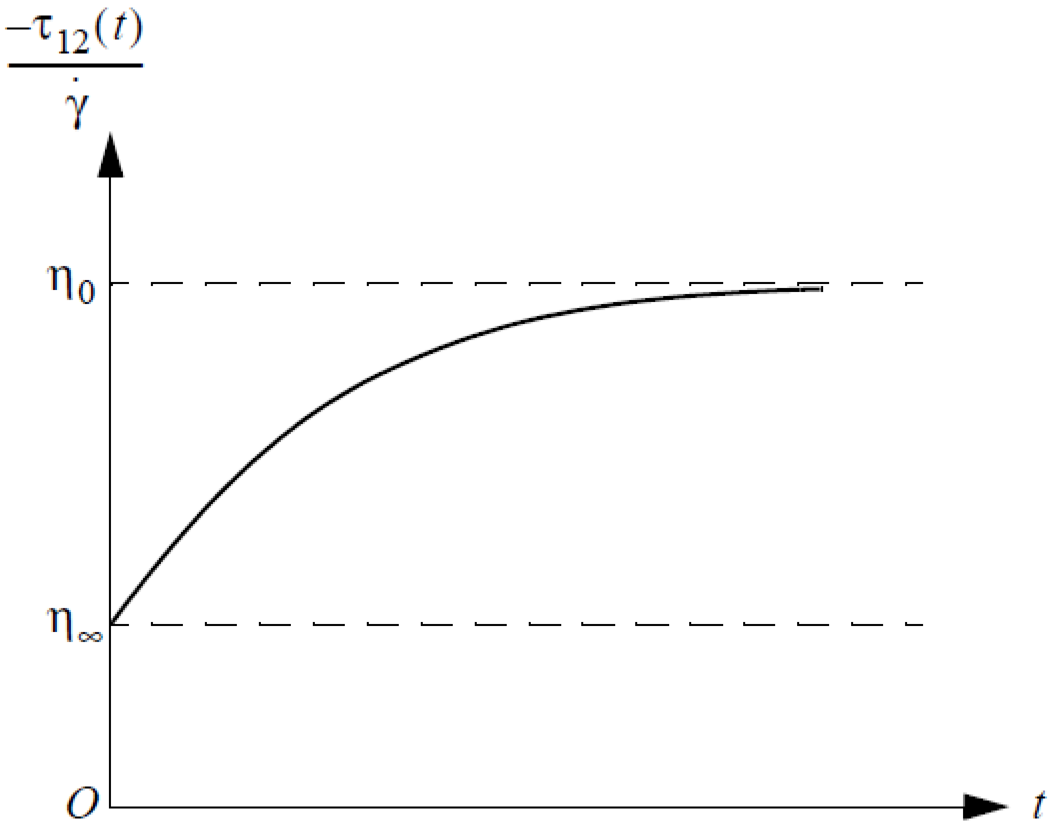

Figure 12.2 Stress growth in start-up of steady shear flow.

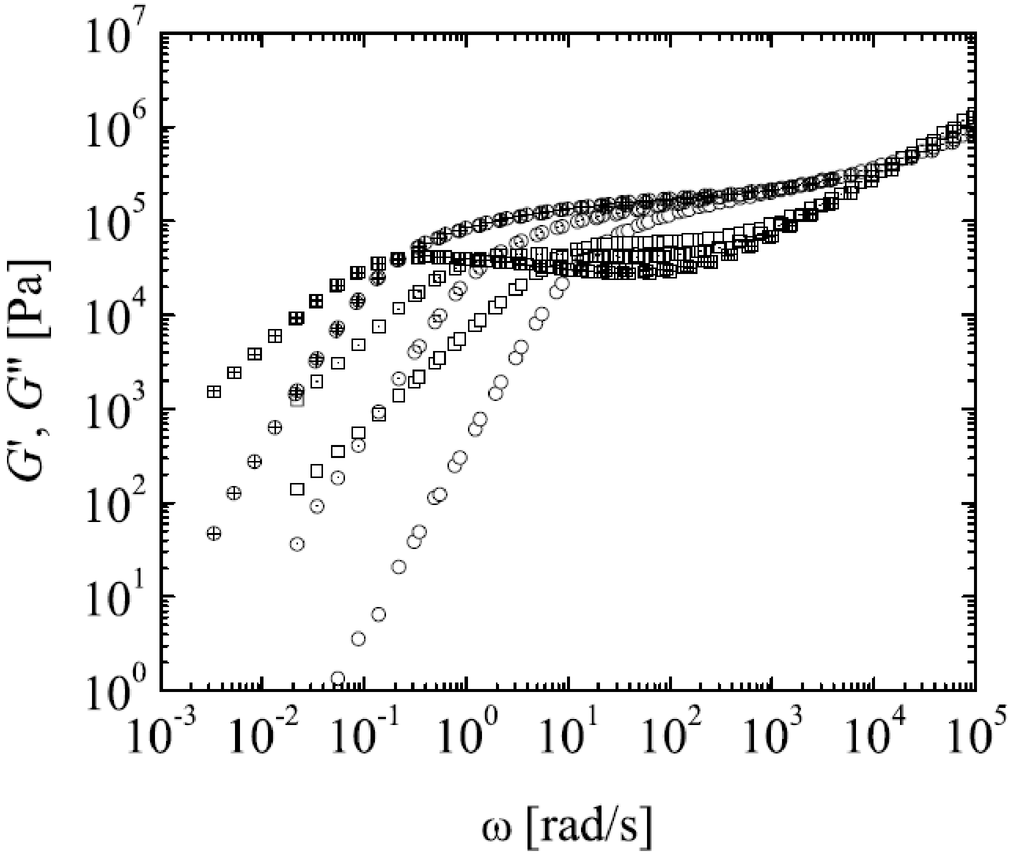

Figure 12.3 Shear storage *G*' (squares) and loss *G*" (circles) moduli versus frequency for three polystyrene melts at 180˚C: $\tilde{M}_w$ = 100 kDa (open); $\tilde{M}_w$ = 200 kDa (dots); $\tilde{M}_w$ = 400 kDa (crosses), from experiments performed by Teresita Kashyap at IIT, Chicago.

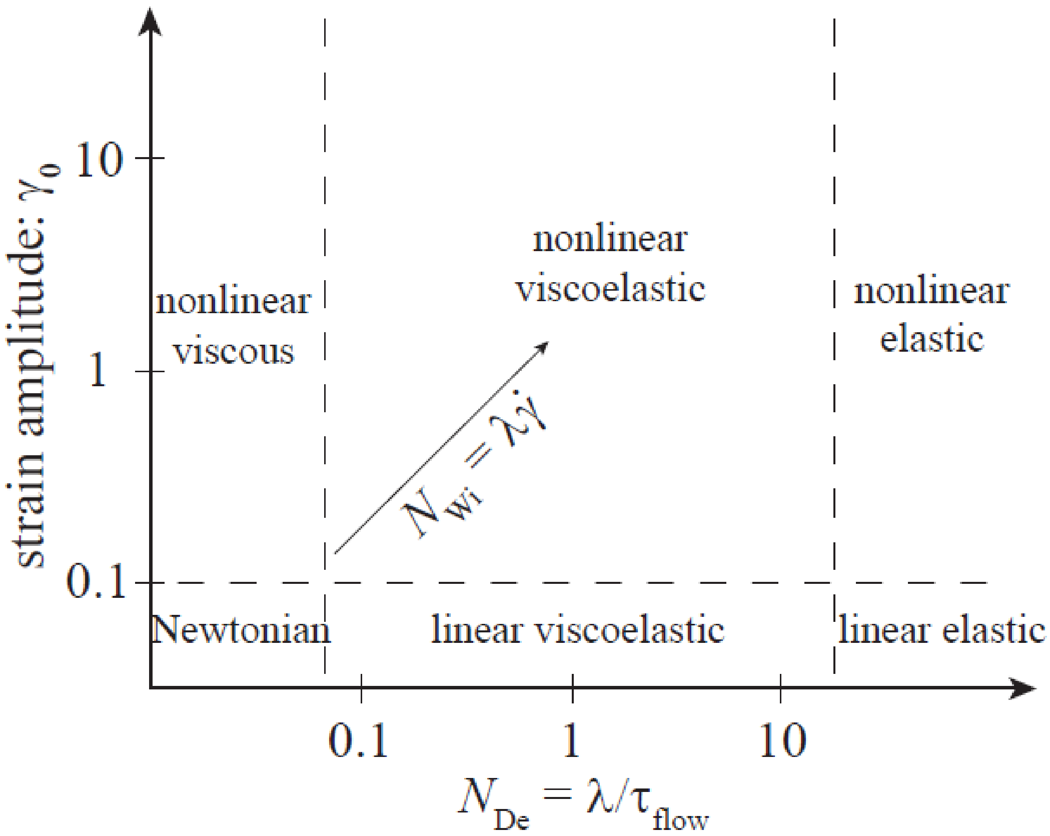

Figure 12.4 Pipkin diagram showing dependence of material response on Deborah N_{De} and Weissenberg N_{Wi} numbers.

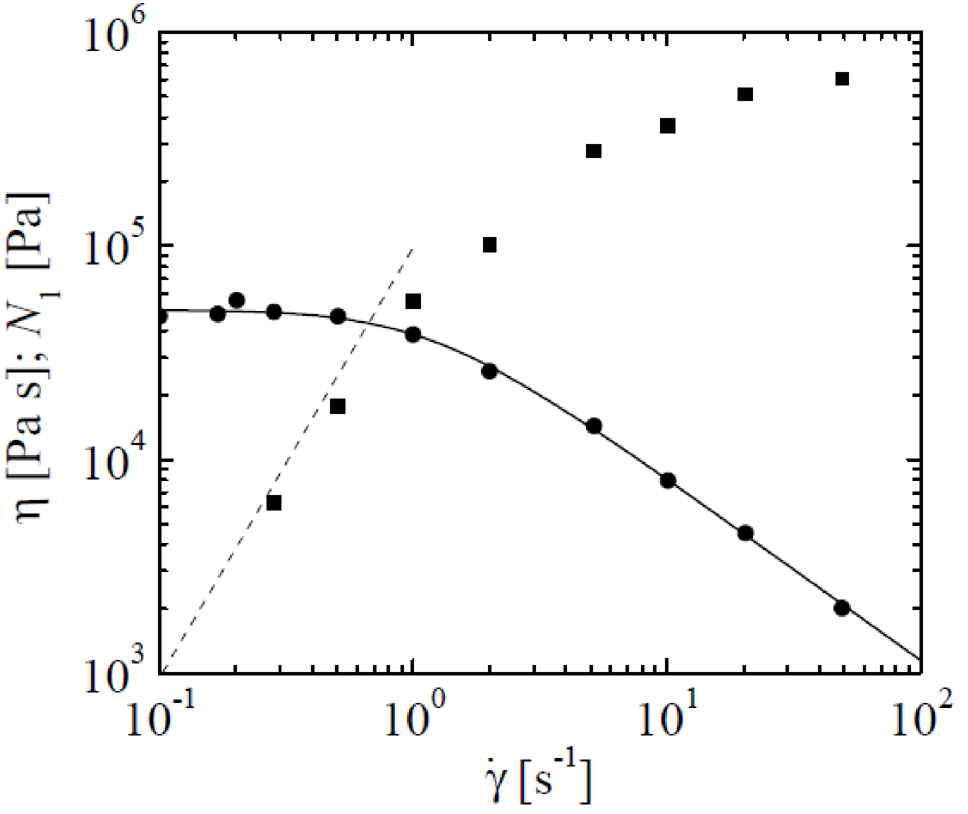

Figure 12.5 Steady state viscosity and first normal-stress difference N_1 versus shear rate for a polystyrene melt at 180˚C ($\tilde{M}_w$ =200 kDa), from Schweizer et al., Rheol. Acta 47 (2008) 943. The solid curve is the t of the expression given in (12.39).

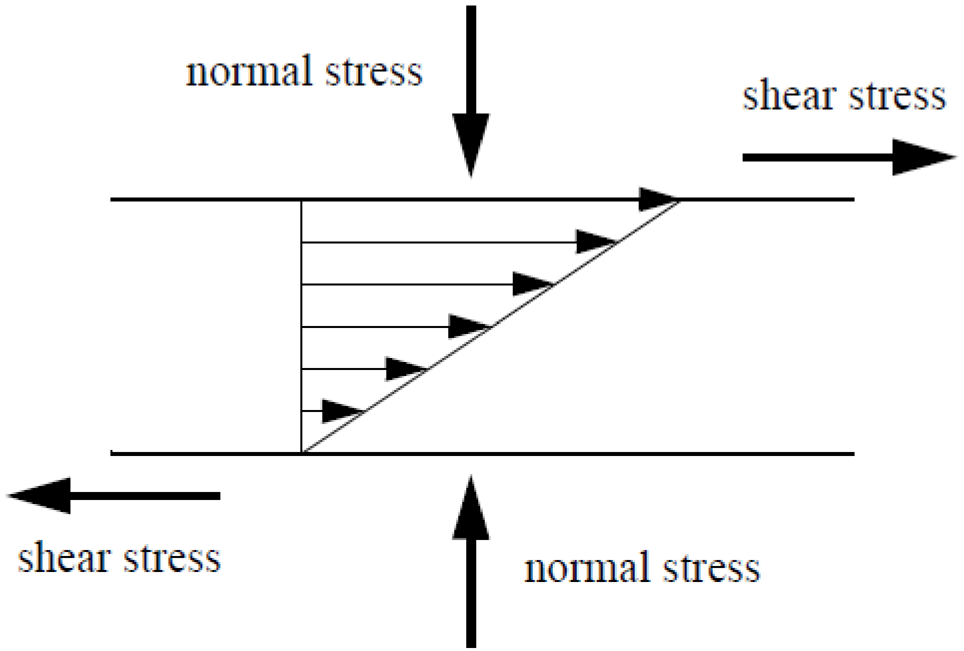

Figure 12.6 Occurrence of normal-stress differences in shear flow of viscoelastic liquids.

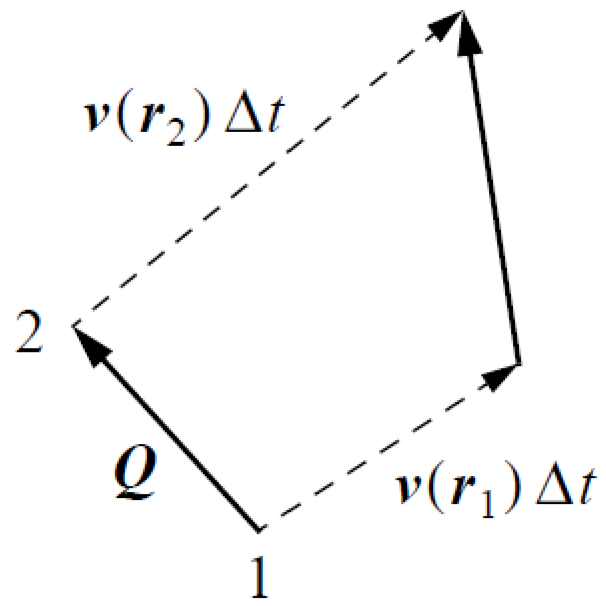

Figure 12.7 Translation and deformation of a vector by convection.

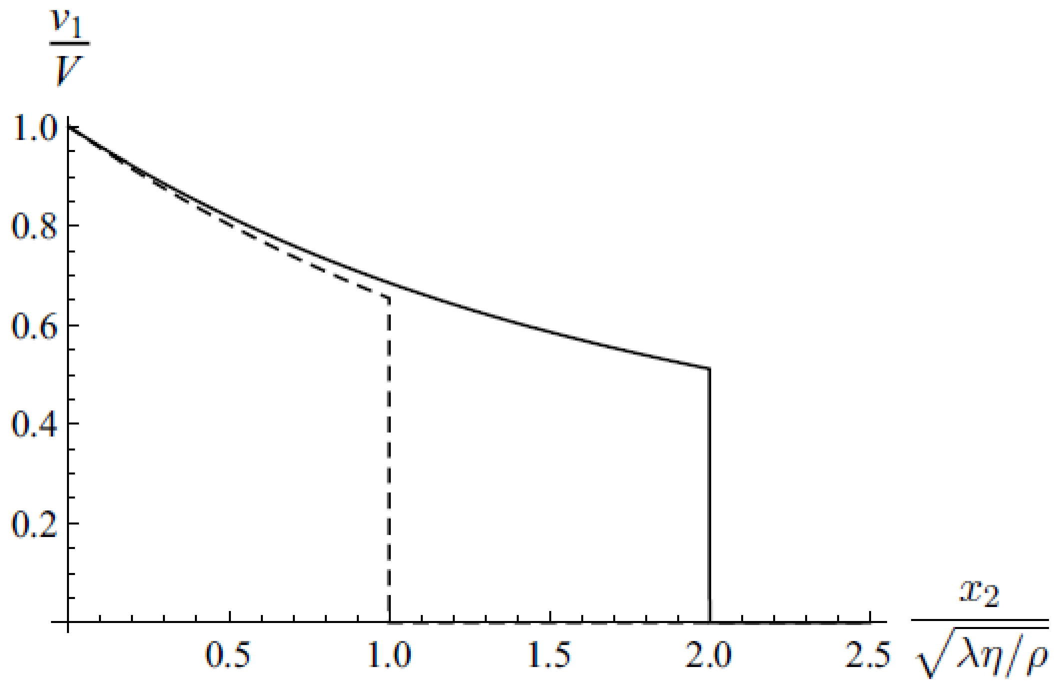

Figure 12.8 The velocity profile (12.68) for $t\,\lambda = 1$ (dashed line) and $t\,\lambda = 2$ (continuous line).

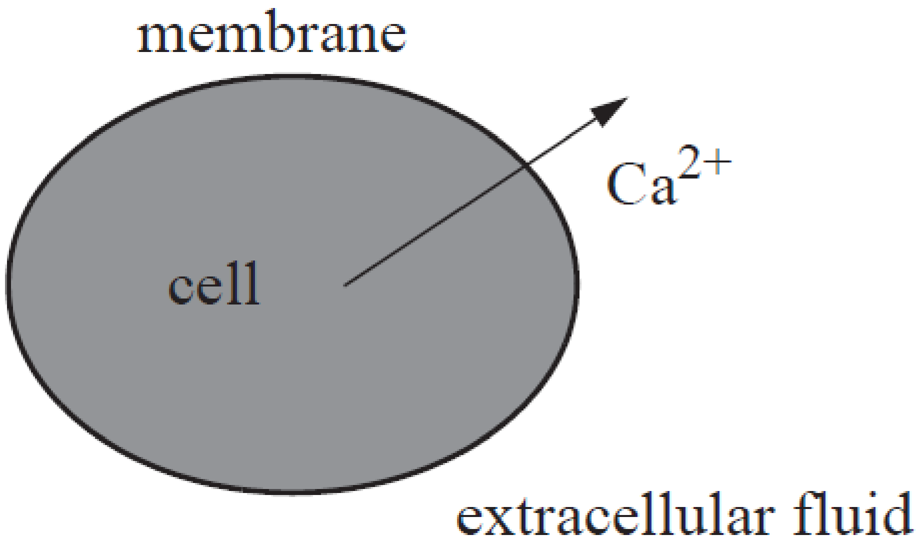

Figure 13.1 Calcium transport across a cell membrane.

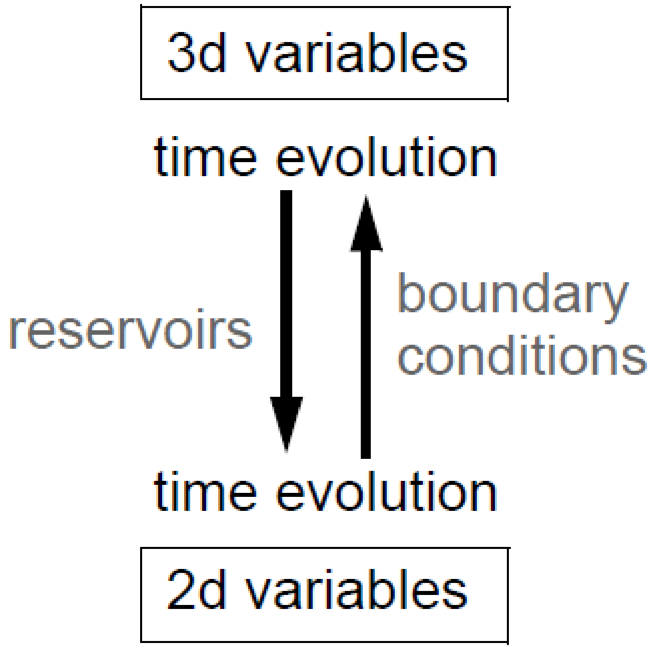

Figure 13.2 Two-way coupling between bulk phases and interfaces.

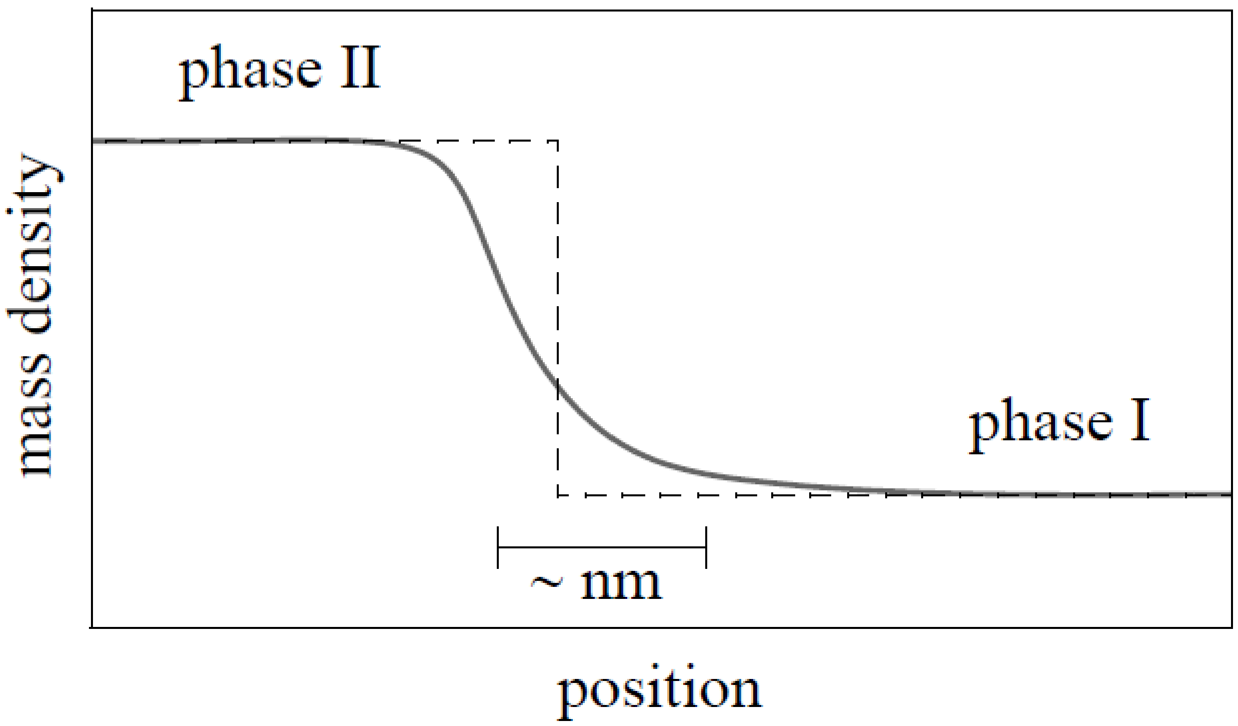

Figure 13.3 True continuous density profile (continuous line) and an idealized profile for two bulk phases touching at a dividing interface (dashed line).

$$\frac{|\Delta \boldsymbol{n}|}{|\Delta \boldsymbol{r}|} = \frac{|\boldsymbol{n}|}{|\boldsymbol{r}|} = \frac{1}{R}$$

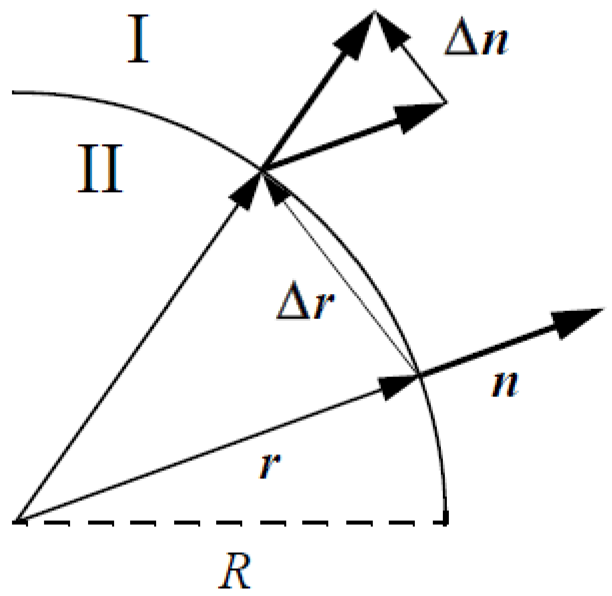

Figure 13.4 Relationship between change of normal vector and radius of curvature.

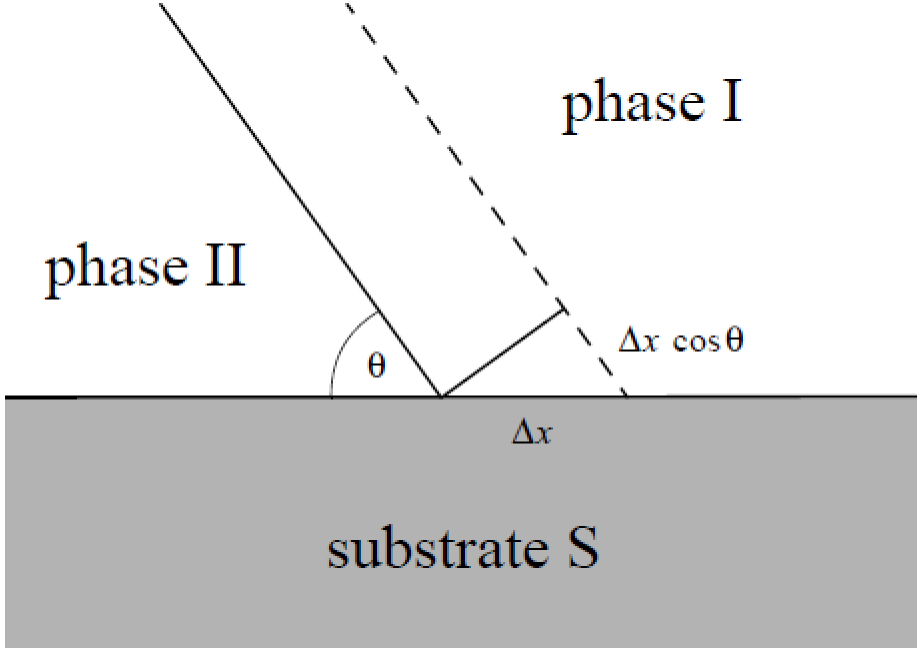

Figure 13.5 Contact angle θ for two fluid phases I and II in equilibrium with a rigid substrate.

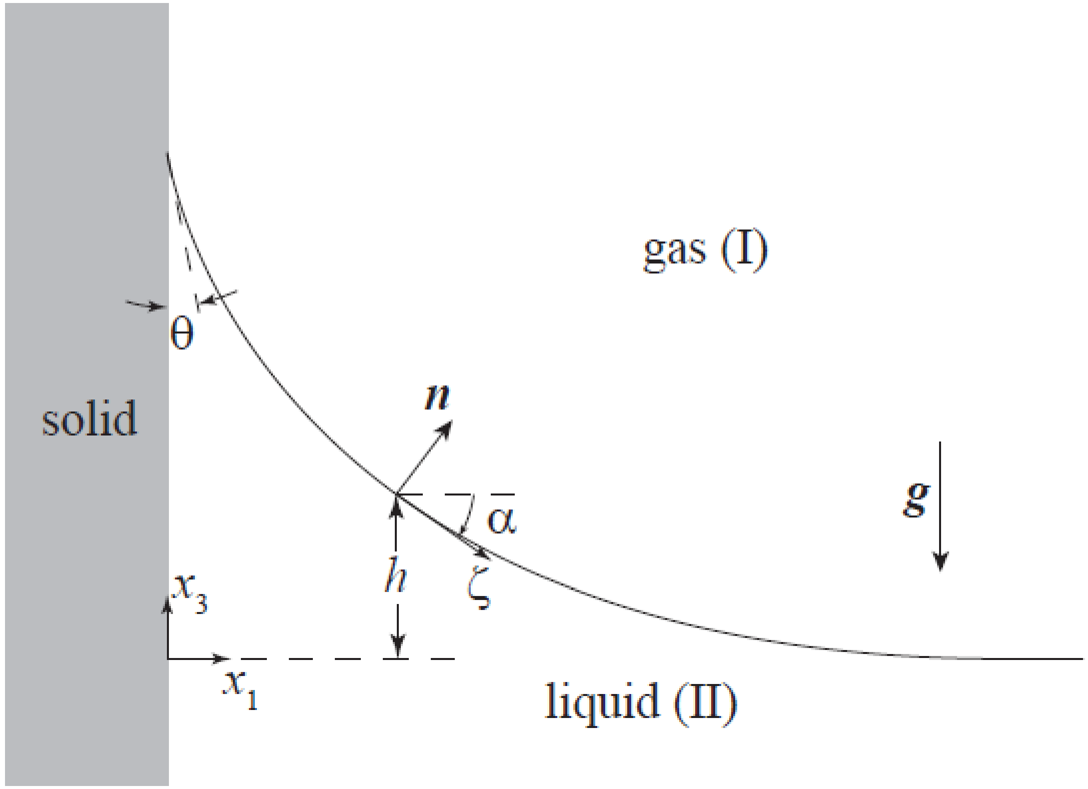

Figure 13.6 Meniscus formed by liquid in contact with a planar solid with local height *h* and contact angle θ .

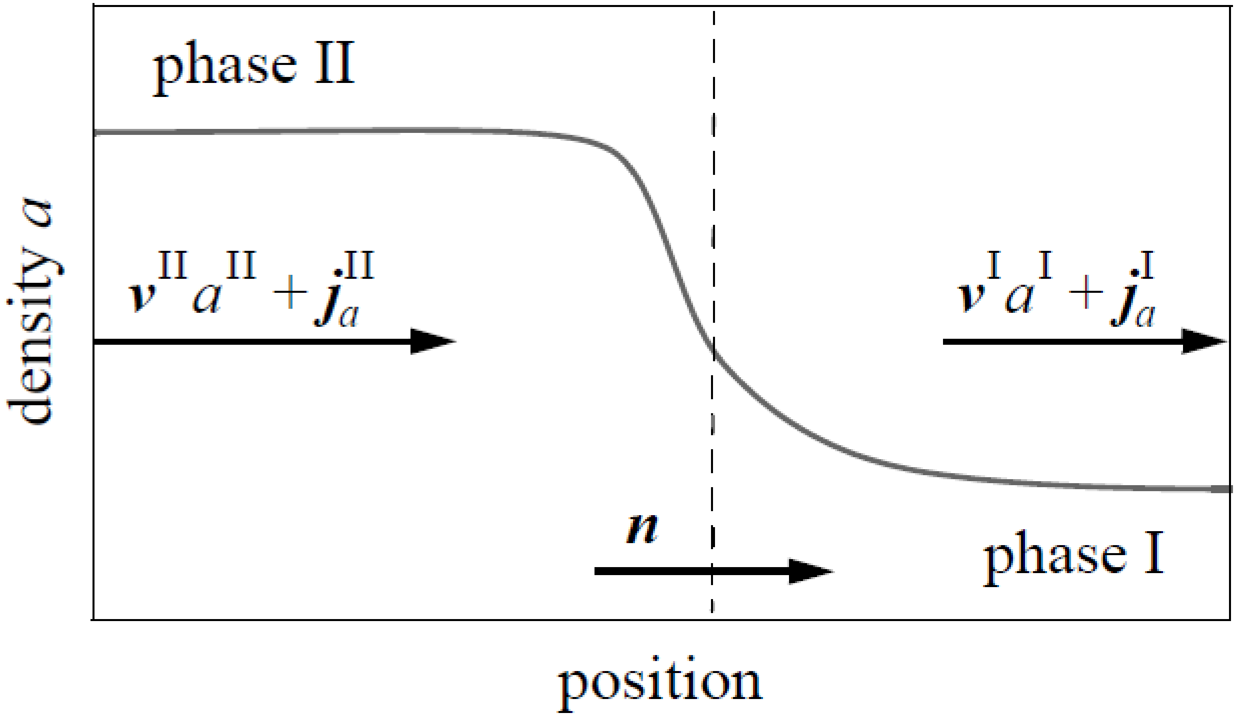

Figure 14.1 Density profile of a conserved quantity. As a consequence of a net accumulation of that quantity in the interfacial region, the dividing interface for a_s = 0 (dashed line) moves to the right.

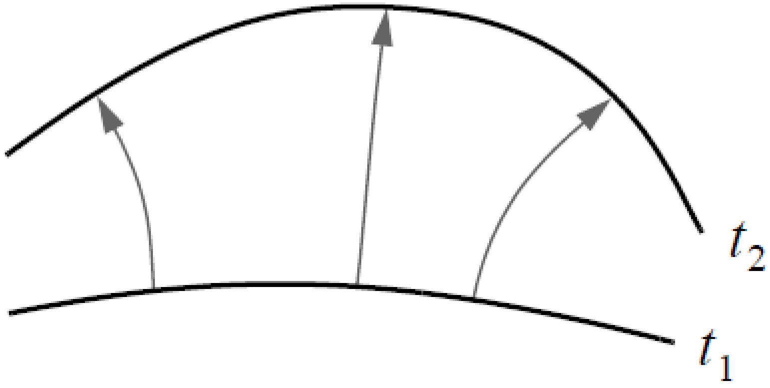

Figure 14.2 Instead of mapping equivalent points of a continuously deforming interface at two times *t*1 and *t*2 (thick lines), we can alternatively look at the trajectories associated with equivalent points (thin arrows) and their time derivatives providing the translational velocity field v^{s}_{tr}.

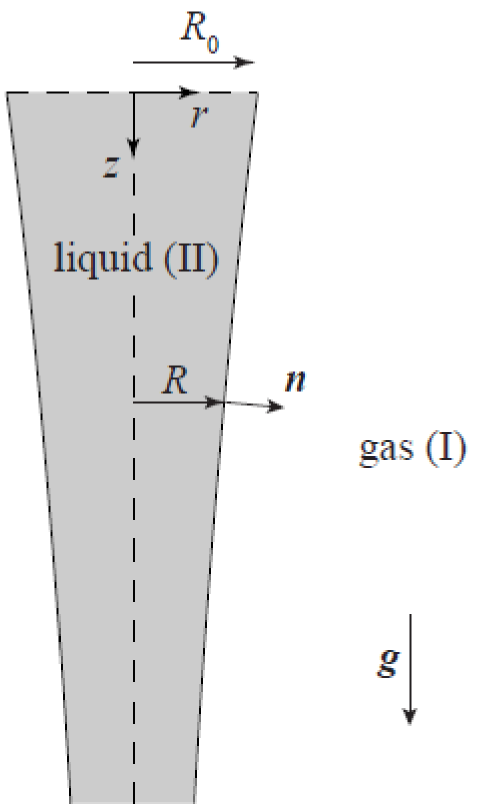

Figure 14.3 Falling liquid (II) jet surrounded by gas (I).

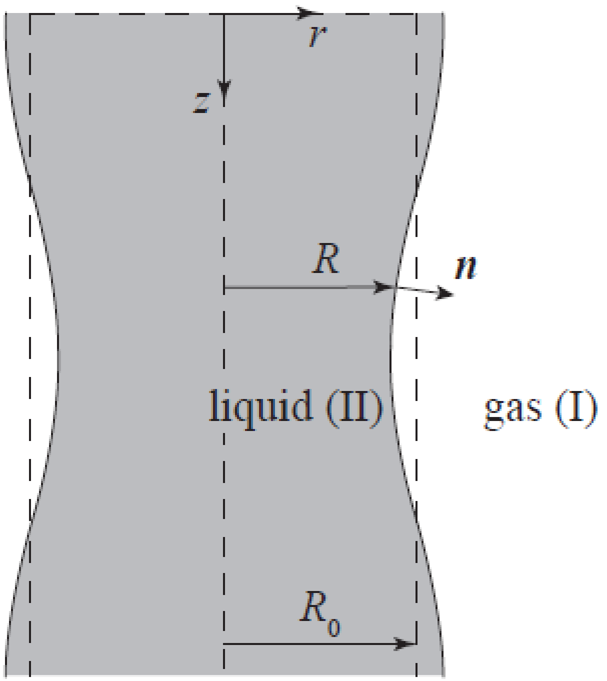

Figure 14.4 Liquid (II) cylinder with unperturbed radius R0 surrounded by gas (I).

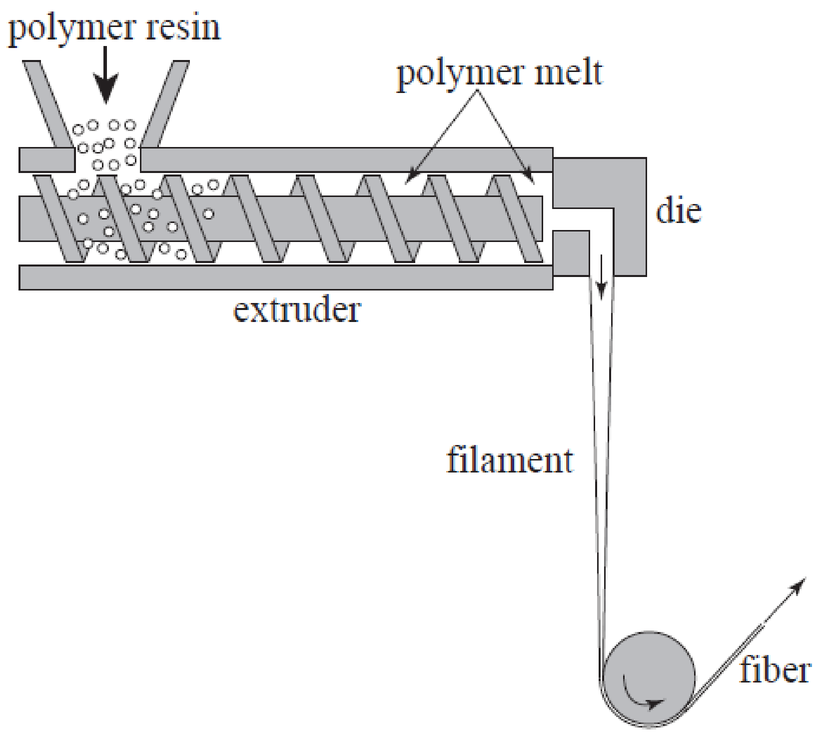

Figure 16.1 Schematic of process for the production of polymer fibers.

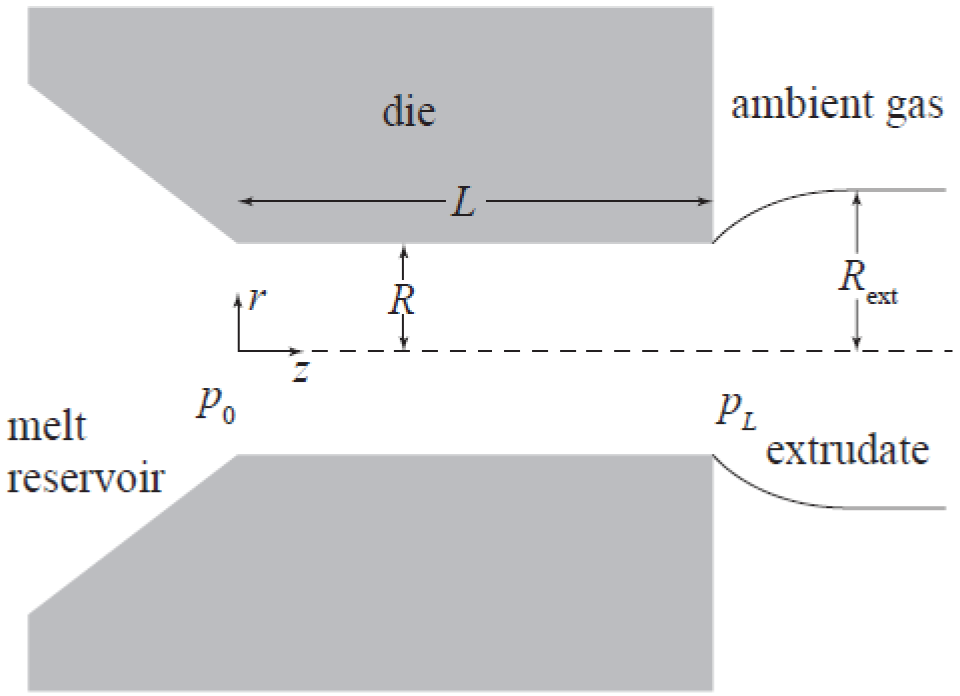

Figure 16.2 Schematic of flow through a circular die.

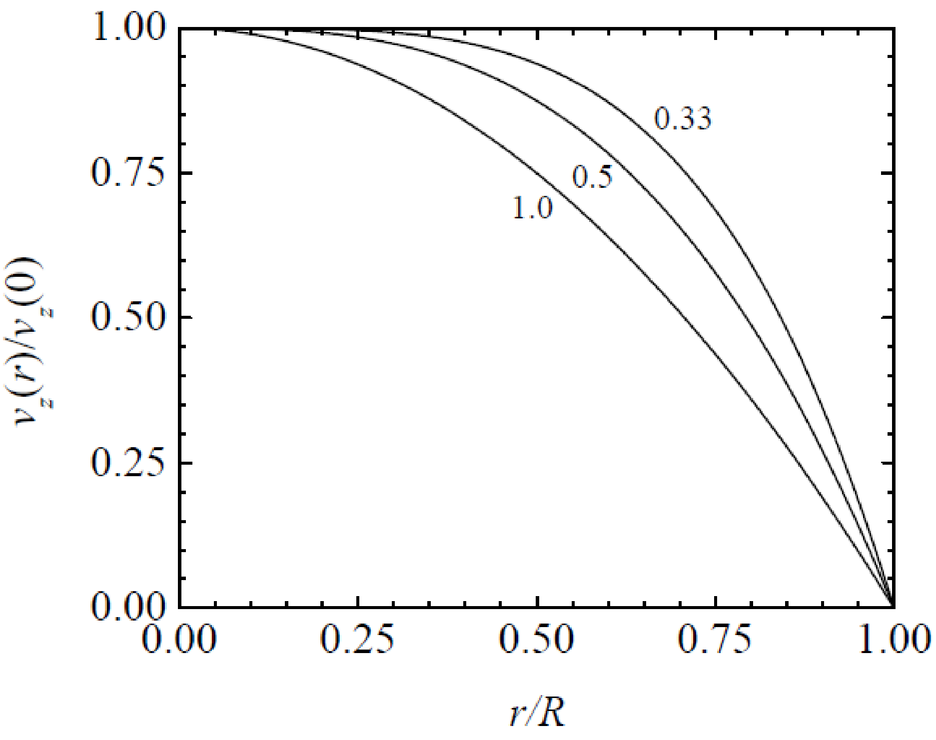

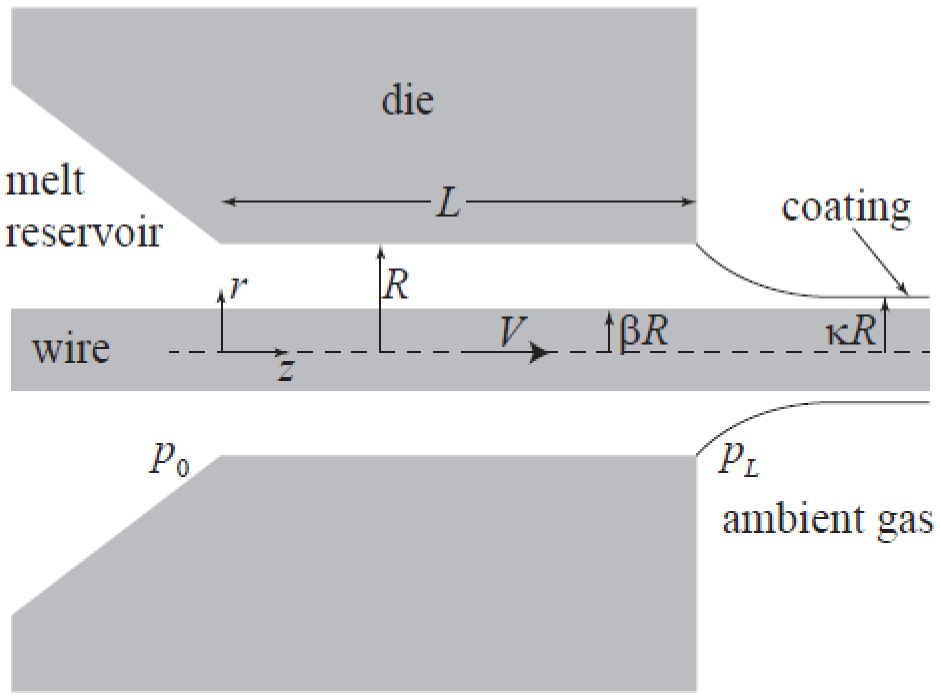

Figure 16.3 Velocity prole for flow through a circular die given by (16.6) for different values of the power law index *n* = 1.0, 0.5, 0.33 bottom to top.

Figure 16.4 Schematic of wire coating flow through a circular die.

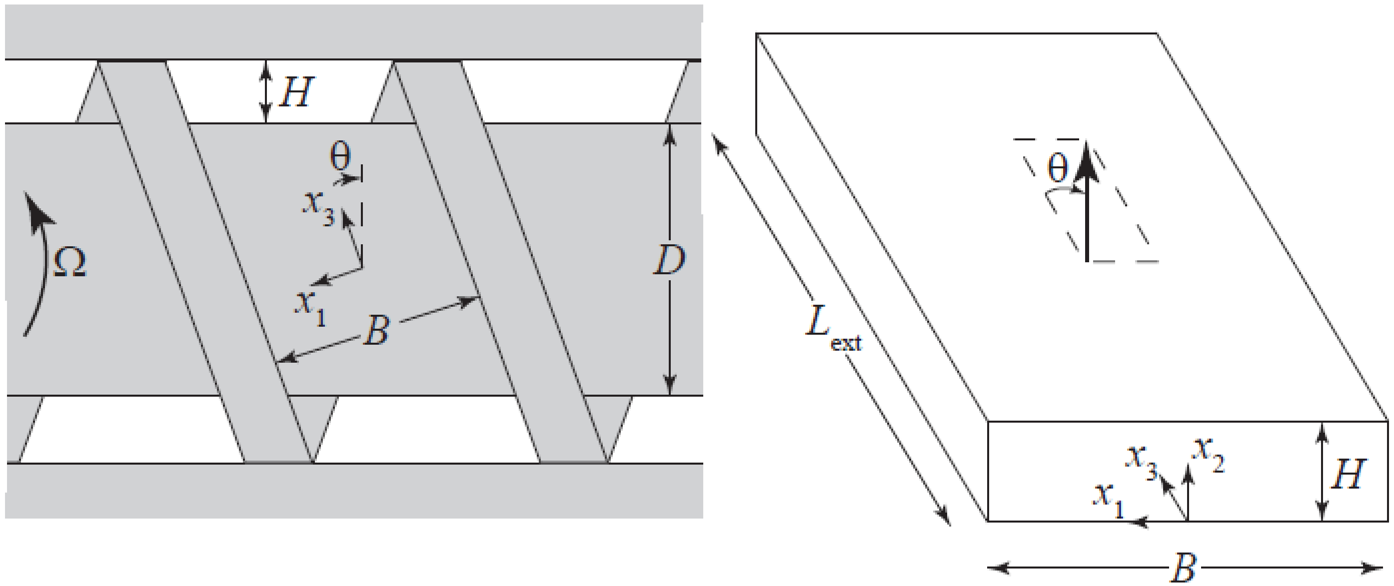

(Above) Figure 16.5 Schematics of extruder with screw rotating with angular Ω locity inside stationary barrel (left) and unwound channel formed between screw and barrel (right).

(Left) Figure 16.6 Representative streamline showing recirculating nature of transverse flow within extruder channel. Solid lines indicate flow described by (16.11).

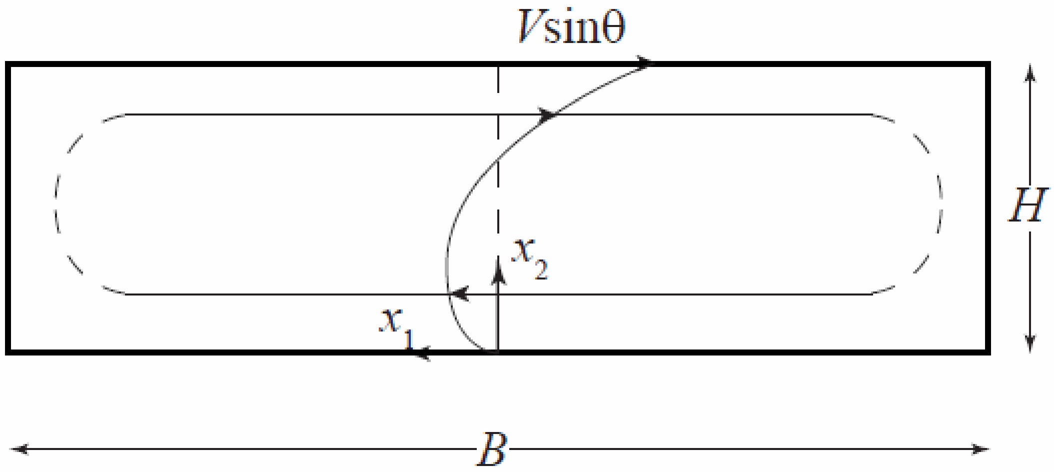

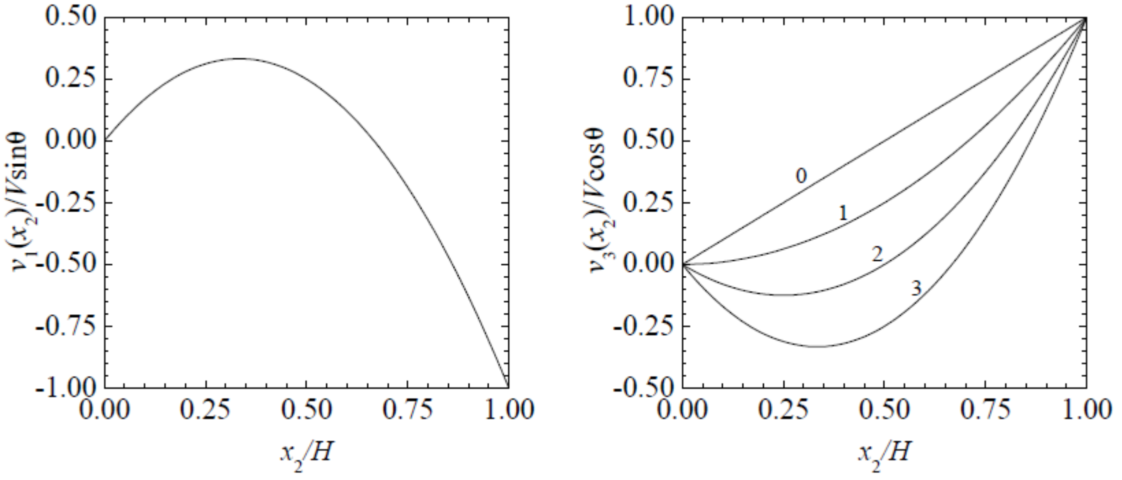

Figure 16.7 Velocity distributions is single-screw extrusion. Left plot shows transverse velocity v_1 given by (16.11), right plot shows velocity along channel v_3 given by (16.12) for several values of the quantity $H^2\Delta p_{\mathrm{ext}}/(2\eta L_{\mathrm{ext}}V\cos\theta)$.

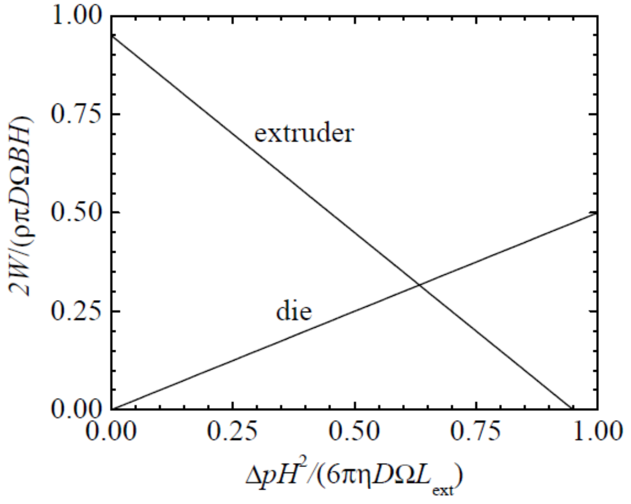

Figure 16.8 Mass flow rate versus pressure difference for single-screw extrusion (θ=10) of a Newtonian fluid. Line marked `die' is from (8.5) with $3\pi R^4 L_{\mathrm{ext}}/(2BH^3L)$= 0:5, and line marked `extruder' is from (16.13). The intersection of the two lines gives the operating point of the extruder.

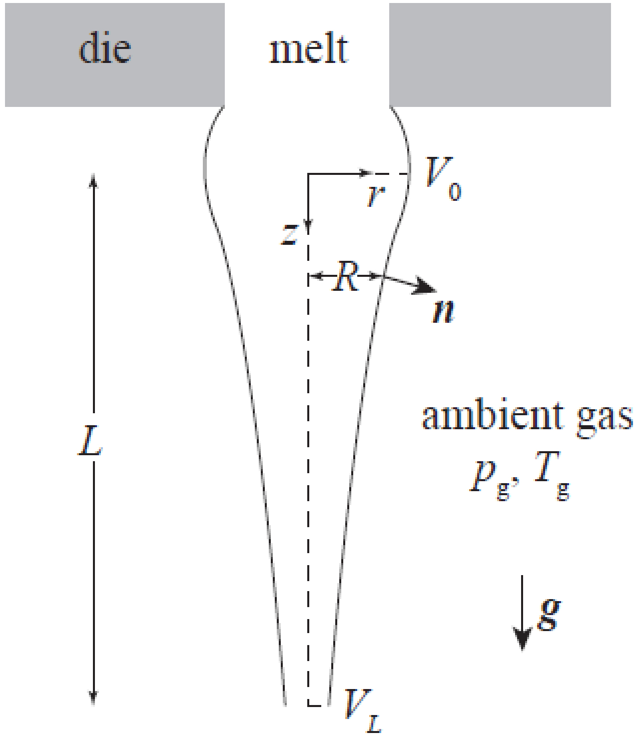

Figure 16.9 Schematic of fiber spinning process showing lament of length *L* and local radius *R*. Note that in practice *R* << *L.*

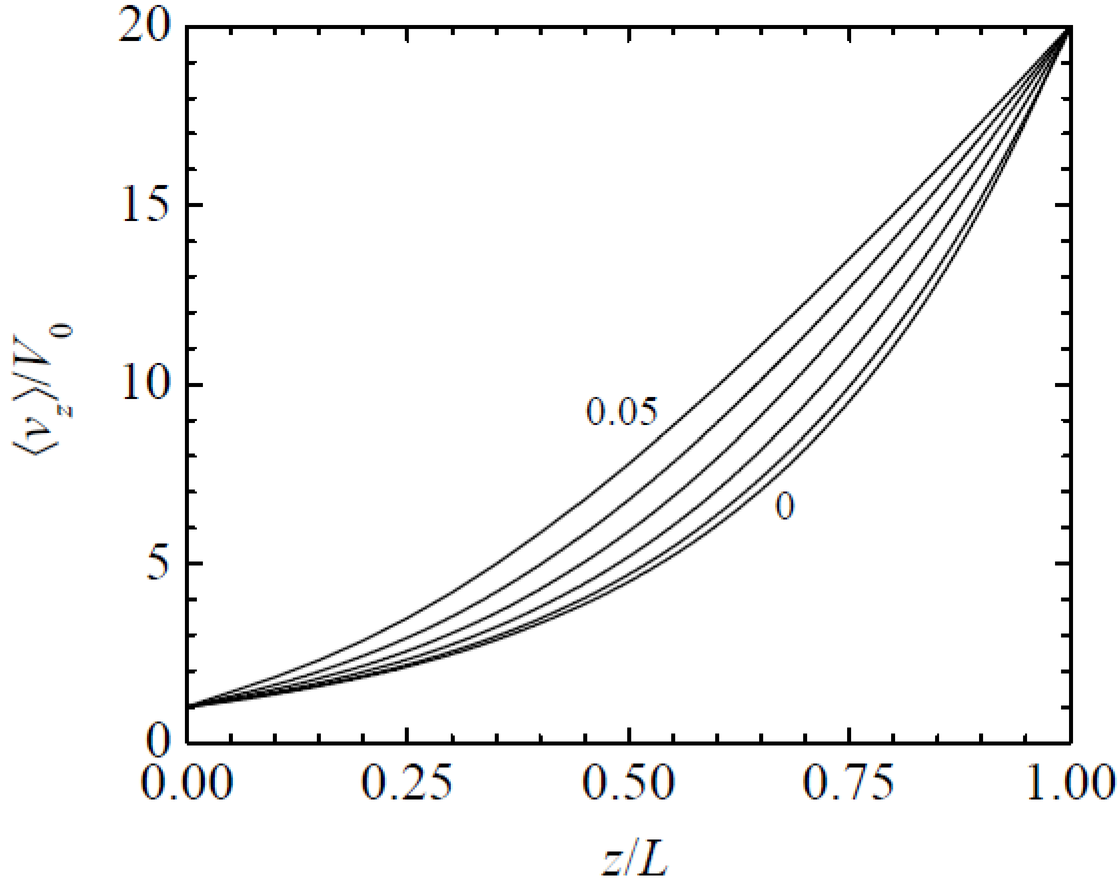

Figure 16.10 Axial velocity along lament for fiber spinning of an upperconvected Maxwell fluid for $N_{\mathrm{De}} = \lambda V_0/L$ = 0, 0.01, 0.02, 0.03, 0.04, 0.05 (bottom to top) obtained by solution of (16.36) for D_R = 20. The Newtonian case (N_{De} = 0) given by (16.39).

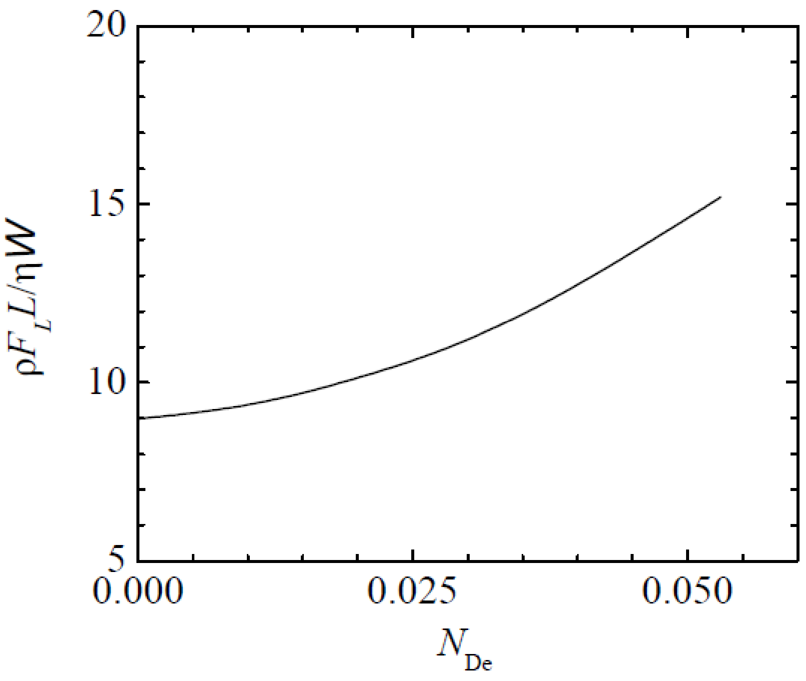

Figure 16.11 Dependence of F_L on NDe for the fiber spinning of an upperconvected Maxwell fluid for D_R = 20. Note that the maximum possible Deborah number is given by N_{De} = (D_R -1) -1

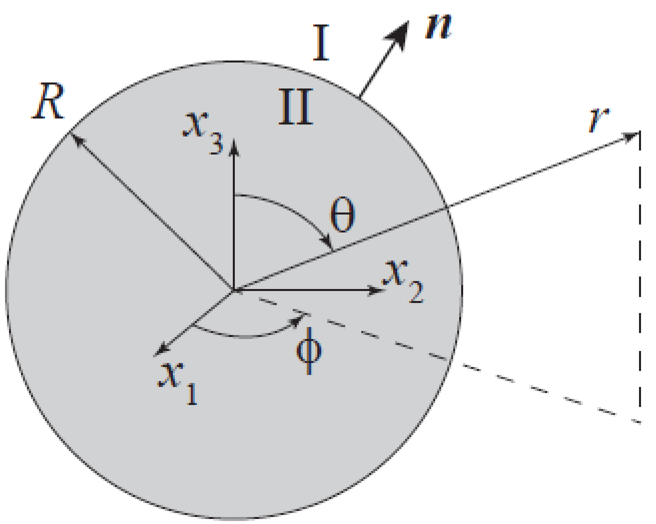

Figure 17.1 Sphere of radius R with its center at the origin of rectangular and spherical coordinate systems surrounded by an infinite medium.

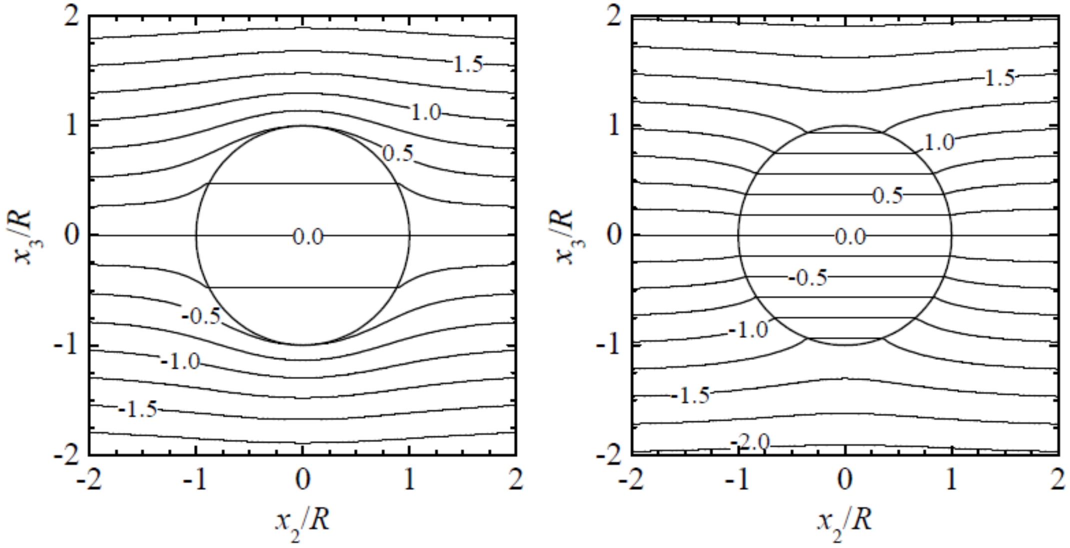

Figure 17.2 Normalized temperature $(T-T_0)/(R|\nabla T|_\infty)$ isotherms in the *x2-x3* plane around a sphere imbedded in an infinite medium predicted by (17.10) and (17.11) with N_{Ka} = 0 and β = 4 (left) and β 1=4 (right).

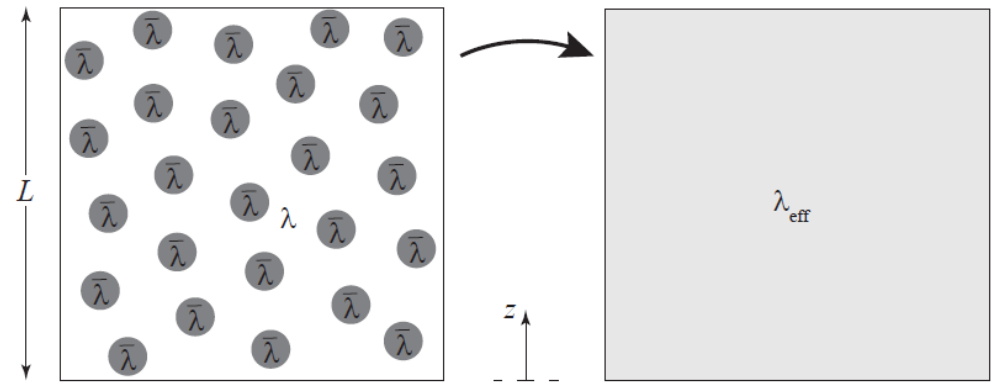

Figure 17.3 Schematic of heterogeneous system composed of multiple spheres with thermal conductivity $\bar{\lambda}$ imbedded in a medium with thermal conductivity λ, and its representation as an effectively continuous medium with effective thermal conductivity λ_{eff}.

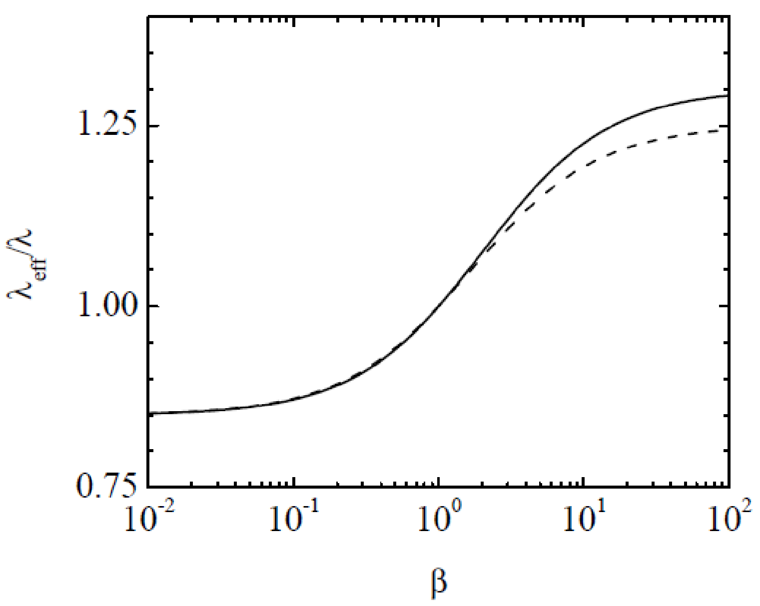

Figure 17.4 Dependence of normalized effective thermal conductivity as a function of thermal conductivity ratio predicted by (17.16) for = 0.1 with N_{Ka} = 0 (solid line) and N_{Ka} = 0.1 (dashed line).

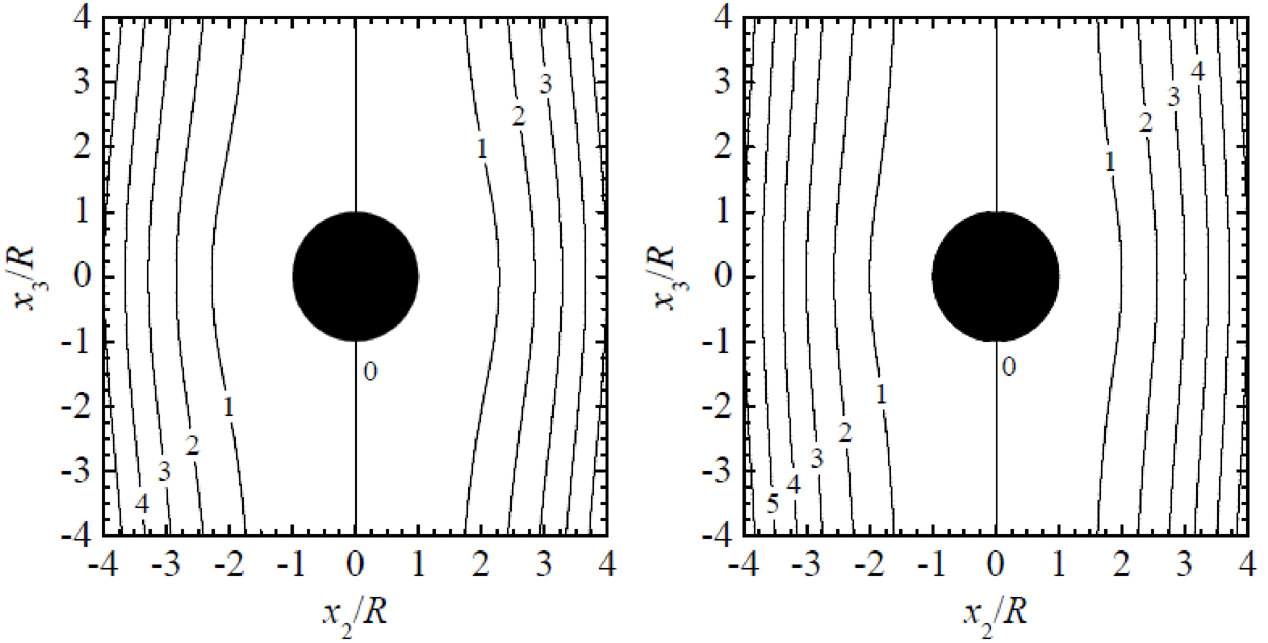

Figure 17.5 Normalized stream function $\psi/(VR^2)$ in the *x2-x3* plane for creeping flow around a sphere predicted by (17.29) with Λ_ξ = 0 (left) and $\Lambda_\xi \to \infty$ (right).

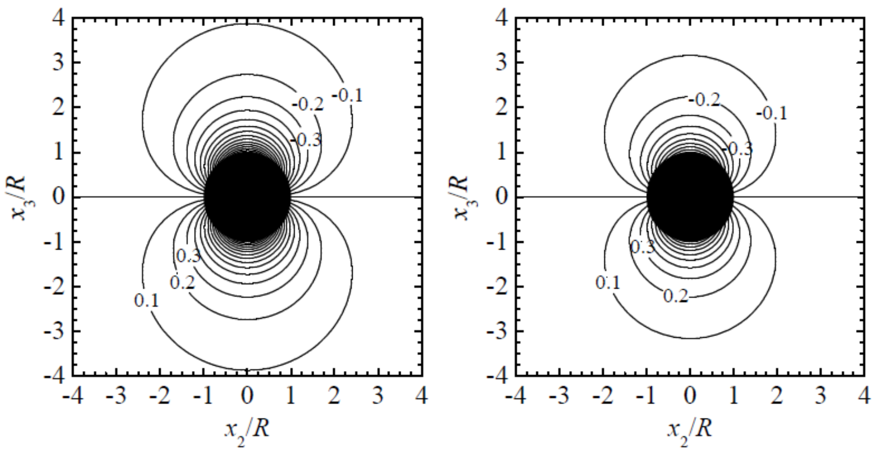

Figure 17.6 Normalized pressure contours $p^{\mathrm{L}}/(\eta V/R)$ in the *x2-x3* plane for creeping ow around a sphere from (17.32) with Λ_ξ = 0 (left) and $\Lambda_\xi \to \infty$ (right).

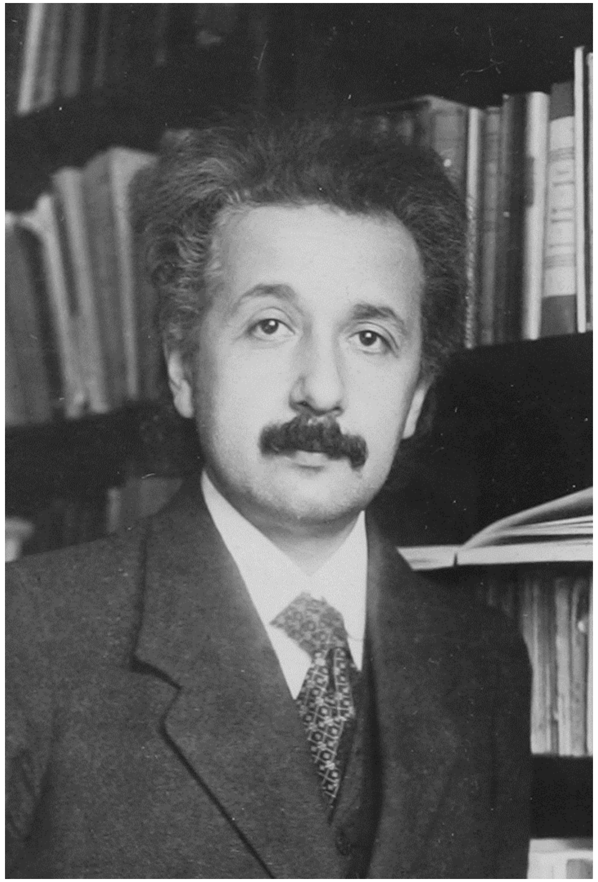

Figure 17.7 Albert Einstein (1879-1955) in 1904.

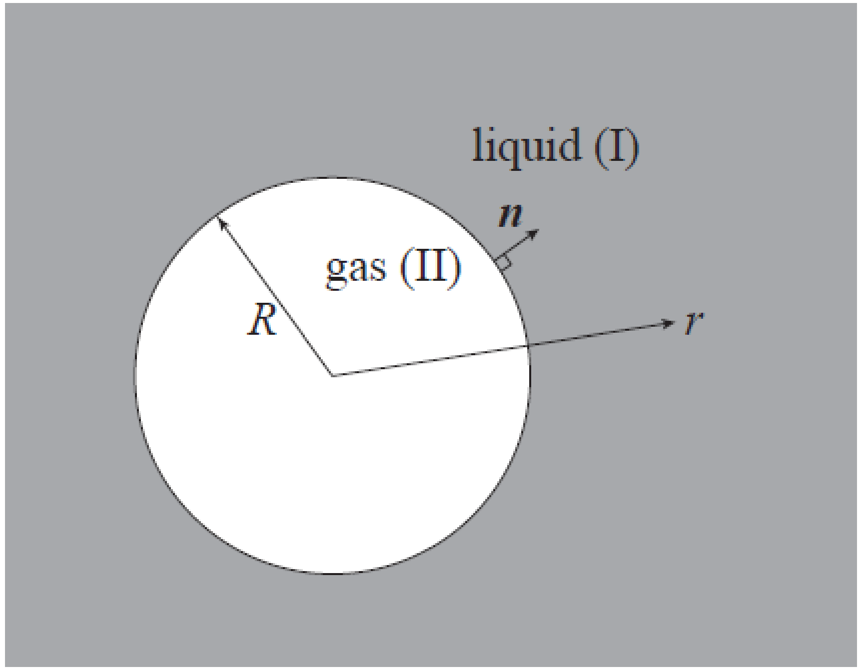

Figure 18.1 Schematic of gas bubble with radius *R* surrounded by infinite liquid.

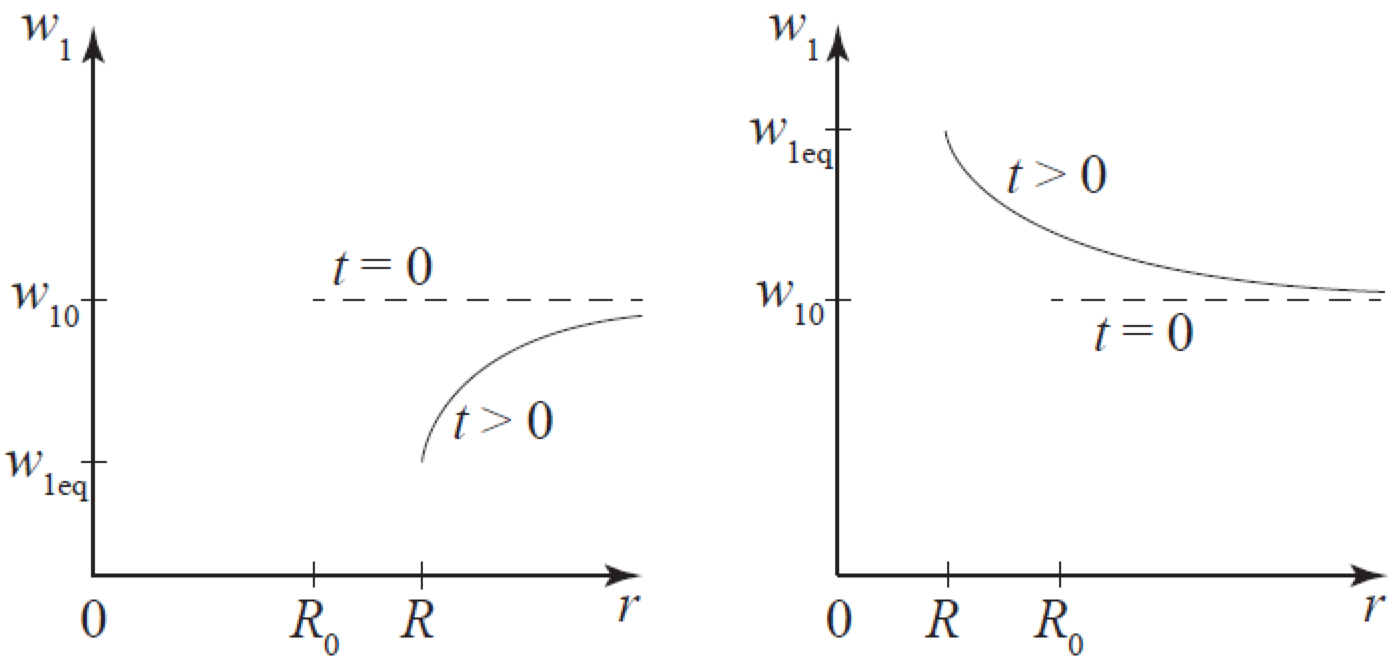

Figure 18.2 Representative concentration field *w*1 in liquid (*r* > *R*) versus radial position r for bubble growth (*R* > *R*0) and collapse (*R* < *R*0).

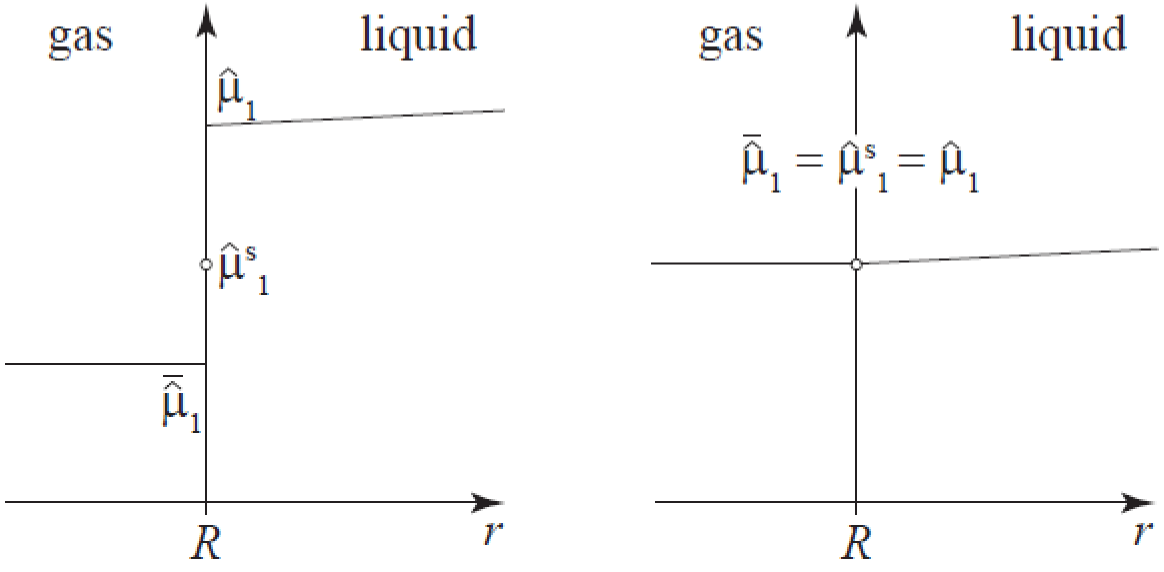

Figure 18.3 Representative solute chemical potentials for the gas phase $\bar{\hat{\mu}}_1$, interface $\hat{\mu}_1^{\mathrm{s}}$ and liquid $\hat{\mu}_1$ near the gas-liquid interface for bubble growth showing nonequilibrium (left) and equilibrium (right) cases.

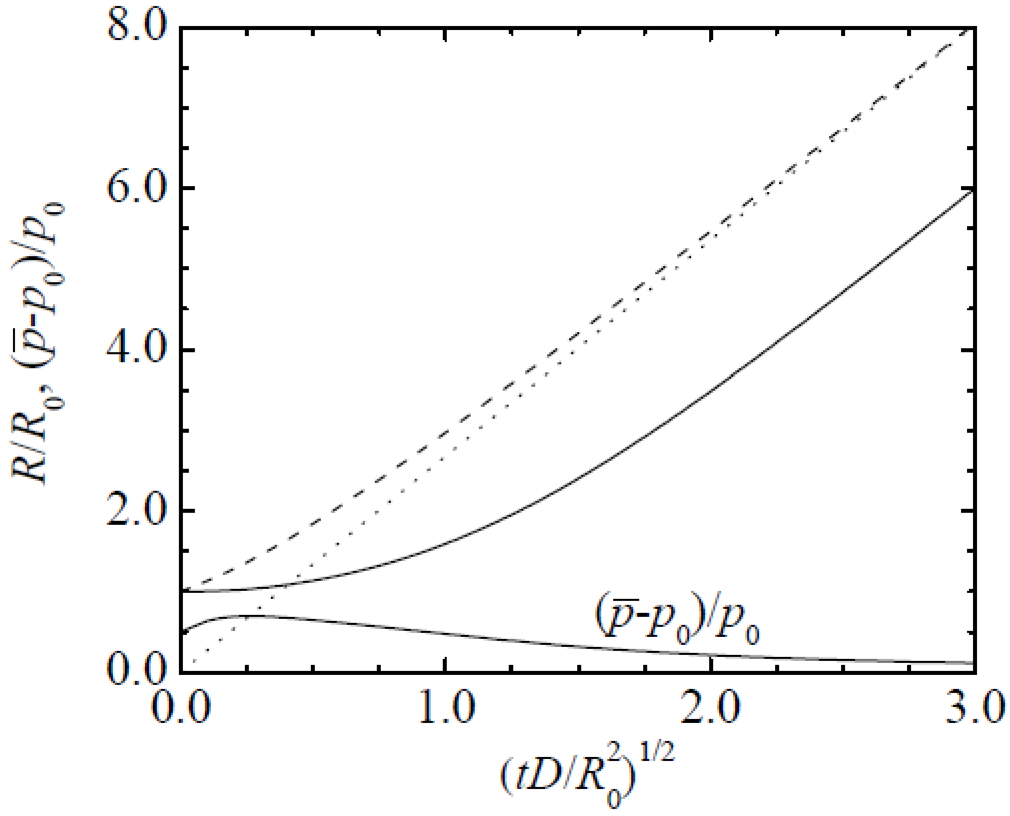

Figure 18.4 Bubble radius and pressure versus time during bubble growth for the following parameter values: N_w = 1 and ϵ = 0.001. Solid lines are for diffusion-induced case where N_n = 0.1, $N_{\Delta p}$ = 0.5 and N_γ = 0.25. Dashed line is diusion-controlled case N_n = N_γ = 0; dotted line is for (18.30) with = 1.34.

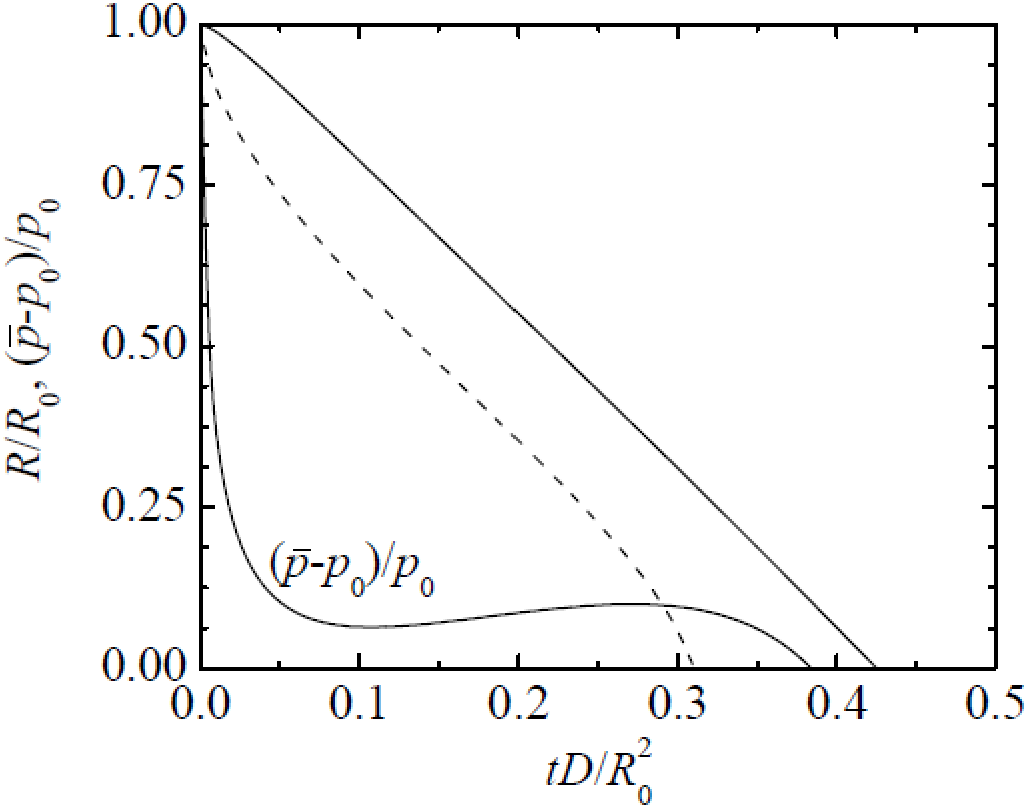

Figure 18.5 Bubble radius and pressure versus time during bubble collapse for the following parameter values: $N_w = -1$ and ϵ = 0.001. Solid lines are for diffusion-induced case where N_n = 0.1, $N_{\Delta p}$ = 2 and N_γ = 0.5. Dashed line is diffusion-controlled case N = N = 0.

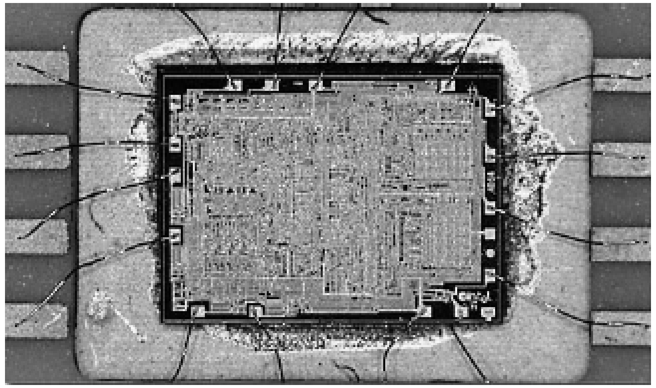

Figure 19.1 Image of the Intel 4004 microprocessor circa 1970 with overall dimensions of $\backsim$ 10mm x 10 mm. This device contains 2300 transistors and has device features of $\backsim$ 10 μm in size. Current microprocessors have device features w$\backsim$ sizes 25nm and over 500 million transistors.

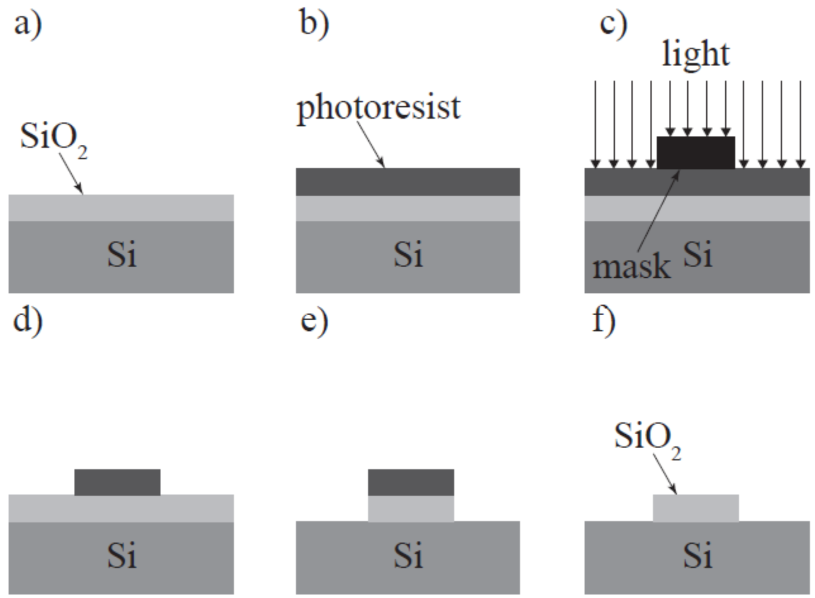

Figure 19.2 Schematic of selected semi-conductor processing steps: a) Si wafer with SiO_2 layer; b) surface coated with positive photoresist film; c) exposure of photoresist through mask; d) photoresist after selective removal; e) selective removal of SiO_2 layer by etching; f) SiO_2 feature left after photoresist removal.

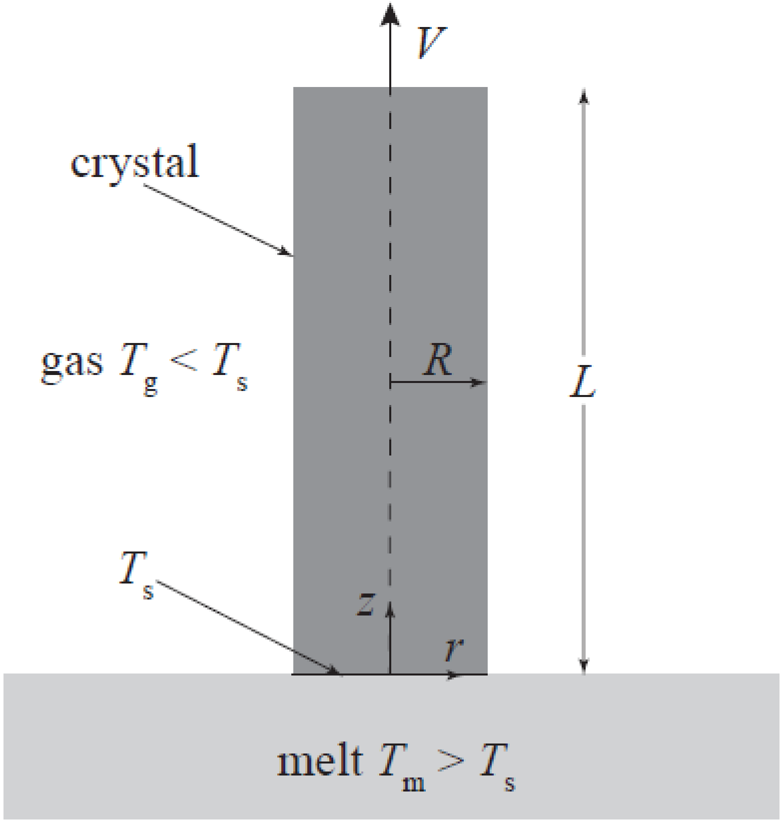

Figure 19.3 Schematic of Czochralski crystal growth process.

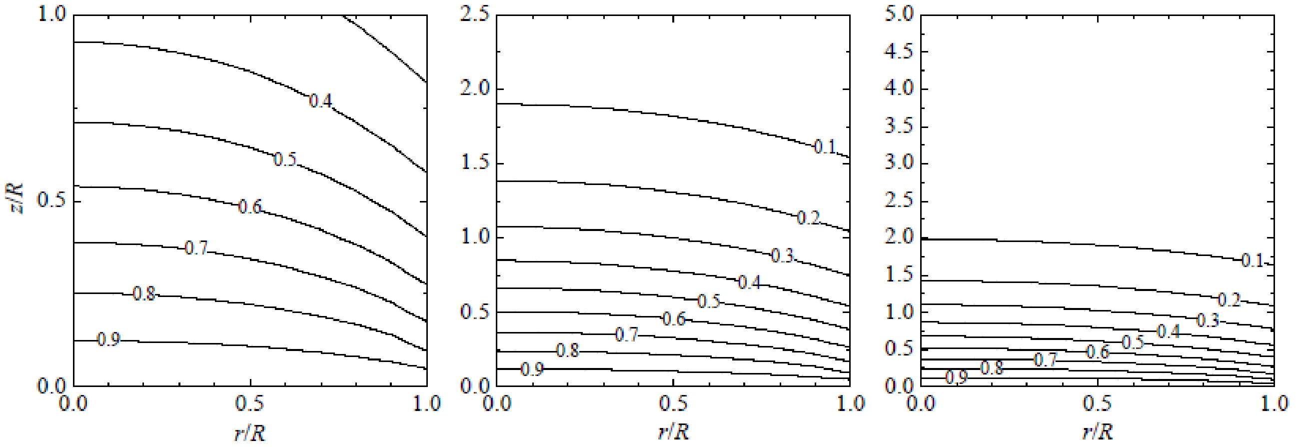

Figure 19.4 Normalized temperature (*T* - *Tg*)/(*Ts* - *Tg*) isotherms in Czochralski crystal growth process given by (19.8) with N_{Bi} = 1.0 for three crystal lengths *L/R* = 1, 2.5, 5 (left to right).

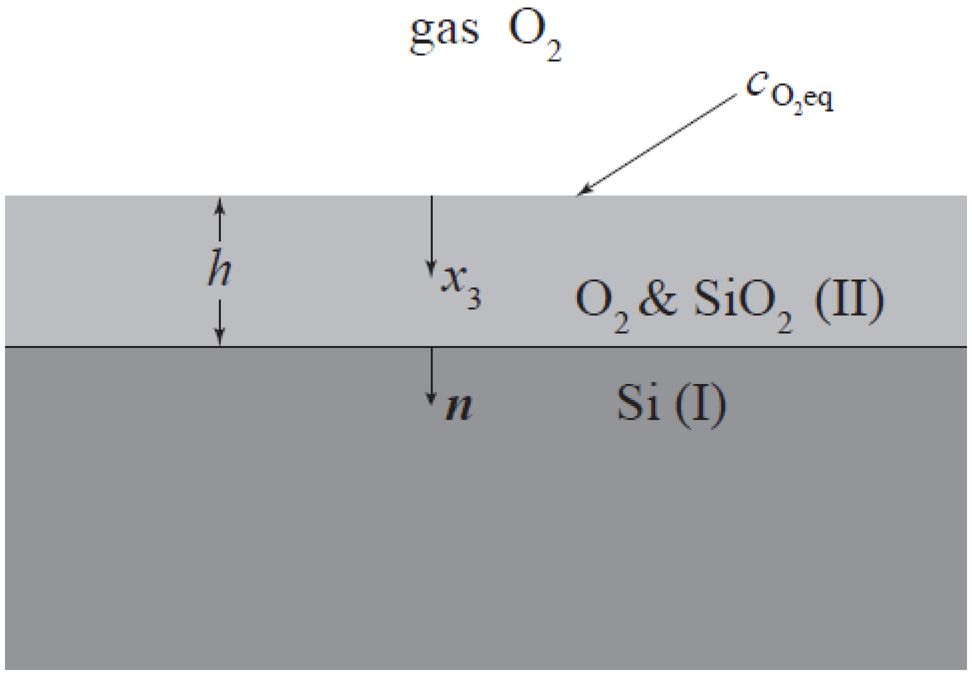

Figure 19.5 Schematic of Si oxidation process showing SiO_2 layer having thickness *h*.

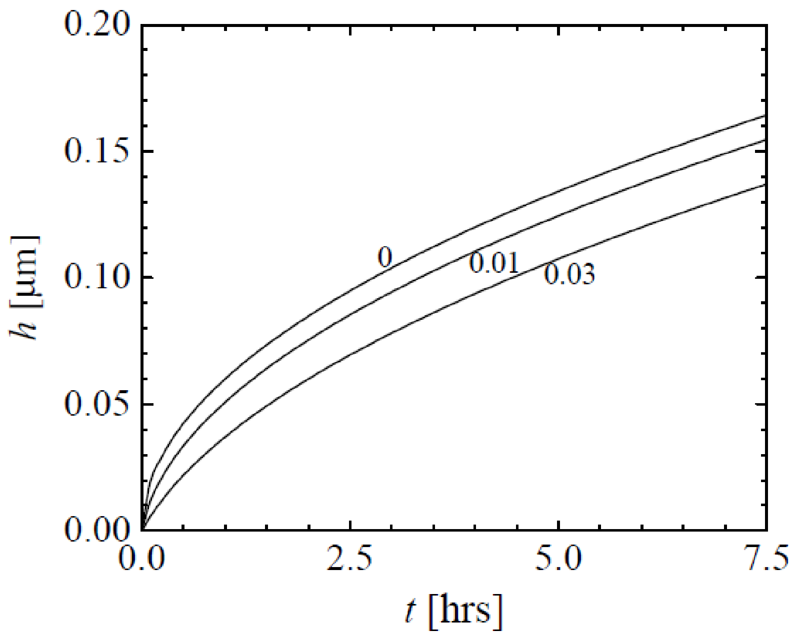

Figure 19.6 Oxide lm thickness h in m versus time t in hours given by (19.28) with $h \to hk^{\mathrm{s}}/D$ and $t \to t(k^{\mathrm{s}})2/D$, and the following parameter values: $\varepsilon = 10^{-5}$. $D = 5 \times 10^{-14}$ m^2/s. Different curves correspond to different values of *D/ks* = 0.0, 0.01, 0.03μm (top to bottom).

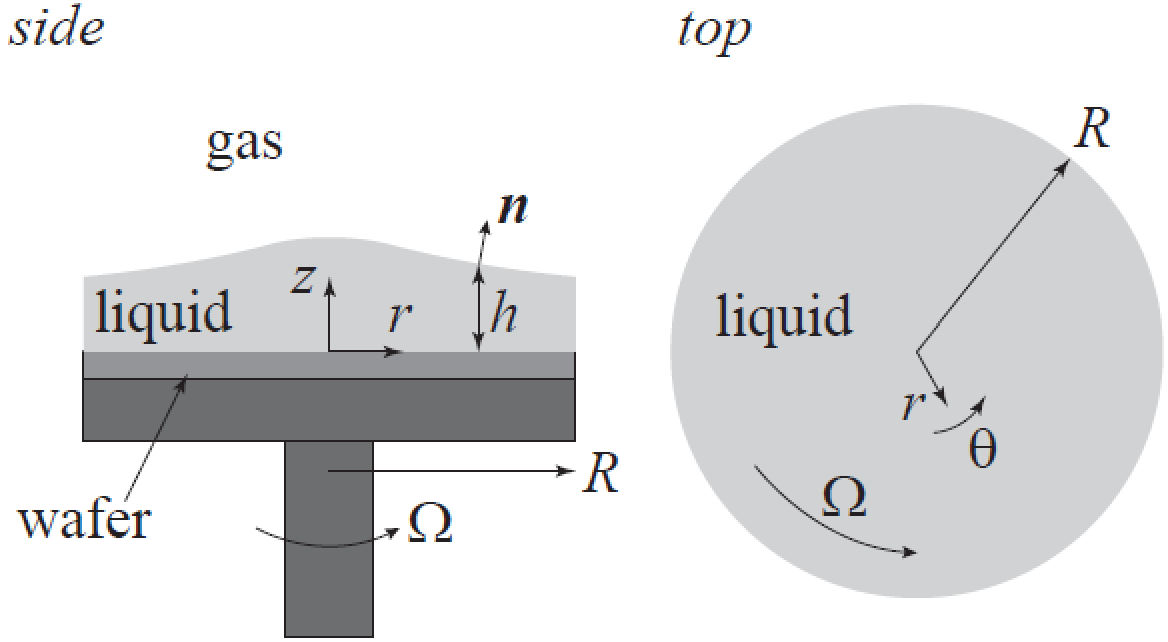

Figure 19.7 Schematic of spin coating process. Note that film thickness *h* is exaggerated for clarity.

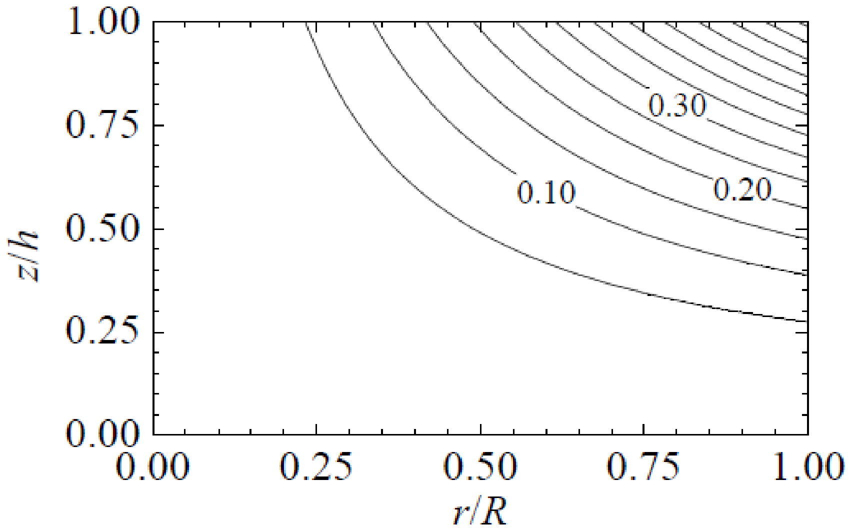

Figure 19.8 Normalized stream function $\psi/(Vh_0^2)$ for velocity within a uniform film given by (19.43) and (19.44) in terms of the stream function given in (19.49) as found in Exercise 19.8. Contours are for constant values of ψ/h^3.

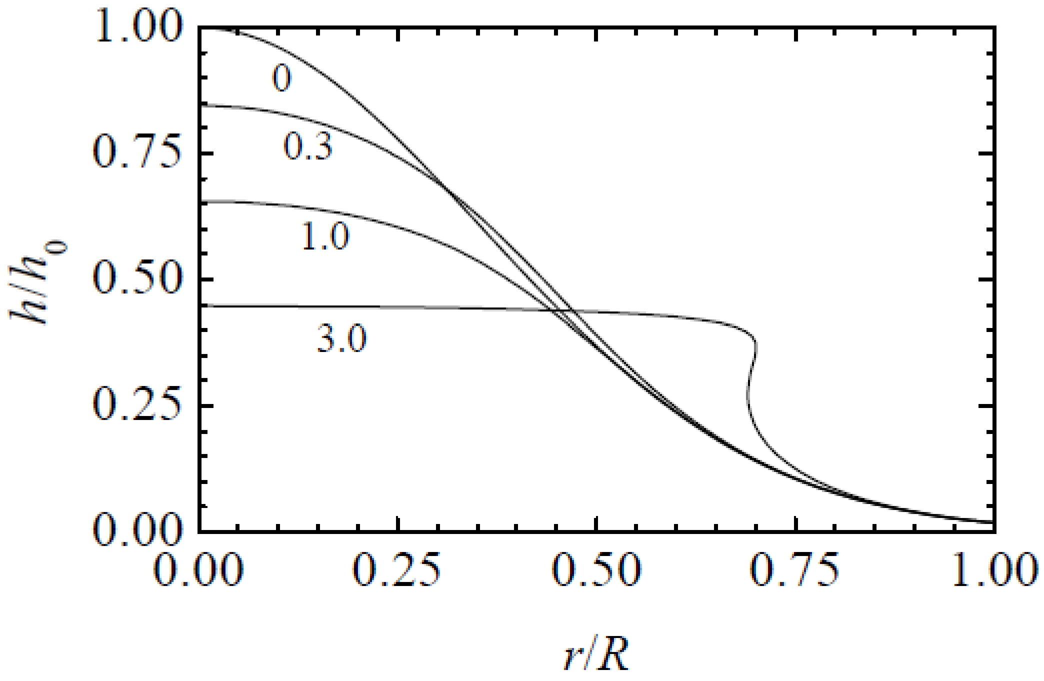

Figure 19.9 Evolution of film prole predicted by (19.48) with an initially Gaussian profile $h' = \exp(-4r'^2)$ Different proles are for different values of time *t* = 0, 0.3, 1.0, 3.0 (top to bottom).

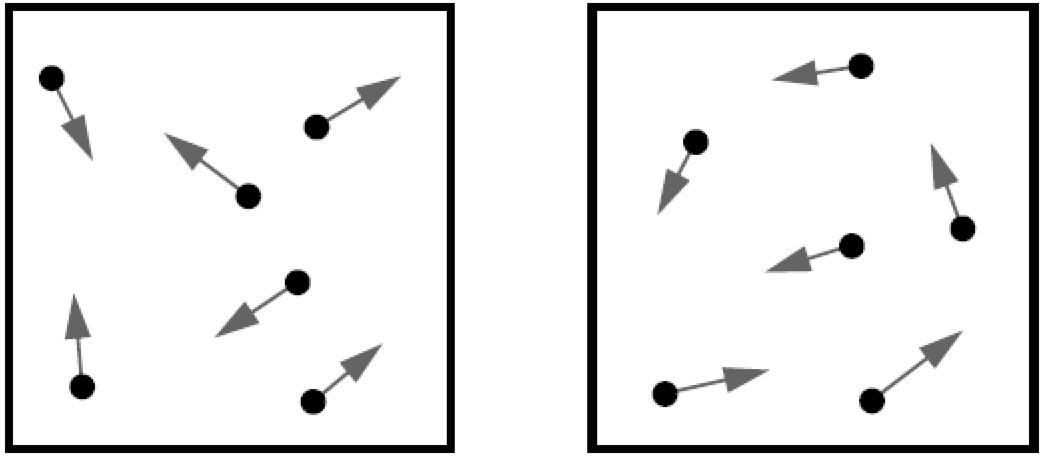

Figure 20.1 Two equivalent particle configurations for a gas of spherical particles.

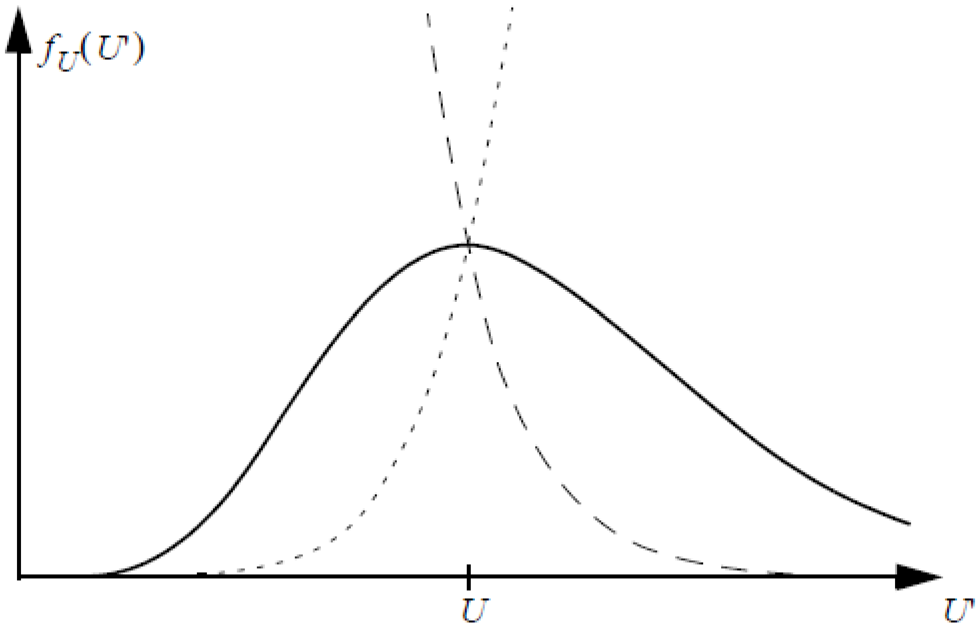

Figure 20.2 Peaked distribution of a macroscopic variable such as the internal energy *U'* in a canonical ensemble.

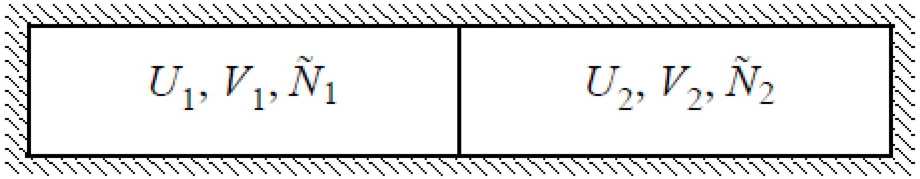

Figure 20.3 Two subsystems brought in contact to identify the statistical expression for the entropy.

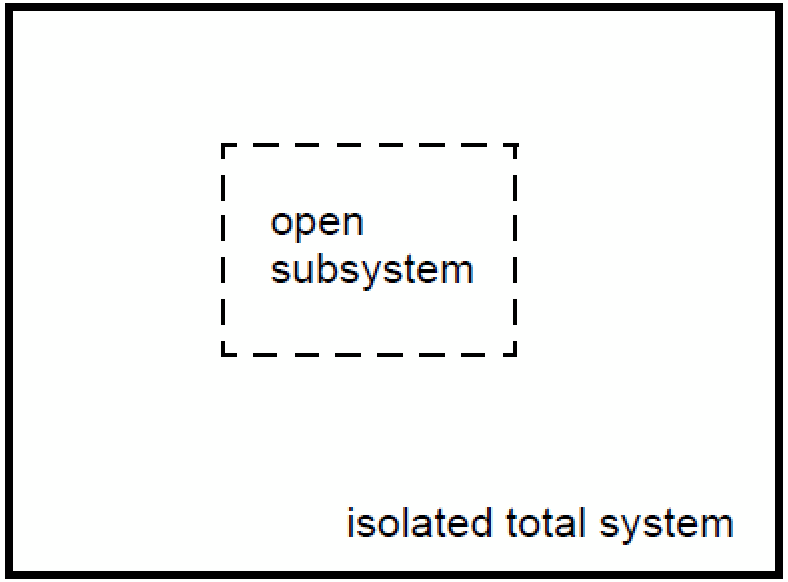

Figure 20.4 Open subsystem with fluctuating internal energy and particle number within a large equilibrium bath.

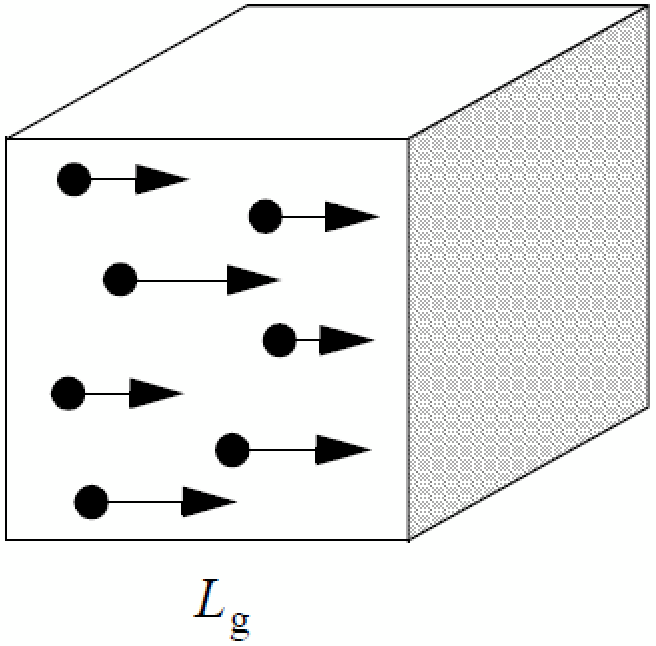

Figure 21.1 Gas particles with a positive velocity component toward the right wall of a cubic container (particles with a negative velocity component are not shown). [Reprinted with permission from Öttinger, *Beyond Equilibrium Thermodynamics* (Wiley, 2005). Copyright by John Wiley & Sons.]

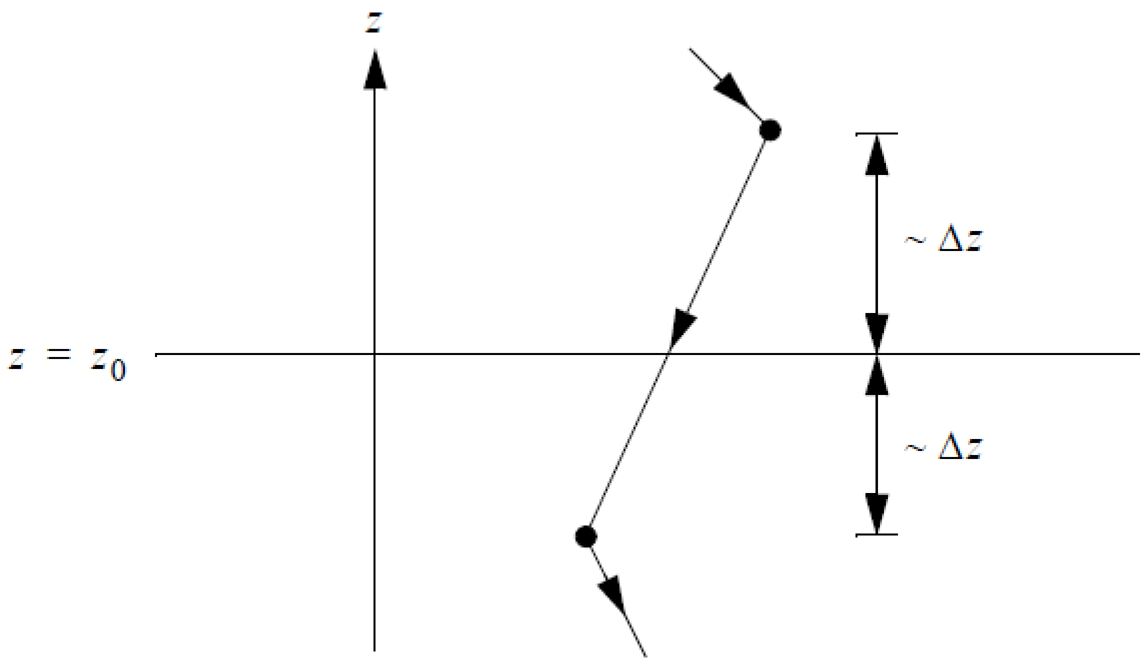

Figure 21.2 A particle has a collision a distance Δz above the plane and transports property *a* to another particle a distance Δz below the plane. [Reprinted with permission from Öttinger, *Beyond Equilibrium Thermodynamics* (Wiley, 2005). Copyright by John Wiley & Sons.]

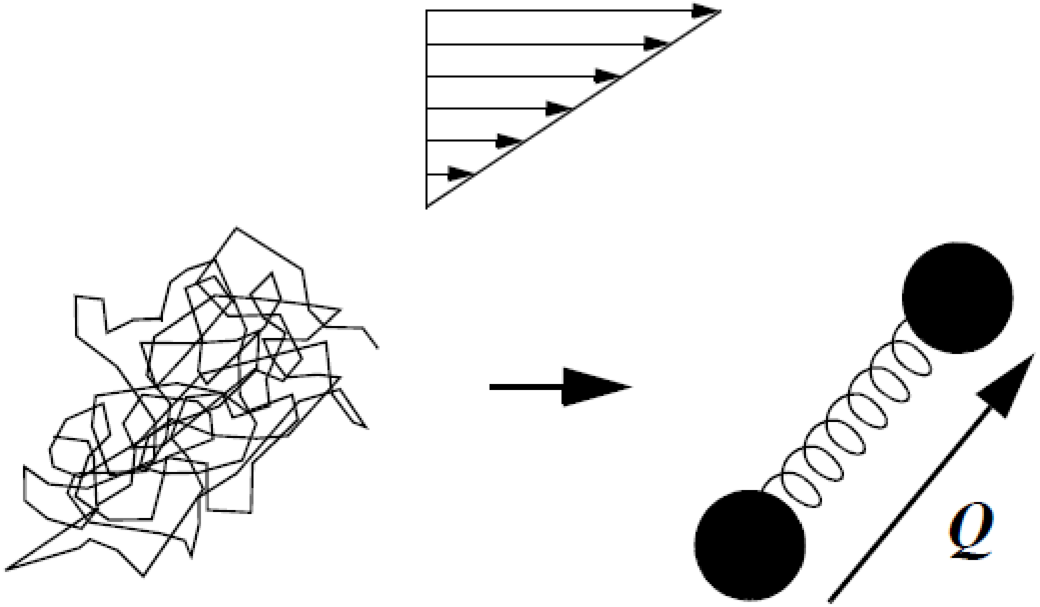

Figure 22.1 Under ow conditions, such as the indicated shear ow, polymer molecules become stretched and oriented. To develop a simple kinetic theory, we model the polymer conformations by a dumbbell.

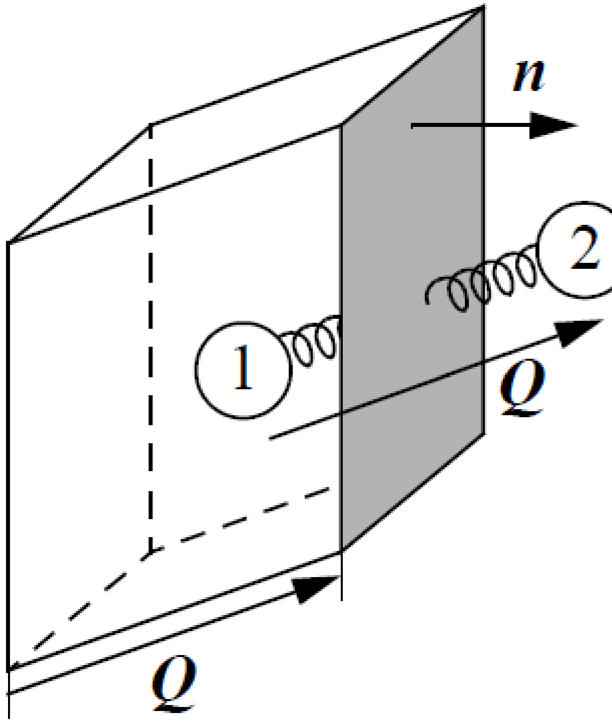

Figure 22.2 The volume that must be occupied by bead 1 when the connector vector ***Q*** intersects the shaded rectangle with unit normal vector ***n***.

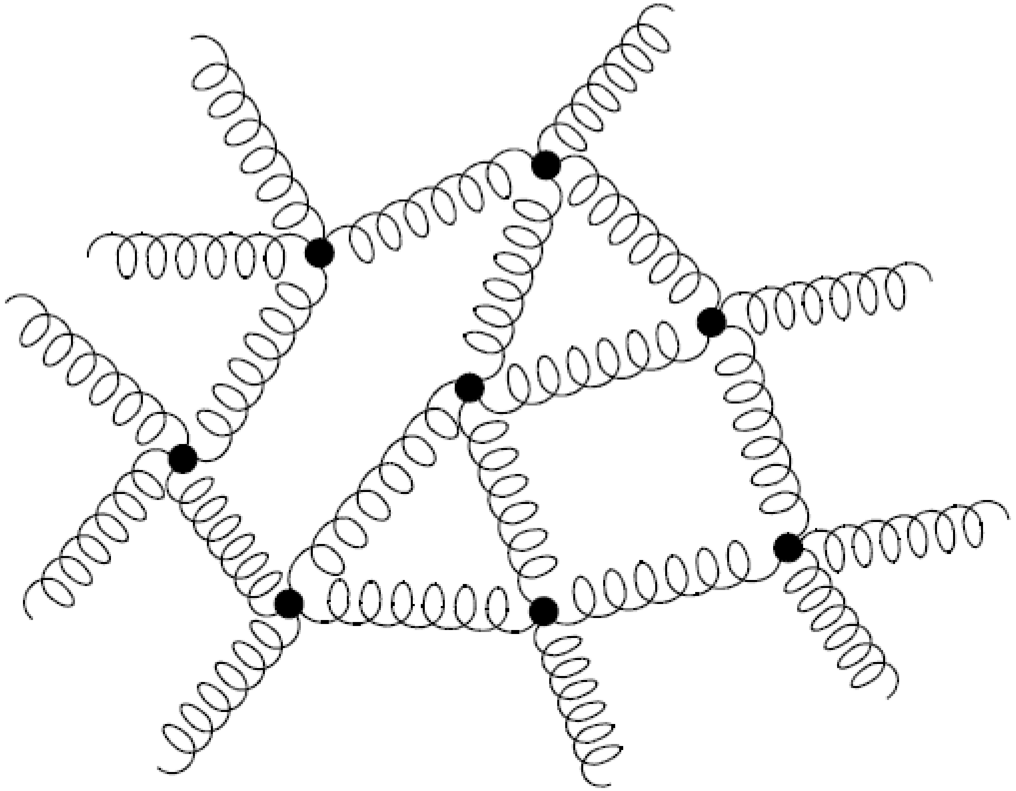

Figure 22.3 Temporary network conformation.

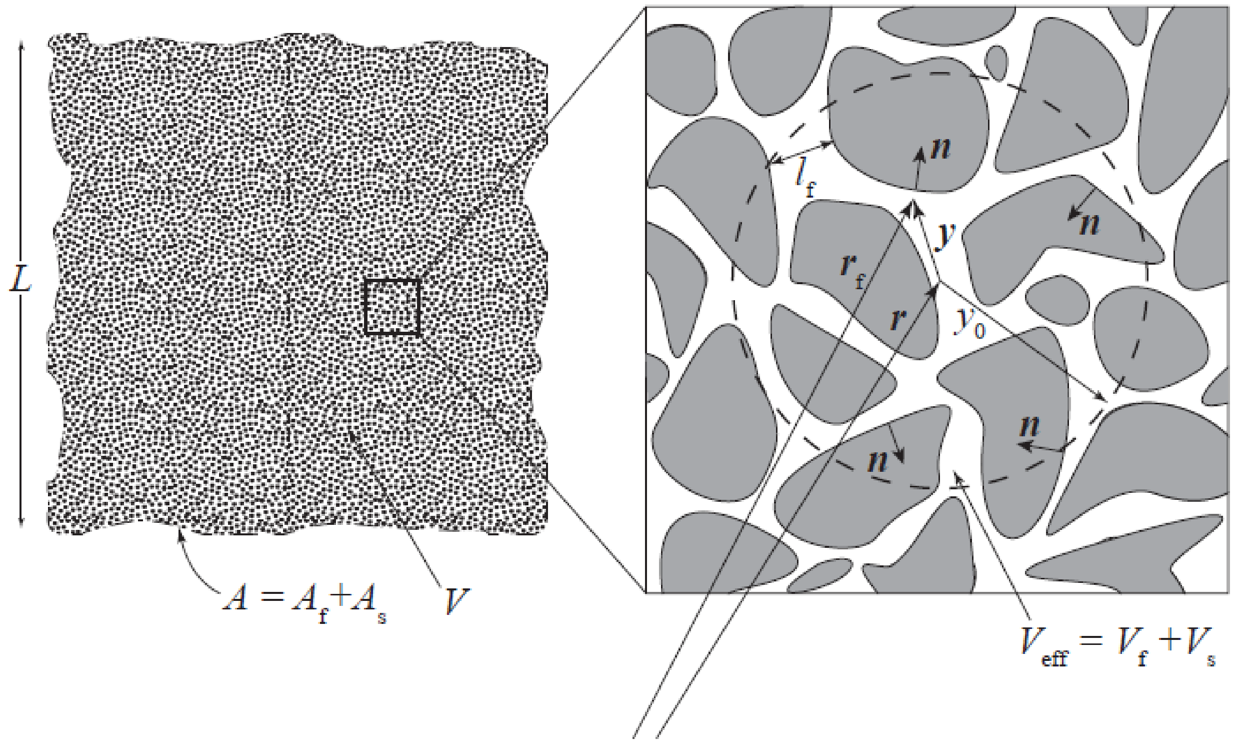

Figure 23.1 Schematic of porous medium with magnified view of averaging volume V_{eff} at position $\boldsymbol{r}$.

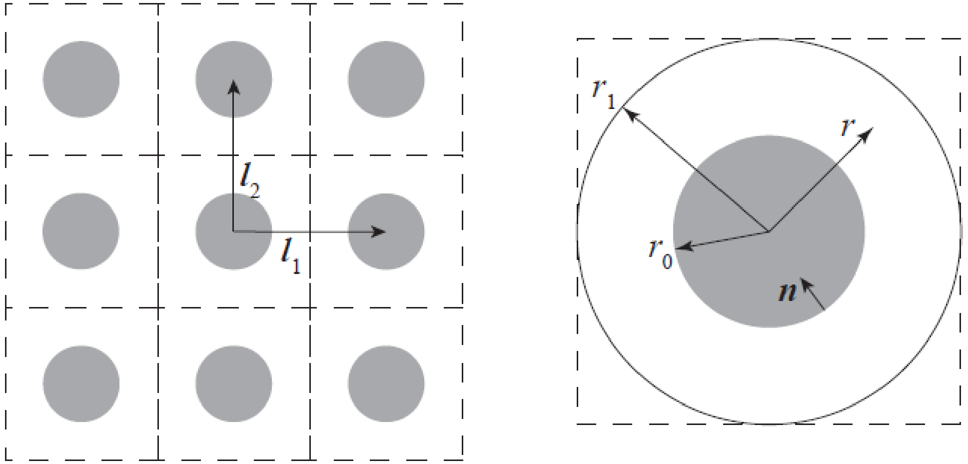

Figure 23.2 Schematic of spatially periodic unit cells (left) and a single unit consisting of a spherical solid surrounded by a spherical fluid (right).

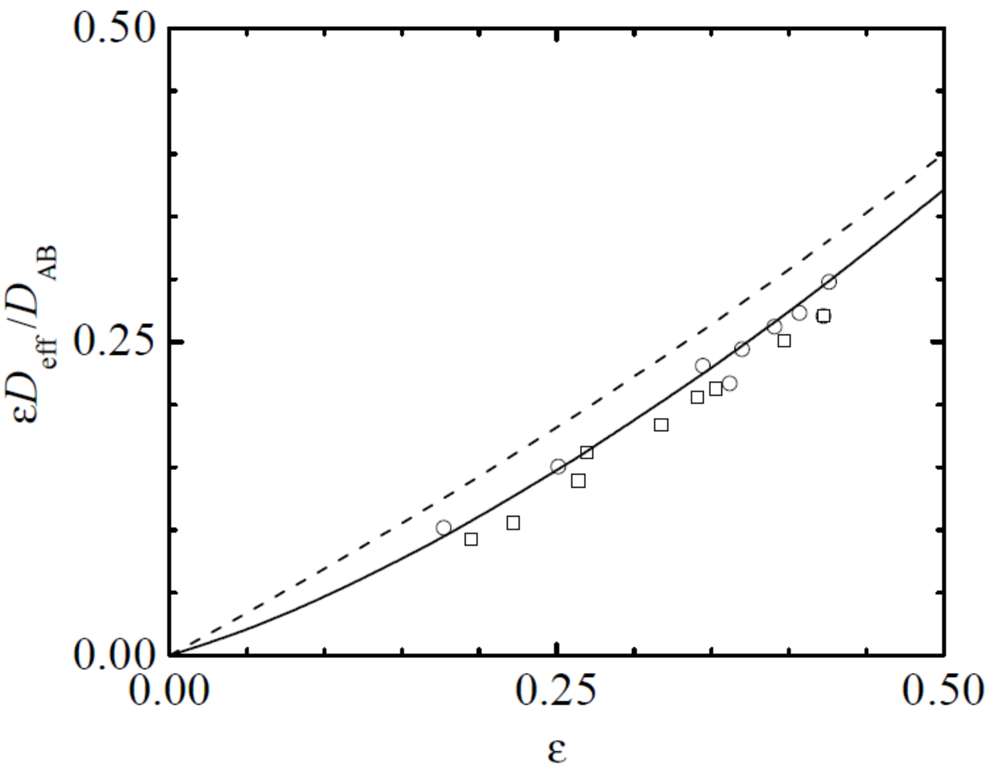

Figure 23.3 Comparison of experimental effective diffusivities in porous media comprised of spheres (circles) and sand (squares) and model predictions from (23.32){(23.34) for a periodic array of spheres (solid curve) and for (23.37) (dashed curve): $\varepsilon D_{\rm eff}/D_{\rm AB} = 2\varepsilon/(3-\varepsilon)$. [Adapted from Whitaker, *The Method of Volume Averaging* (Kluwer, 1999)].

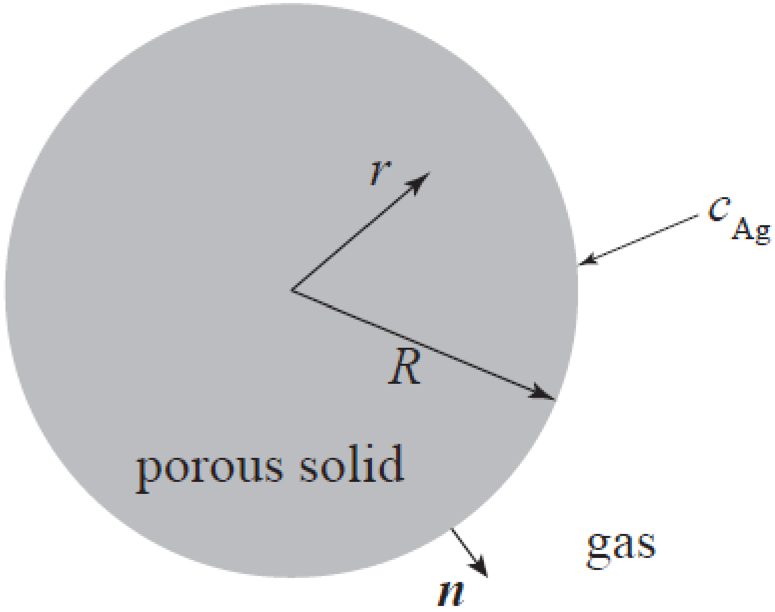

Figure 23.4 Schematic of a spherical porous catalyst particle with radius *R* surrounded by a gas that maintains concentration c_{Ag} at particle surface.

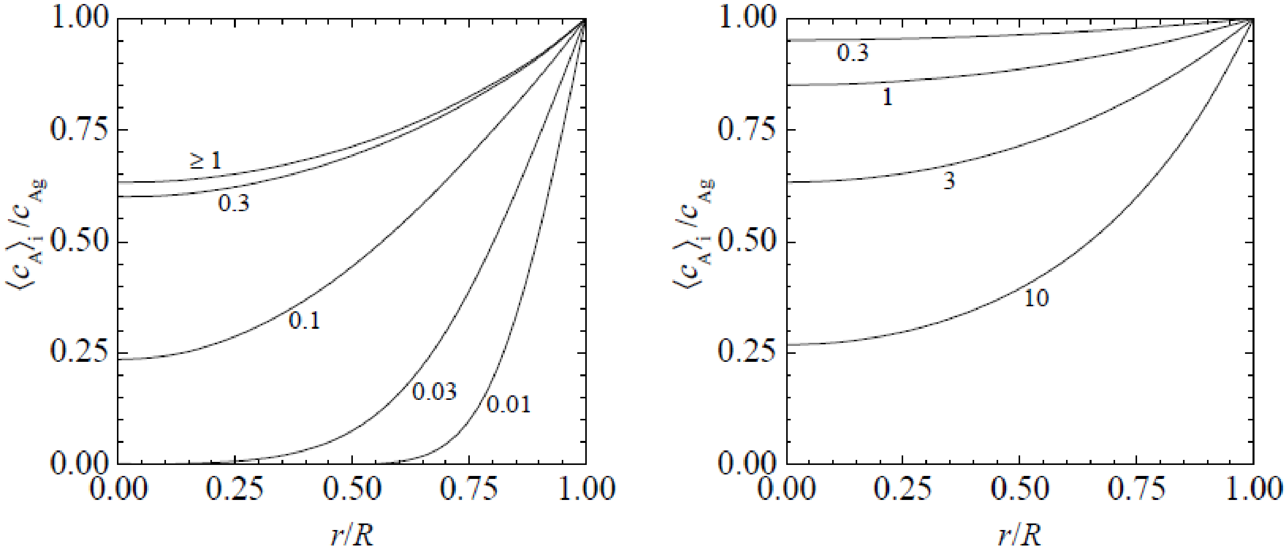

Figure 23.5 Reactant concentration prole within catalyst particle from (23.40) for N_{Da} = 3 at different times $D_{\mathrm{eff}}t/R^2$ = 0.01, 0.03, 0.1, 0.3, 1 (left); steady state reactant concentration prole from (23.41) for different values of N_{Da} = 0.3, 1, 3, 10 (right).

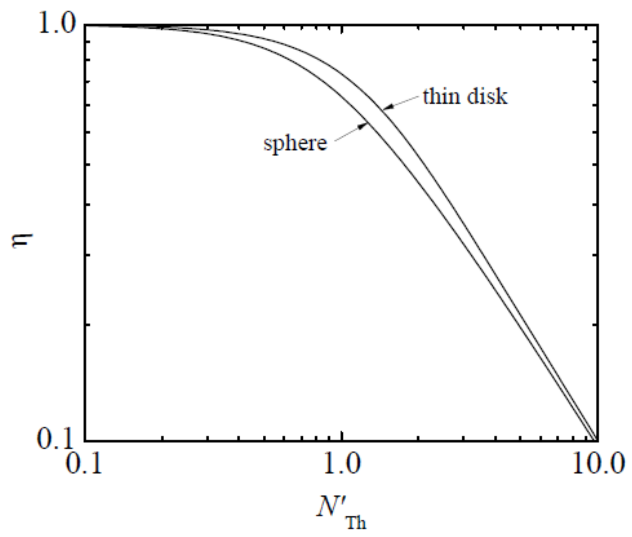

Figure 23.6 Effectiveness factor *n* for catalyst particles with spherical (23.43) and thin disk (23.52) shapes as a function of modified Thiele modulus N'_{Th}

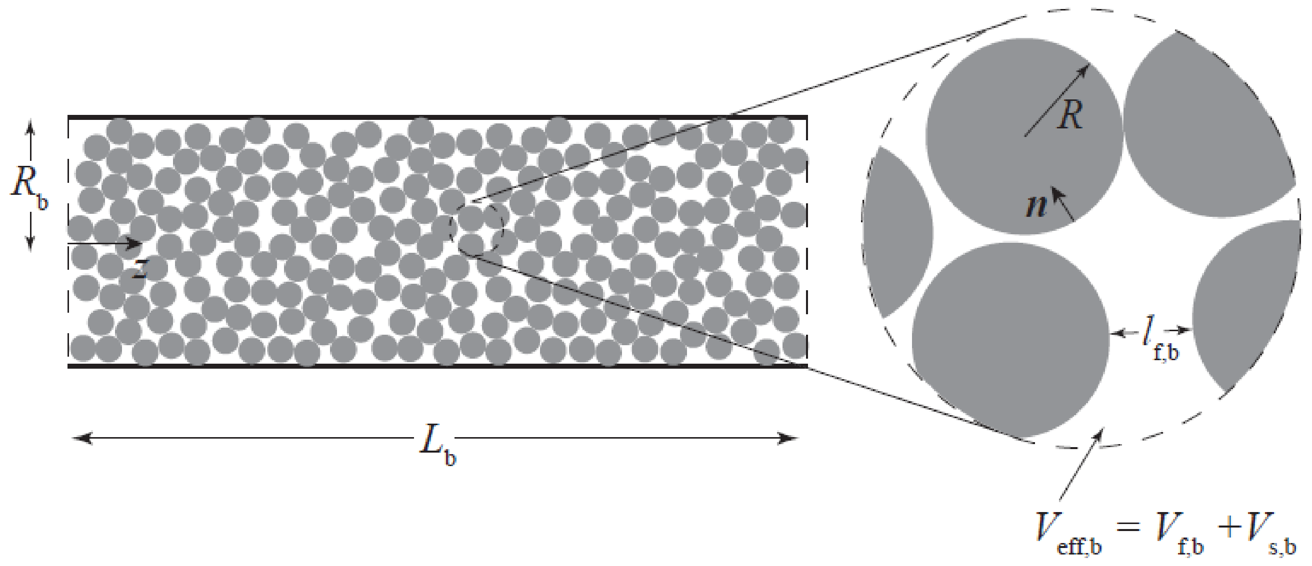

Figure 23.7 Schematic of tubular packed bed reactor having length L_b and radius R_b containing spherical catalyst particles with magnified view of averaging volume $V_{\mathrm{eff,b}}$.

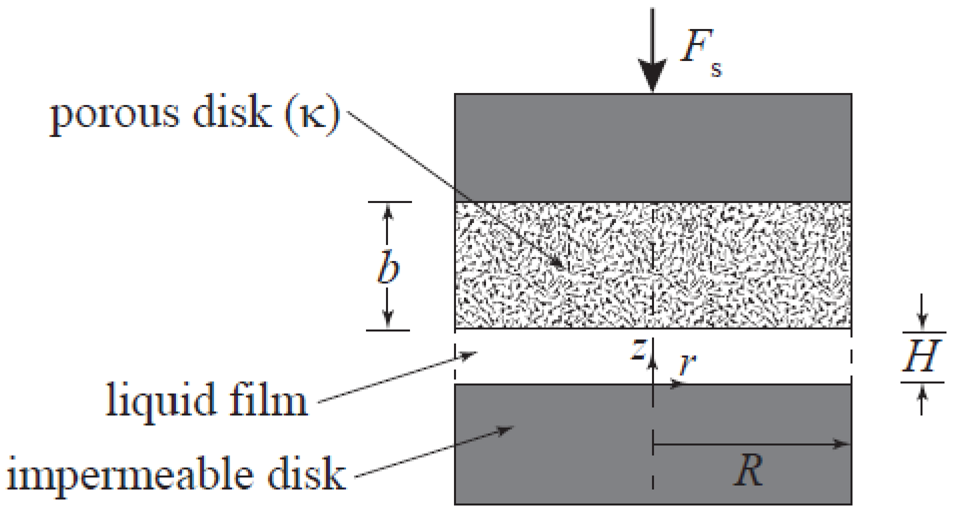

Figure 23.8 Schematic of liquid lm between porous and impermeable disks.

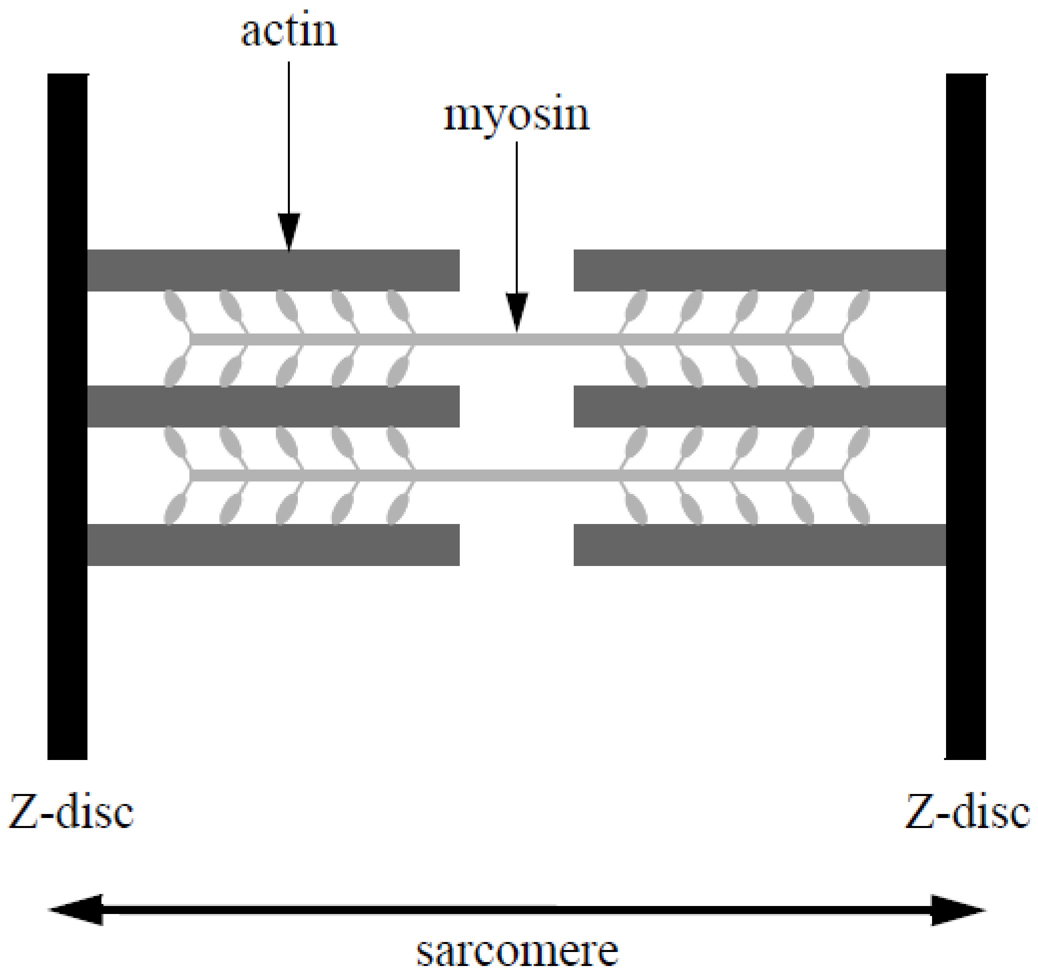

Figure 24.1 A sarcomere as the basic unit of a muscle. The ends of the myosin laments are actually attached to the Z-disc by means of highly elastic molecules which, for simplicity, are not shown in the figure. [For a more realistic sketch see, for example, Kim et al., Trends Cell Biol. 18 (2008) 264.]

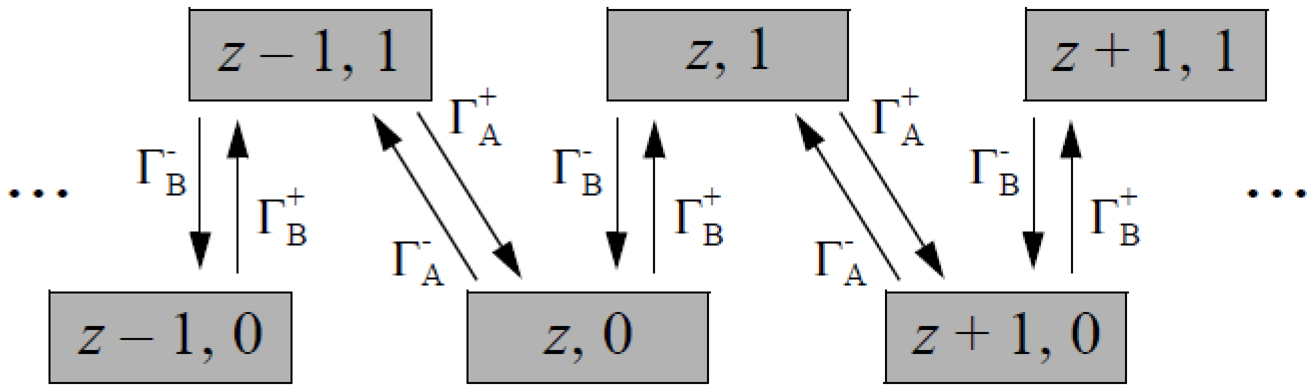

Figure 24.2 Transition rates for the two-state model of translational motors.

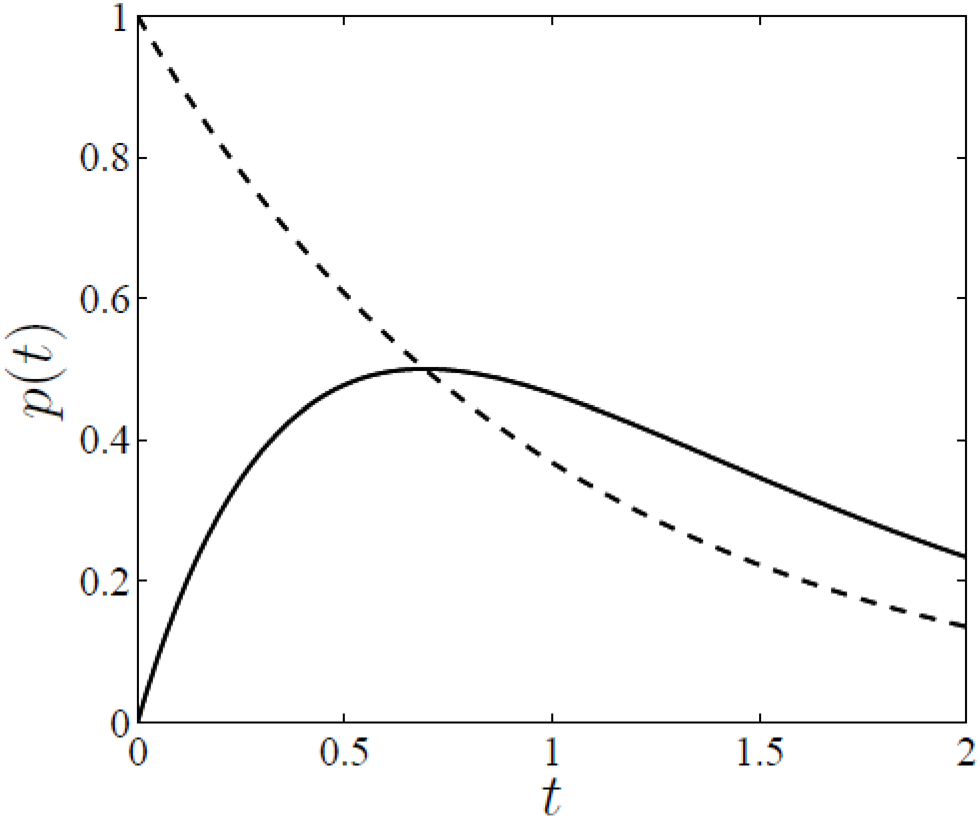

Figure 24.3 Dwell time distribution (24.18) for $\Gamma_1 = 1, \Gamma_2 = 2$ (continuous line); for comparison, the single exponential decay e^{-t} is also shown (dashed line).

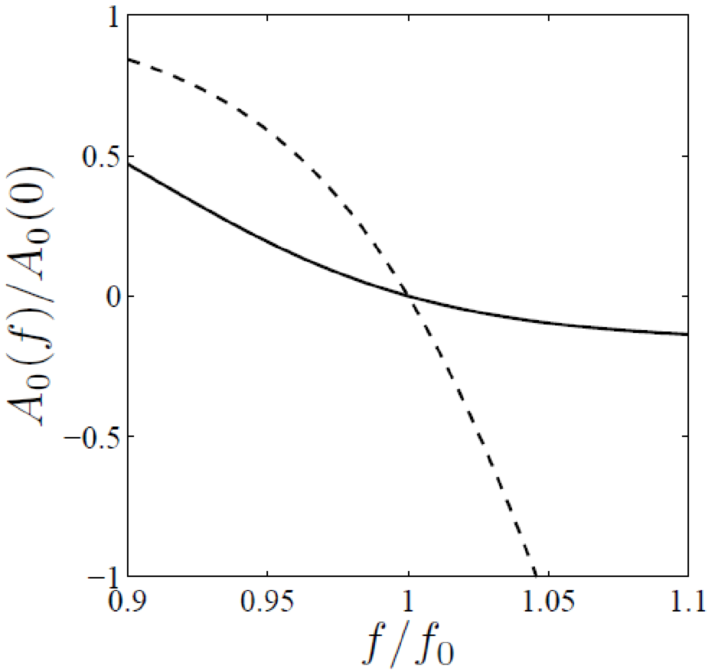

Figure 24.4 Normalized forward drift velocity as a function of the backward pulling force *f* divided by the stall force *f0*; the continuous and the dashed lines correspond to the rate parameters (24.2) and (24.3), respectively, where the coefficients are chosen as c+ = 1, c_= 0:2, and *f0* = 20.

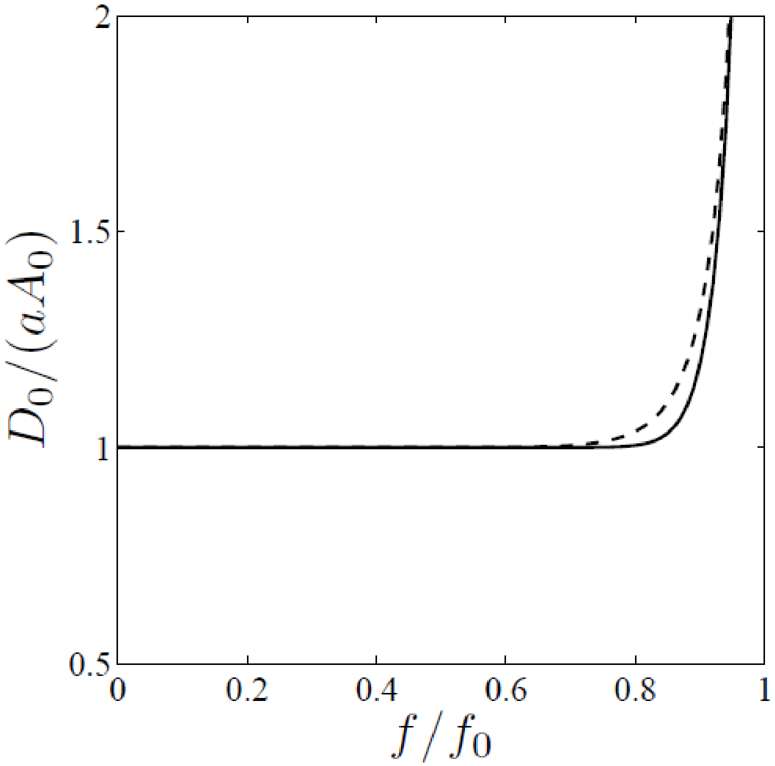

Figure 24.5 Randomness as a function of the backward pulling force *f* divided by the stall force *f0*; the continuous and the dashed lines correspond to the rate parameters (24.2) and (24.3), respectively, where the coefficients are chosen as c+ = 1, c_ = 1, and *f0* = 20.

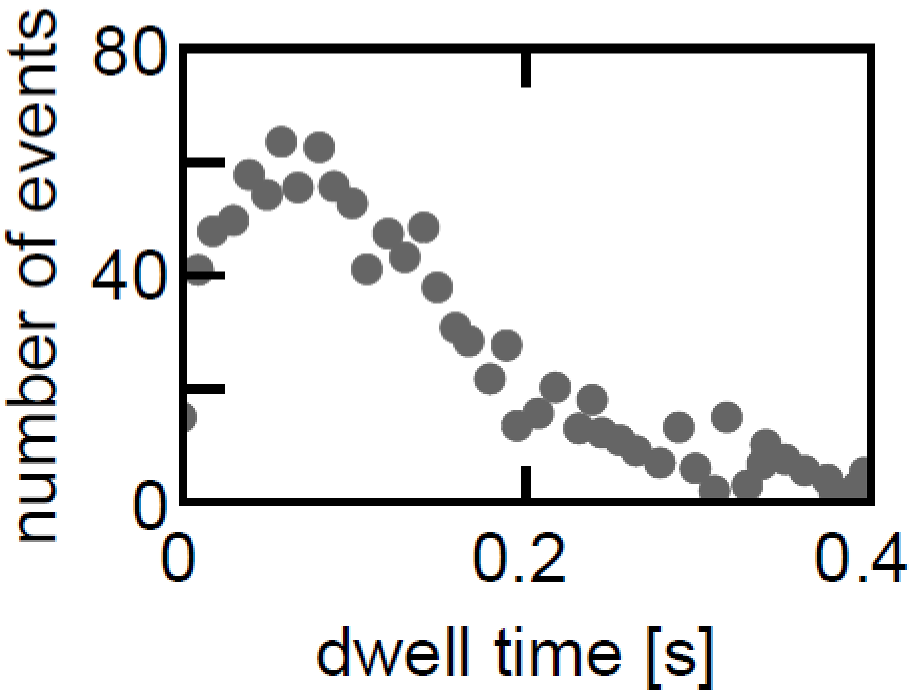

Figure 24.6 Experimental data for the dwell time histogram for the myosin V motor protein. [Redrawn from Purcell et al., Proc. Natl. Acad. Sci. U.S.A. 102 (2005) 13873.]

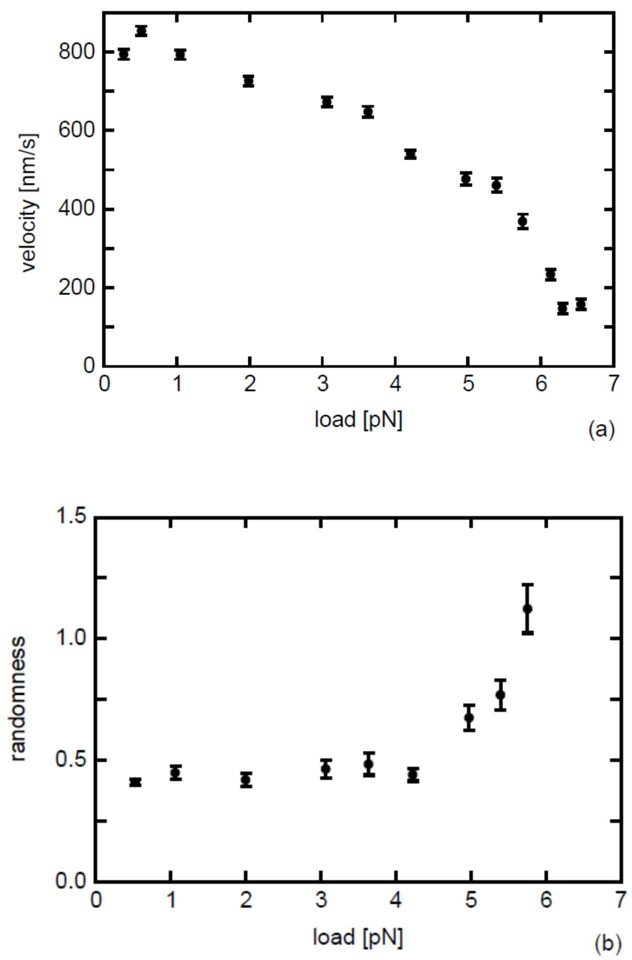

Figure 24.7 Experimental data for (a) the molecular motor velocity and (b) the randomness parameter for kinesin moving along microtubules at high ATP concentration. [Redrawn from Visscher et al., Nature 400 (1999) 184.]

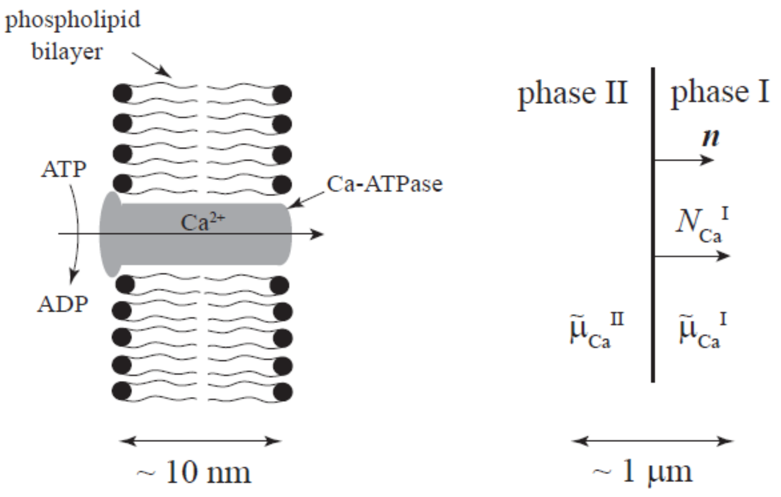

Figure 24.8 Schematic of phospholipid bilayer membrane with Ca-ATPase protein for active transport of Ca2+ (left); idealization of membrane as an interface with molar flux $N_{\mathrm{Ca}}^{\mathrm{I}}$ from interface into phase I and $\tilde{\mu}_{\mathrm{Ca}}^{\mathrm{I}} > \tilde{\mu}_{\mathrm{Ca}}^{\mathrm{II}}$ (right).

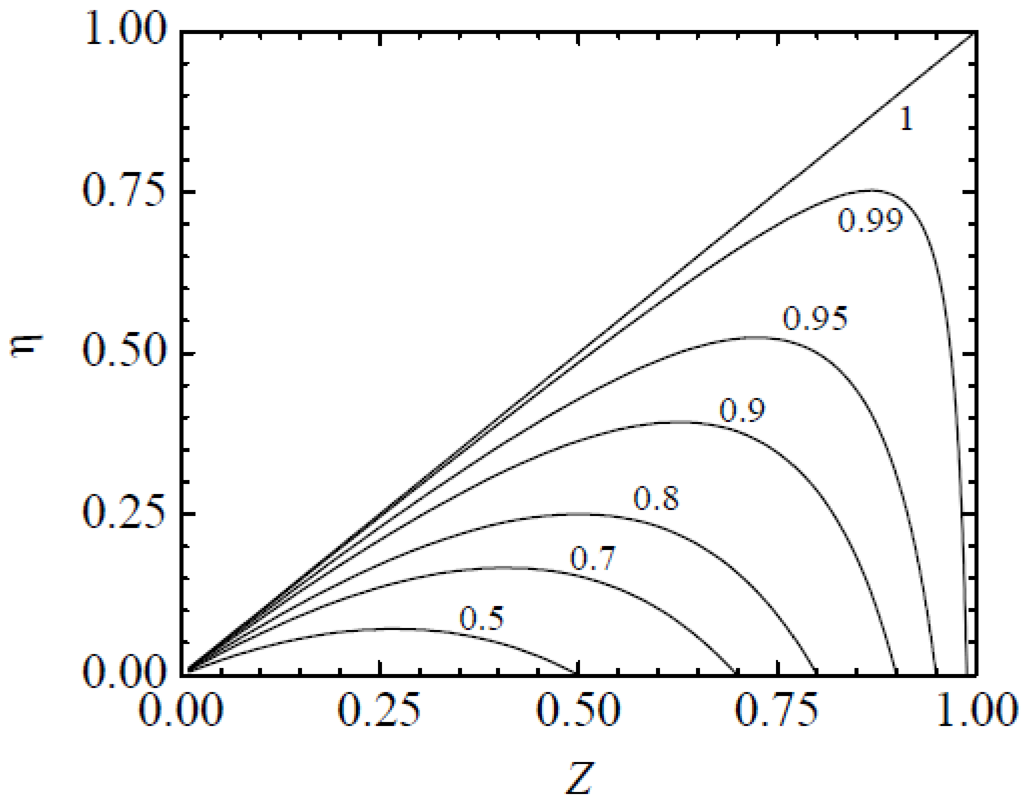

Figure 24.9 Thermodynamic efficiency *n* of Ca2+ ion pump versus Z for different values of the coupling coefficient *q* given by (24.29) and (24.30).

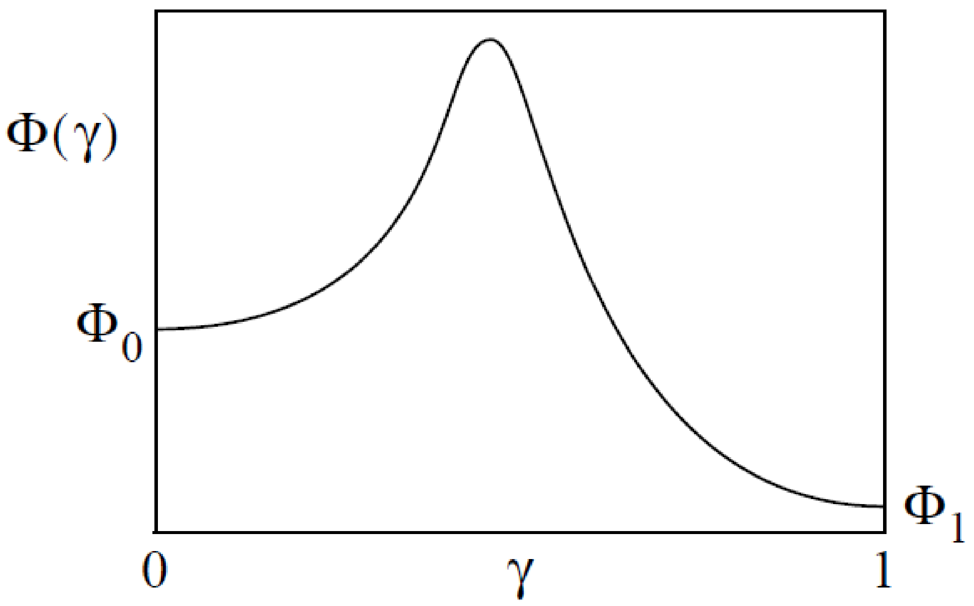

Figure 24.10 Qualitative behavior of the activation energy $\Phi(\gamma)$.

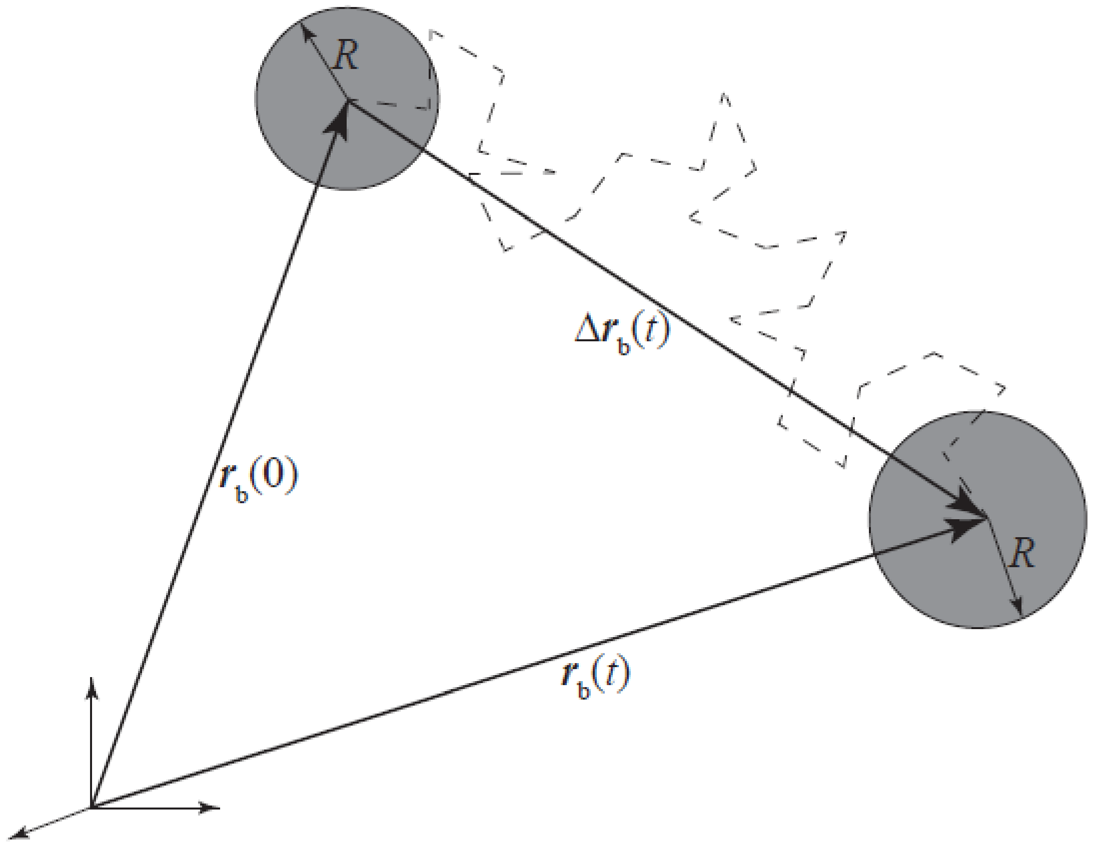

Figure 25.1 Schematic of Brownian motion of spherical particle (bead) with radius *R* showing particle position ***rb*** and displacement Δ***rb*** vectors.

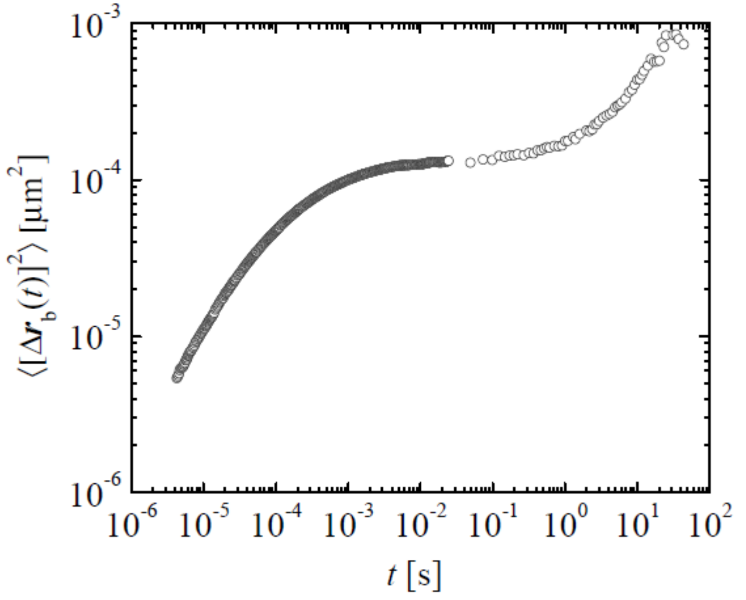

Figure 25.2 Mean-square displacement for microbead rheology experiment performed on a wormlike micellar solution measured using diffuse wave spectroscopy [see Willenbacher et al., Phys. Rev. Lett. 99 (2007) 068302].

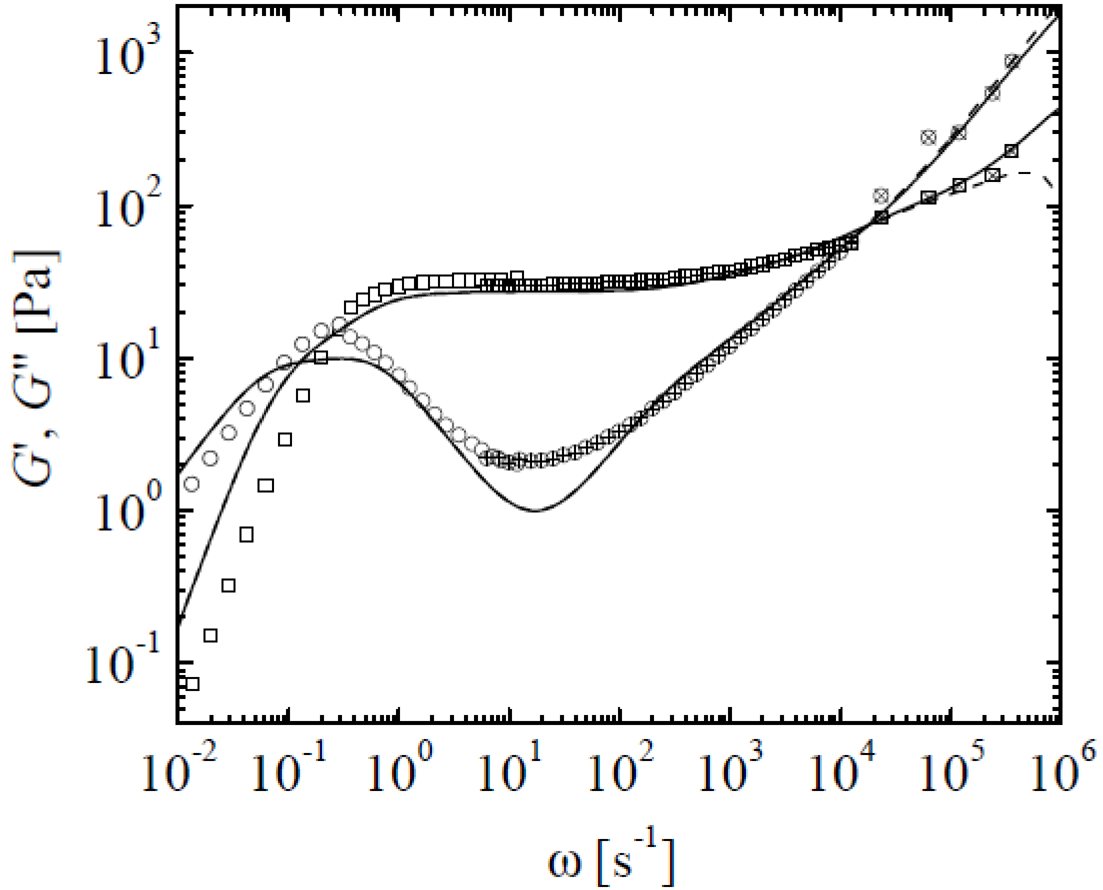

Figure 25.3 Complex modulus for a wormlike micellar solution from the mean-square displacement data in Figure 25.2 and from mechanical rheology: *G'* (squares); *G"* (circles) [see Willenbacher et al., Phys. Rev. Lett. 99 (2007) 068302]. The solid curves are obtained using (25.18) and the dashed curves using (25.19) [curves provided by Tsutomu Indei at IIT, Chicago].

Figure 26.1 Lord (John William Strutt) Rayleigh (1842-1919).

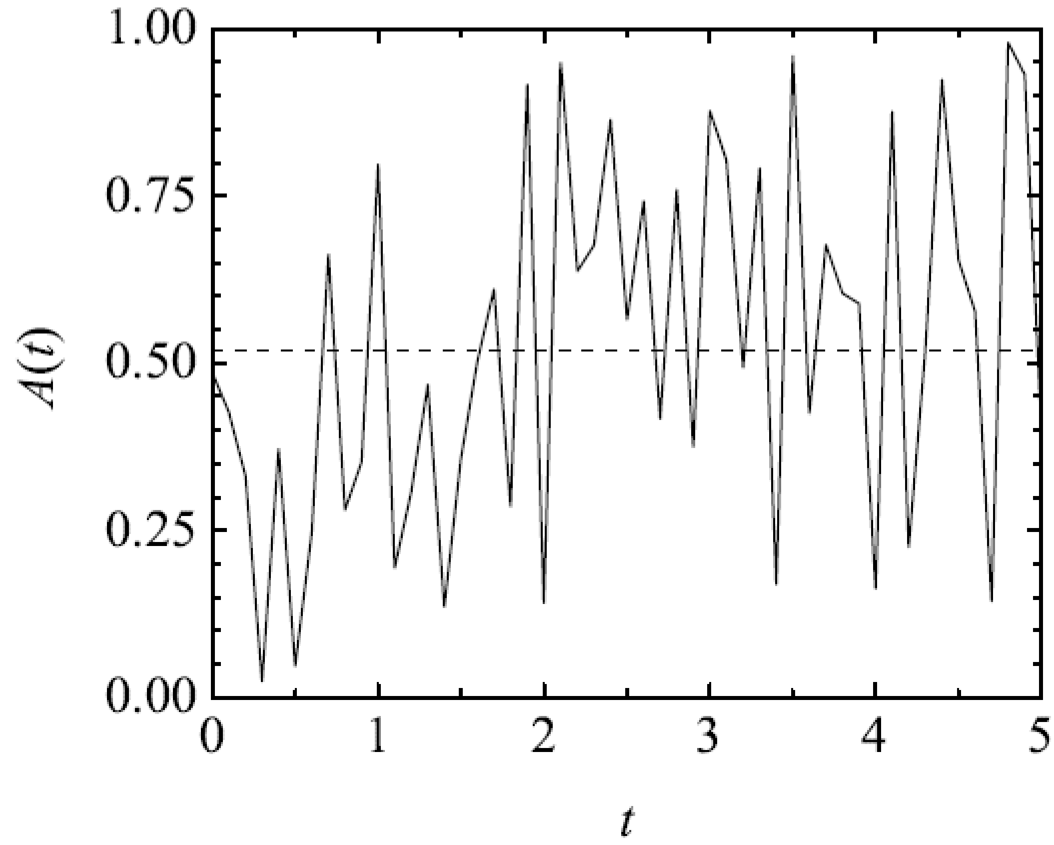

Figure 26.2 Plot of the time dependence of a property *A(t)* fluctuating about its average value <*A*>indicated by the dashed line.

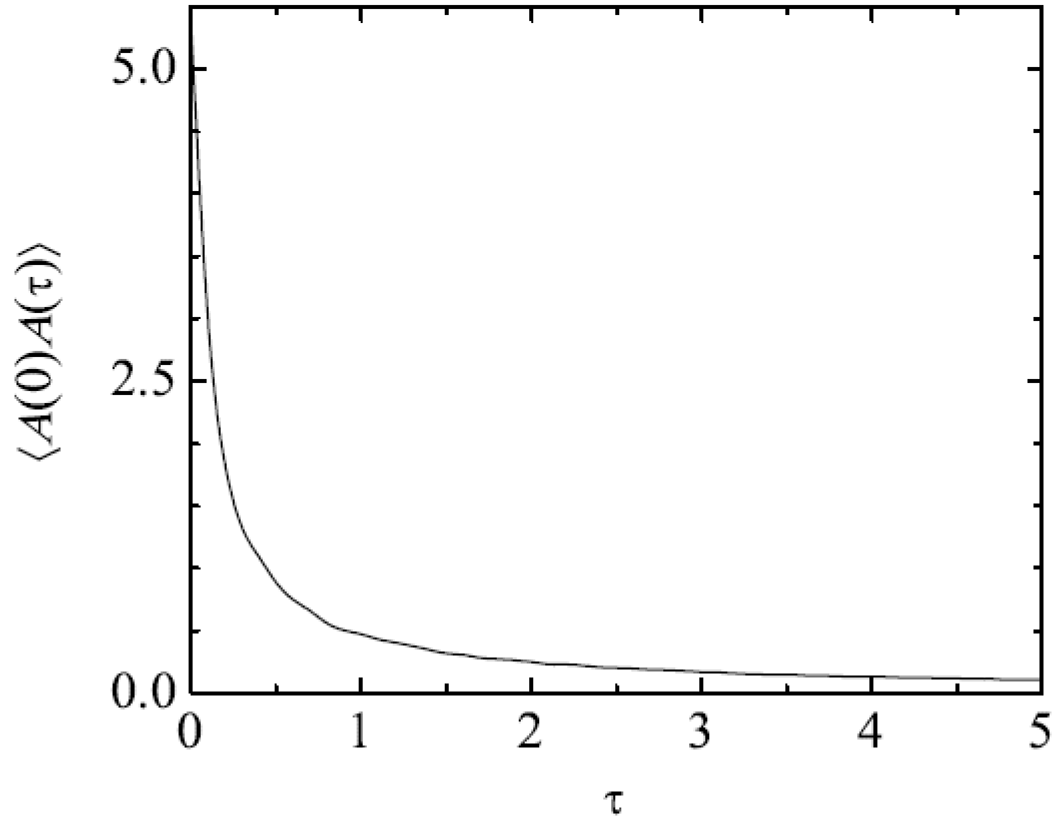

Figure 26.3 Schematic plot of time dependence of autocorrelation function $\langle \delta A(0) \delta A(\tau) \rangle$ obtained from time dependence of *A(t)* in Figure 26.2.

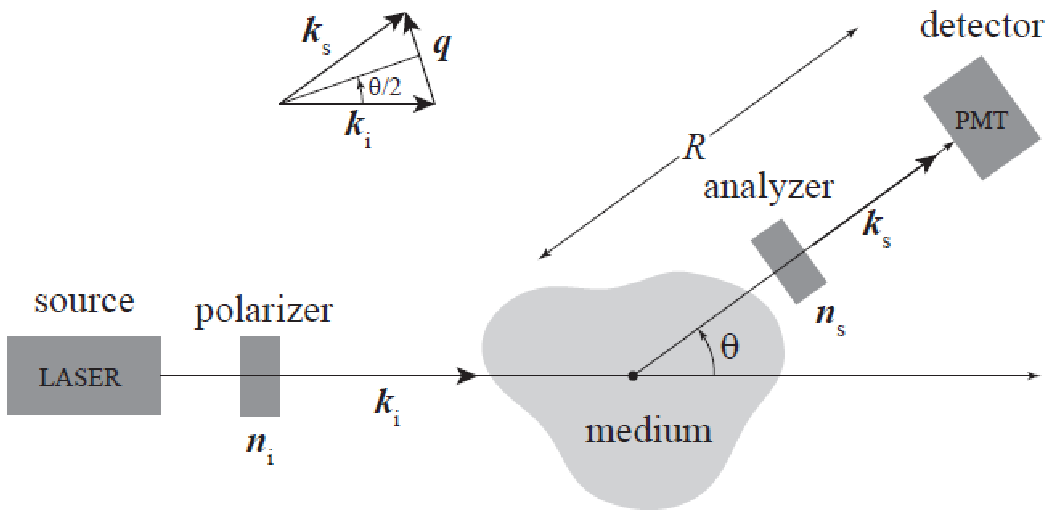

Figure 26.4 Schematic of dynamic light scattering (DLS) setup.

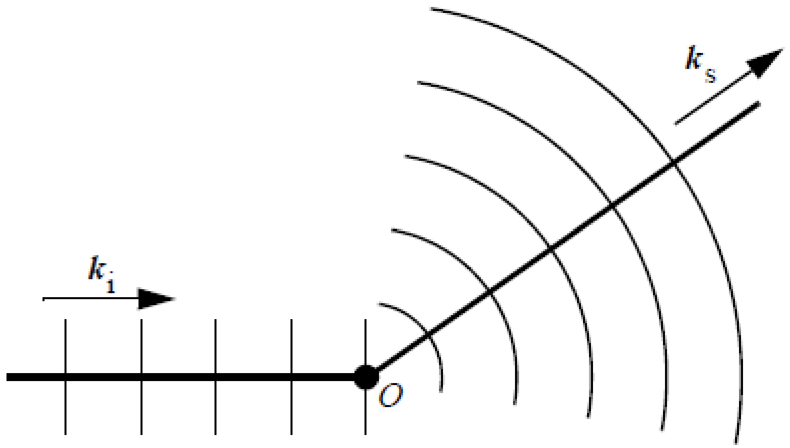

Figure 26.5 Schematic of scattering from a single stationary particle located at the origin.

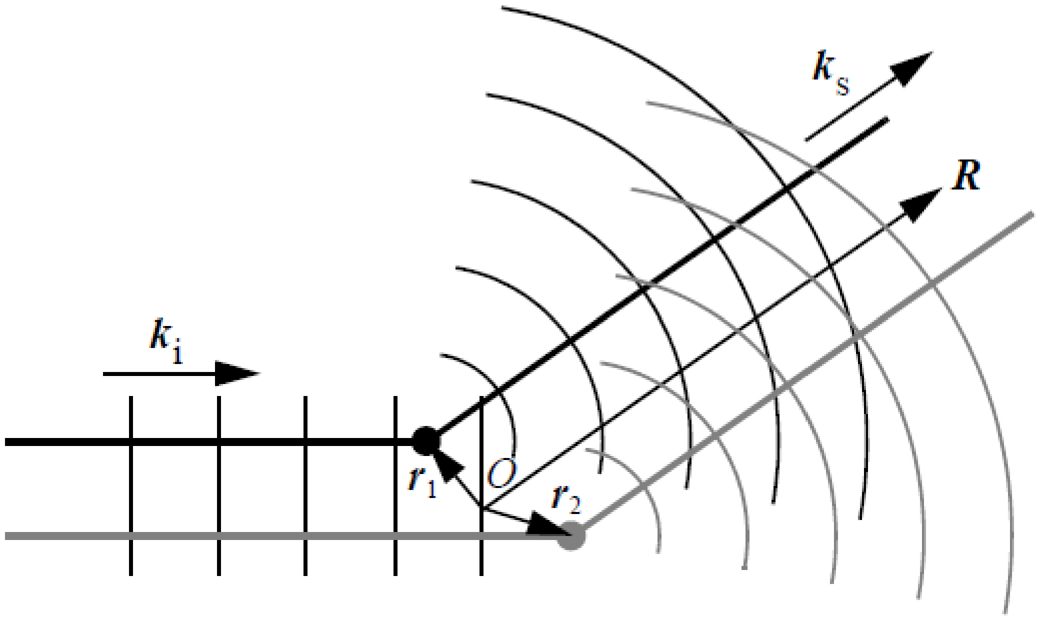

Figure 26.6 Schematic of scattering from two stationary particles located near the origin.

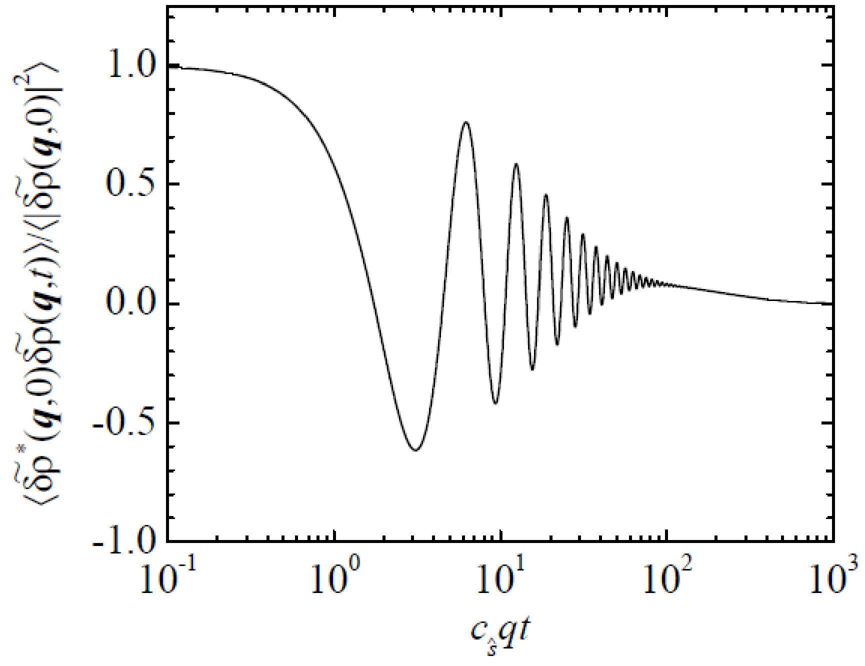

Figure 26.7 Normalized autocorrelation function of density fluctuation $\langle \widetilde{\delta\rho}^*(\boldsymbol{q},0)\widetilde{\delta\rho}(\boldsymbol{q},t)\rangle$ predicted by (26.51) with $\chi q/c_{\hat{s}} = 5 \times 10^{-3}$, $\Gamma q/c_{\hat{s}}$ = 5×10^{-2} and $\gamma = 1.15$

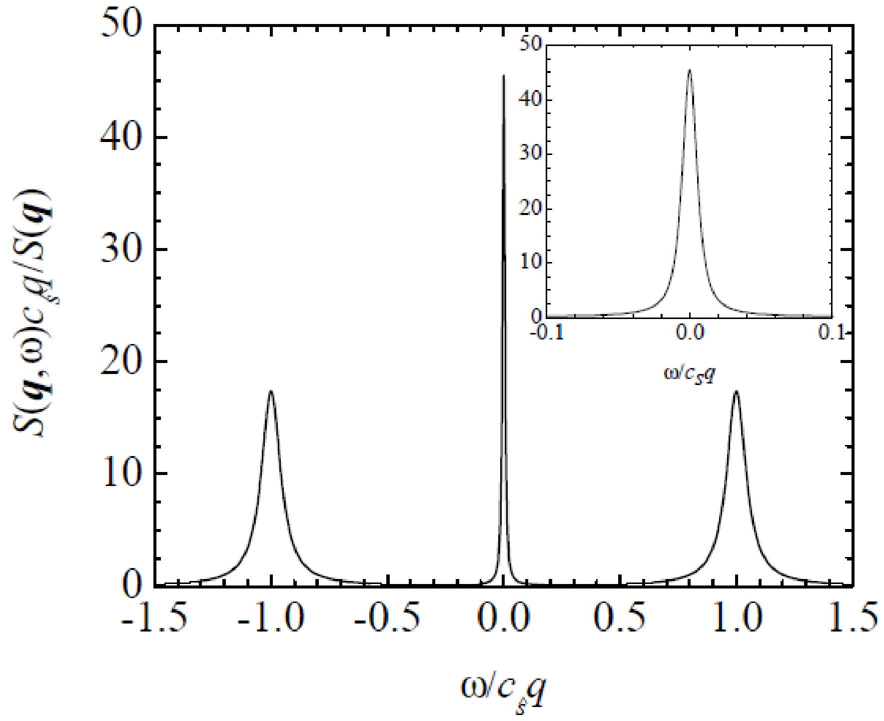

Figure 26.8 Normalized dynamic structure factor $S(\boldsymbol{q},\omega)/S(\boldsymbol{q})$ (scaled by $c_{\hat{s}}q$) predicted by (26.52) with $\chi q/c_{\hat{s}} = 5 \times 10^{-3}$, $\Gamma q/c_{\hat{s}} = 5 \times 10^{-2}$ and γ = 1:15. Inset shows magnfied view of the Rayleigh peak.

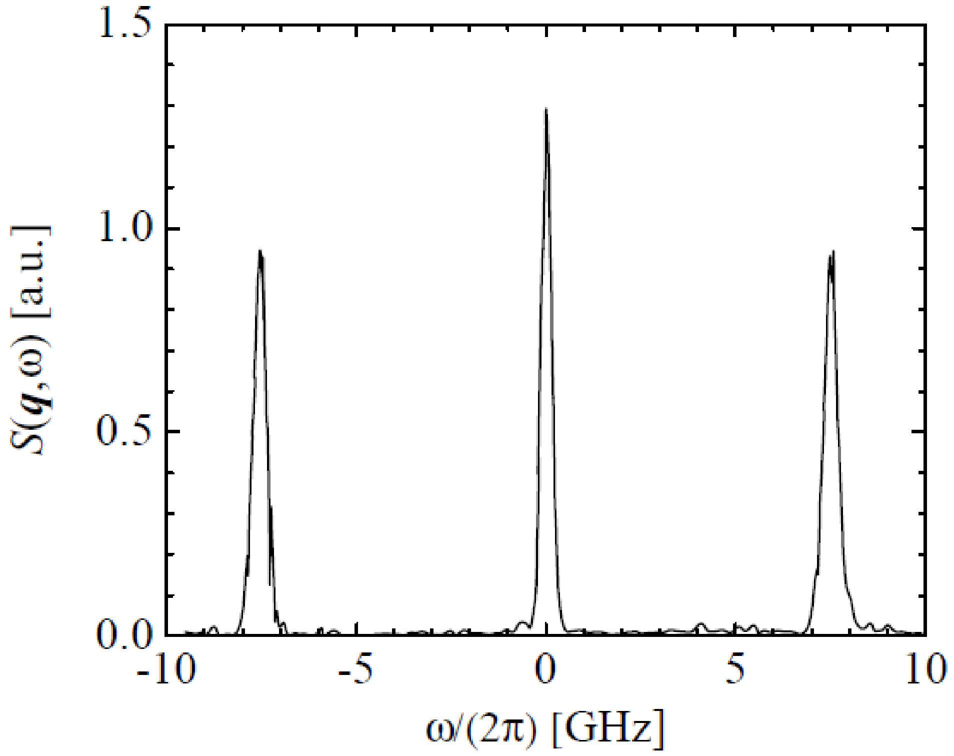

Figure 26.9 Rayleigh-Brillouin spectrum for water at 293 K with $q = 3.0 \times 10^7$ m^{-1}. The Brillouin doublet shift is $\omega_\mathrm{B}/(2\pi) \approx 7.4 \times 10^9$ Hz and the half-width at half maximum $\Delta\omega_\mathrm{B}/(2\pi) \approx 0.31 \times 10^9$ Hz [Adapted from Xu et al., Appl. Optics, 42 (2003) 6704.].